Julius–Maximilians–Universität Würzburg

Thesis for Acquiring the Academic Degree

Doctor Rerum Naturalium

Quantum Chemical Exploration of Potential Energy Surfaces: Reaction Cycles and Luminescence Phenomena

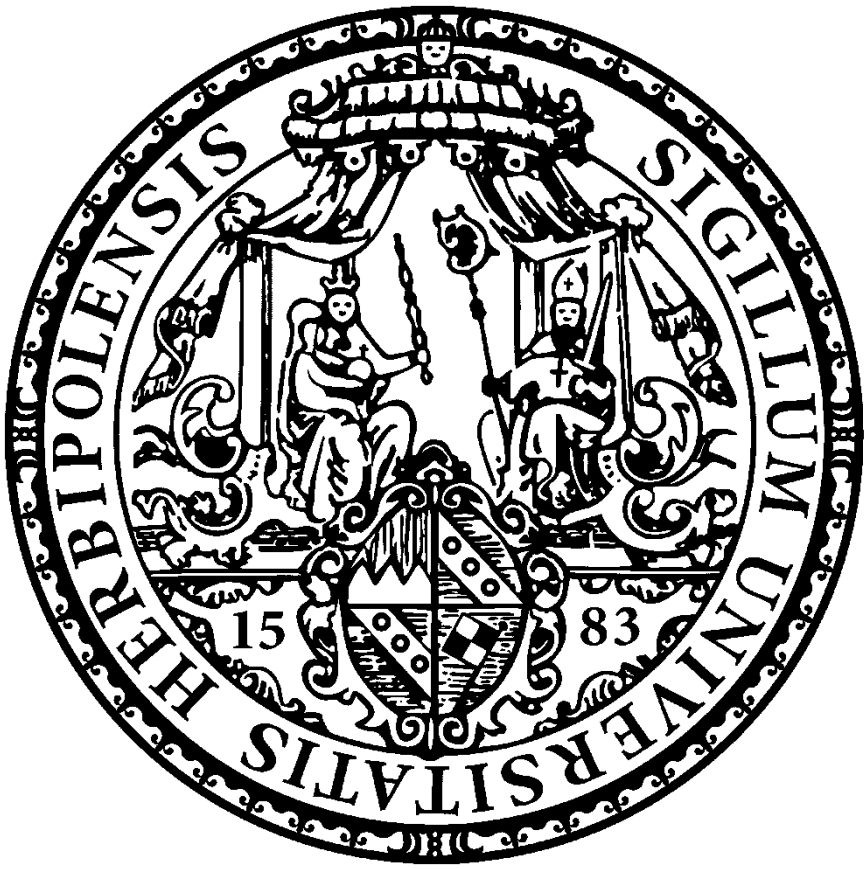

Christoph Herok

Quantum Chemical Exploration of Potential Energy Surfaces: Reaction Cycles and Luminescence Phenomena

Dissertation zur Erlangung des naturwissenschaftlichen Doktorgrades der Julius-Maximilians-Universität Würzburg

vorgelegt von

Christoph Herok

aus Berlin

Würzburg 2024

Eingereicht bei der Fakultät für Chemie und Pharmazie am

30.01.2024

Gutachter der schriftlichen Arbeit

1. Gutachter: Prof. Dr. Bernd Engels

2. Gutachter: Prof. Dr. Volker Engel

Prüfer des öffentlichen Promotionskolloquiums

1. Prüfer: Prof. Dr. Bernd Engels

2. Prüfer: Prof. Dr. Volker Engel

3. Prüfer: Prof. Dr. Tanja Schirmeister

Datum des öffentlichen Promotionskolloquiums

12.03.2024

Doktorurkunde ausgehändigt am

The present work was conducted at the Faculty of Chemistry and Pharmacy of the Julius–Maximilians–University, Würzburg under the supervision of Prof. Dr. Bernd Engels.

This semi–cumulative thesis contains an excerpt of a peer–reviewed scientific publication. Please note that the indexation of the references in this excerpt is not identical to the indexation of the references from the additional chapters in this thesis.

Contents

List of Figures . . . iii
List of Tables . . . iv
List of Abbreviations . . . vi

1 Introduction **1**
1.1 Reactivity of Compounds Containing Cooperating Boron Centers . . 1
1.2 Overview of Boron–Containing Organic Phosphorescent Compounds . 4

2 Theoretical Background **9**
2.1 The CCSD Method and its DLPNO Implementation . . . 9
2.2 Density Functional Theory and IP Tuning . . . 14
2.3 The ONIOM Method . . . 17
2.4 The Nudged Elastic Band Method . . . 19

3 Multifaceted Behavior of a Doubly Reduced Arylborane in B–H–bond Activation and Hydroboration Catalysis **22**

4 Benchmark of First–Shell Solvation Effects **42**
4.1 Introduction . . . 42
4.2 Computational Details . . . 44
4.3 Results and Discussion . . . 46
4.3.1 Comparison of Model and Experiment . . . 46
4.3.2 Influence of System Size and Entropy Corrections . . . 48
4.3.3 Benchmark of Electronic Structure Methods . . . 53
4.3.4 Benchmark of ONIOM Scheme for Optimizations . . . 59
4.4 Conclusions . . . 61

5 Delayed Luminescence Phenomena in Arlyboronic Esters **62**
5.1 Introduction . . . 62
5.2 Computational Details . . . 63
5.3 Results and Discussion . . . 63
5.3.1 Monomer 1 . . . 63
5.3.2 Monomer 2 . . . 64
5.3.3 Comparison of 1 and 2 . . . 65
5.3.4 Dimers of 1 and 2 . . . 68
5.3.5 Investigation of the 2/1 Mixture . . . 71
5.3.6 Compound 3 . . . 77

5.4 Conclusions 83

6 Investigation of RedOx Chemistry and Singlet–Triplet Gaps 84
6.1 Introduction 84
6.2 Computational Details 85
6.3 Results and Discussion 85
6.3.1 Modeling of Reduction and Oxidation Processes 85
6.3.2 Prediction of Singlet–Triplet Gaps 89
6.4 Conclusions 94

7 Summary 95

8 Zusammenfassung 98

9 Appendix 102

10 Acknowledgements 111

11 References 112

12 Author Contributions 121

List of Figures

1 Kinjo's electrostatic hydroboration catalysts. 2
2 Catalytic reactivity of methyl DBA. 3
3 Tetracoordinated boron compounds that show RTP. 4
4 Influence of borylation of the chromophore on RTP properties. 5
5 Phenyl boronic acid derivatives with RTP properties. 6
6 1,4–Phenylenediboronic acid trimer from the corresponding crystal. . 7
7 Geometry distortion in the triplet excited state. 7
4.1 Catalytic Cycles A and B. 42
4.2 Prediction of coordination numbers. 47
4.3 Dependence of the reaction profile on system size. 49
4.4 Dependence of the reaction profile on entropy corrections. 52
4.5 Benchmark of Electronic Structure Methods 55
5.1 Lewis structures of the investigated compounds. 62
5.2 Relaxation of the S0 geometry to the S1 geometry. 66
5.3 Relaxed scans of the Bpin group rotation in 1 and 2. 67
5.4 Relaxed scan of the -NH . . . O(Bpin) distance in 2. 69
5.5 The dimer structures of 1 and 2. 69
5.6 Vertical singlet excitations in the hetero dimer 2/1. 71
5.7 Heterodimer with optimized relative distance. 72
5.8 Vertical singlet excitations in the optimized hetero dimer 2/1. 73
5.9 Vertical singlet excitations in the optimized hetero dimer with tuned functional. 74
5.10 Natural transition orbitals in the hetero dimer 2/1. 76
5.11 Dimer of compound 3. 80
6.1 Reactivity of compound A. 84
6.2 Potential energy surfaces of the di–cation, mono–cation and neutral system. 86
6.3 Isomerisation reaction from $B_1{}^0$ to D^0. 87
6.4 Restricted Kohn–Sham frontier molecular orbitals. 88
6.5 Unrestricted Kohn–Sham frontier molecular orbitals. 89
6.6 Placement of K^+ ions in the singlet ground state of the reduced compound. 91
6.7 Nudge elastic band optimization. 93
9.1 Influence of implicit and explicit solvation on the geometry. 102
9.2 UV–vis spectra of 1. 108

9.3 UV–vis spectra of 2. 108
9.4 UV–vis spectra of the 2/1 system. 109
9.5 UV–vis spectra of 3 in solution. 109
9.6 UV–vis spectra of 3 in the solid state. 110

List of Tables

4.1 Methods and basis sets. 45
4.2 Optimization using the ONIOM scheme. 59
5.1 Vertical and adiabatic excitations in 1. 64
5.2 Vertical and adiabatic excitations in 2. 65
5.3 SOC matrix elements of 1 and 2. 67
5.4 Vertical excitations of homo dimers of 1 and 2. 70
5.5 Monomer calculations of 3 with different basis sets. 77
5.6 Influence of implicit solvation on the vertical excitation of 3. 77
5.7 Influence of implicit solvation on the adiabatic excitation of 3. 78
5.8 Vertical transitions in 3 with the SCS-CC2 method. 78
5.9 Monomer calculations of 3 with DFT and SCS-CC2. 79
5.10 Vertical and adiabatic emission of 3 from the S1 and T1 states. . . . 80
5.11 Dimer calculations on compound 3. 81
5.12 Decomposed dimer calculations on compound 3. 82
6.1 Benchmark of different basis sets with the CPCM(THF)/ωB97X-D4 method. 90
6.2 Adiabatic singlet–triplet gaps of different isomers. 92
6.3 Singlet–triplet gaps of different isomers and ion pair complexes. . . . 93
9.1 Comparison of different optimized coordination spheres and the crystal structure. 103
9.2 Comparison of the influence of system size on electronic energies and entropy corrections to Gibbs Free Energy. 103
9.3 Comparison of Free Energies with different electronic structure methods. 104
9.4 Comparison of Free Energies with different basis sets. 104
9.5 Comparison of Free Energies with the revDSD-PBEP86-D3BJ method. 105
9.6 Comparison of Free Energies with different solvation. 105
9.7 Comparison of Free Energies with the DLPNO-CCSD(T) method. . . 106
9.8 Comparison of Free Energies with the ωB97XD:ωB97XD scheme. . . 106

9.9 Comparison of Free Energies with the DLPNO-CCSD(T):ωB97XD and the DLPNO-CCSD(T):DLPNO-CCSD(T) schemes. 107
9.10 Comparison of wall times and geometrical RMSD for ONIOM scheme optimizations. 107

List of Abbreviations

°C	degrees Celsius
Å	angstrom
AO	atomic orbital
Ar	aryl
AutoAux	automatically generated auxiliary basis
Bpin	pinacol boronic ester group
Bu	butyl
CAAC	cyclic(alkyl)(amino)carbene
CASSCF	complete active space self–consistent field
CC	coupled cluster
CC2	approximate second order coupled cluster
CCSD	second order coupled cluster
CCSD(T)	coupled cluster theory with single, double and perturbative triple excitations
CI	configuration interaction
CISD	second order configuration interaction
CPCM	Conductor–like Polarizable Continuum Model
CT	charge transfer
DBA	9,10–diboraanthracene
DFT	density functional theory
DH	double hybrid
DIP	dipole pair
DLPNO	domain–based local pair natural orbital
EA	electron affinity
ee	electron–electron
EPR	electron paramagnetic resonance
ESI	electronically available supporting information
Et	ethyl
FB	Foster–Boys
GGA	generalized gradient approximation
HBpin	pinacolborane
HF	Hartree–Fock
HO	highest occupied
HOMO	highest occupied molecular orbital
IDPP	image dependent pair potential

IEFPCM	Polarizable Continuum Model with integral equation formalism
IP	ionization potential
ISC	intersystem crossing
K	Kelvin
kcal	kilocalorie
kJ	kilojoule
KS	Kohn–Sham
LC	long–range correction
LMO	localized molecular orbital
LPNO–CCSD	local pair natural orbitals second order coupled cluster
LR	long–range
LSCF	localized self–consistent field
LSDA	local spin density approximation
LUMO	lowest unoccupied molecular orbital
MC–SCF	multiconfigurational self–consistent field
Me	methyl
MEP	minimal energy path
MM	molecular mechanics
MO	molecular orbitals
mol	mole
MP2	second order Møller–Plesset
NEB	nudged elastic band
NHC	N–heterocyclic carbene
NHC^{Me_4}	1,3,4,5–tetra–methyl–imidazol–2–ylidene
NMR	nuclear magnetic resonance
NTO	natural transition orbital
ONIOM	Our Own N-layered Integrated Molecular Orbital and Molecular Mechanics
OSV	orbital specific virtual orbital
OTf	triflate
PAO	projected atomic orbitals
PCM	Polarizable Continuum Model
PES	potential energy surface
Ph	phenyl
PM	Pipek–Mezey
PMMA	polymethyl methacrylate
PNO	pair natural orbital

Pr	propyl
QM	quantum mechanical
RedOx	reduction and oxidation
RI	resolution of identity
RMSD	root mean square deviation
RSH	range–separated hybrid
RTP	room temperature phosphorescence
SC	semi–canonical
SCF	self–consistent field
SCS	spin component scaled
SMD	Solvation Model for Density
SOC	spin orbit coupling
SOMO	singly occupied orbital
SR	short–range
ST	singlet–triplet
TADF	thermally activated delayed fluorescence
TD	time dependent
TDA	Tamm–Dancoff approximation
THF	tetrahydrofuran
TM	transition metal
TS	transition state
XC	exchange–correlation

1 Introduction

This work aims at elucidating chemical processes involving homogeneous catalysis and photo–physical relaxation of excited molecules in the solid state. Furthermore, compounds with supposedly small singlet–triplet gaps and therefore biradicaloid character are investigated with respect to their electro–chemical behavior. The work on hydroboration catalysis via a reduced 9,10–diboraanthracene (DBA) was preformed in collaboration with the Wagner group in Frankfurt, more specifically Sven Prey, who performed all laboratory experiments. The investigation of delayed luminescence properties in arylboronic esters in their solid state was conducted in collaboration with the Marder group in Würzburg. The author of this work took part in the synthesis of the investigated compounds while being supervised by former PhD student Dr. Zhu Wu. The final project was a collaboration with the group of Anukul Jana from Hyderabad, India who provided the experimental data.

To place the investigations within this work in the context of contemporary research, a few illustrative examples of DBA–based homogeneous reactions and boron–containing organic phosphorescent compounds are presented in the following sections.

1.1 Reactivity of Compounds Containing Cooperating Boron Centers

Parts of this work build on the author's master thesis.[1] Hence, the introduction of the master thesis is adapted in this section.

In the past, research showed that by designing molecules which contain two cooperating boron sites, a similar reactivity to transition metal (TM) complexes is achieved.[2] Particularly, the scaffold of 9,10–diboraanthracene (DBA) derivatives exhibits frontier orbitals that are reminiscent of TM d–orbitals.[3] A first observation of the metallomimetic reactivity of these compounds was made by Lorbach *et al.* in 2010.[4] Two boron centers that are part of the central DBA heterocycle were shown to coordinate 1,2–diazine compounds similarly to a TM. A DBA analogue stabilized by N–heterocyclic carbenes was demonstrated to react with O_2, CO_2, and ethylene via formal [4+2] cycloaddition to the central diborabutadiene moiety.[5] Thus, these small molecules were untypically activated by compounds consisting only of main

group elements.[6]

Especially Prof. Rei Kinjo's research group at the Nanyang Technological University, Singapore focuses on this class of DBA related compounds.[7–11]

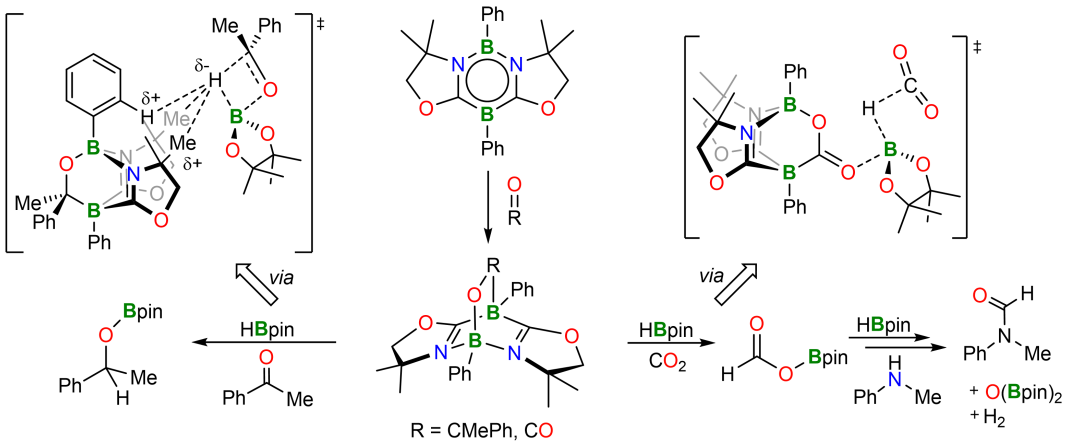

Figure 1: Kinjo's hydroboration catalysts based on electrostatic interactions of the substrate–precatalyst cycloadducts. Adapted from [1].

Figure 1 depicts a 1,3,2,5–diazadiborinine that was reported by Kinjo and coworkers in 2015.[8] In order to become iso–electronic to the related anthracene molecule and exploit the symmetry of the frontier orbitals for TM–like reactivity, the scaffold is not reduced by an reducing agent, but N atoms are introduced. Furthermore, the outer aromatic rings are replaced by saturated five–membered heterocycles containing O atoms.

Wu *et al.* reported on the catalytic activity of a hydroboration with HBpin.[12] The catalytically active species was found to be the cycloadduct with the corresponding substrate and not the diazadiborinine itself. It is speculated that the two oxazoline units and one phenyl substituent at boron form a partially positively charged hydride pocket (Figure 1, left transition state, TS). The hydridic hydrogen atom of HBpin is stabilized without forming or dissociating any covalent bonds and the hydroboration reaction is facilitated purely through electrostatic interaction. A relatively high activation barrier of 27 kcal mol^{-1} was calculated for the depicted transition state, despite the mild reaction conditions, i.e. room temperature. If CO_2 gas is added to the diazadiborinine, the resulting cycloadduct is suggested to exhibit catalytic activity as well, albeit coordination takes place at the double–bonded oxygen instead of the oxazoline pocket (Figure 1, right TS). It was confirmed by quantum chemical calculations that the transition state in Figure 1 is accurate and

the oxazoline pocket is not involved, because the reaction barriers were calculated to be 19 kcal mol^{-1} and 40 kcal mol^{-1}, respectively. If the reduced CO_2 compound is treated with *N*–methyl–aniline and excess HBpin, the N–formylation product is formed.[1]

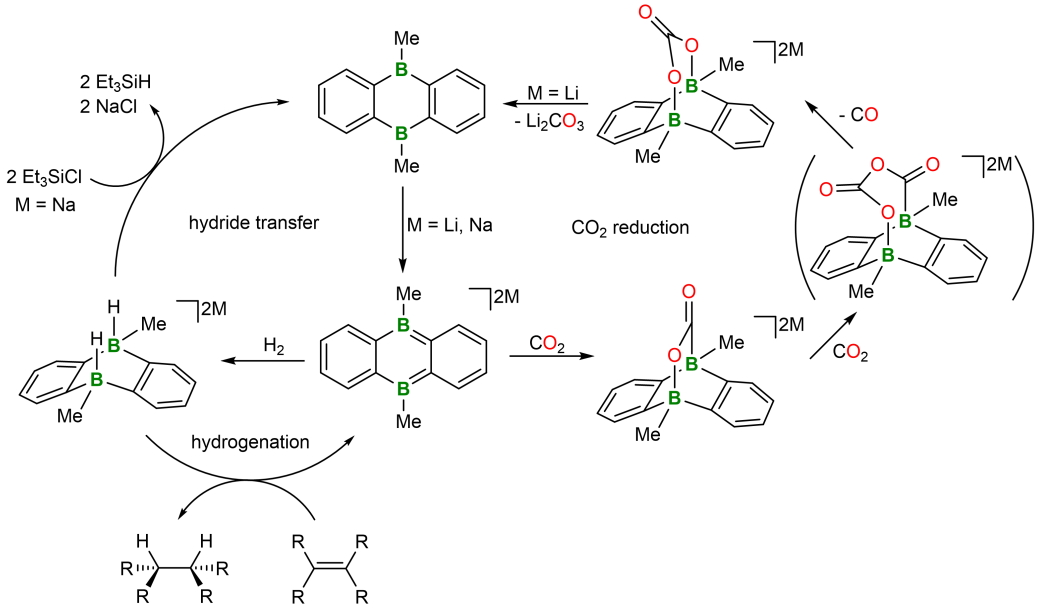

Figure 2: Reactivity of methyl DBA catalyst reported by Wagner and coworkers. Adapted from [1].

Wagner and coworkers at the University Frankfurt approached DBA chemistry via a different route than the Kinjo group. Instead of introducing nitrogen atoms into the heterocycles, they reduced a neutral DBA with alkali metals. The resulting DBA salts were shown to reversibly activate dihydrogen and to perform 1,4–addition reactions.[4, 13] Figure 2 shows a selection of possible reactions of methyl substituted DBA salts.

If the reduced DBA is reacted with CO_2, CO_2 adds across the central heterocycle to form a doubly negatively charged adduct.[14] This adduct, which exhibits an activated C=O double bond, was reported to react with excess CO_2 via C=O bond insertion. The resulting OCOC bridge at the DBA scaffold is labile with respect to CO elimination. After CO gas is eliminated from the complex, the remaining C_1 unit appears to be a carbonate di–anion $[CO_3]^{2-}$. If the DBA was reduced by Li metal in the first step of the reaction sequence, Li carbonate precipitates from solution and the parent neutral DBA can be isolated for reuse. This is not possible for the Na salt, which is rationalized by Wagner and coworkers by a smaller driving

force in the case of Na_2CO_3.

Von Grotthuss *et al.* reported another two distinct reactivities of the same reduced DBA in 2019.[15] Instead of CO_2 the DBA was reacted with dihydrogen gas H_2 and analogously, the H–H bond was activated by the cooperating boron centers. This di–anionic dihydrogen complex was shown to be capable of hydrogenation and hydride transfer reactions (see Figure 2).

1.2 Overview of Boron–Containing Organic Phosphorescent Compounds

Room temperature phosphorescence (RTP) in purely organic compounds is a relatively rare phenomenon, yet its research field has been attracting more and more attention over the recent years.[16] Highly efficient metal–free triplet phosphors are desirable luminescent materials because of their low toxicity and cost in comparison to transition metal or heavy atom containing compounds. Furthermore, there is a range of potential applications utilizing RTP materials, e.g. oxygen detection[17, 18] or tumor hypoxia imaging[19]. An early example of a tetracoordinated boron compound that exhibits RTP in the solid state is the boron β–diketonate reported by Zhang *et al.* in 2007.[17] Said compound was used as initiator for ring opening polymerization of lactide, producing the end–functionalized polyactide **A** (see Figure 3). Similarly, the related β–hydroxy–vinylimine boron compound **B** (see Figure 3) reported by Koch *et al.*[20] shows efficient phosphorescent emission both in solution and when doped in PMMA.

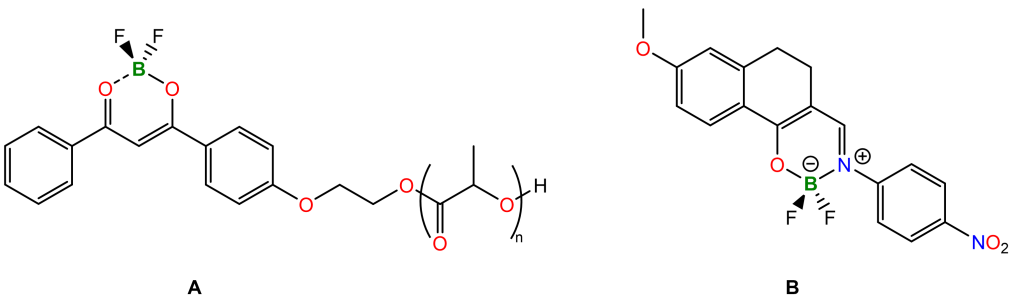

Figure 3: Tetracoordinated boron compounds that show RTP.

The cause of phosphorescence in both compounds **A** and **B** has been ascribed to singlet fission. Singlet fission is a process that involves the fast energy transfer from a singlet–excited molecule to an adjacent ground state molecule, producing a pair

of correlated triplet–excited molecules. This phenomenon enables quantum yields of up to 200%.[21] Indeed, compound **B** was found to emit with a quantum yield of 118% in PMMA. The most important properties that monomers need to feature for singlet fission to be possible are the absence of fast non–radiative deactivation processes and a favorable alignment of energy levels. The former condition is met by doping PMMA with the compound or investigating it in the neat solid state. The latter condition is met when

$$E(S_1), E(T_2) \geq 2E(T_1), \tag{1}$$

or in other words, there needs to be a very low lying first triplet state.[22]

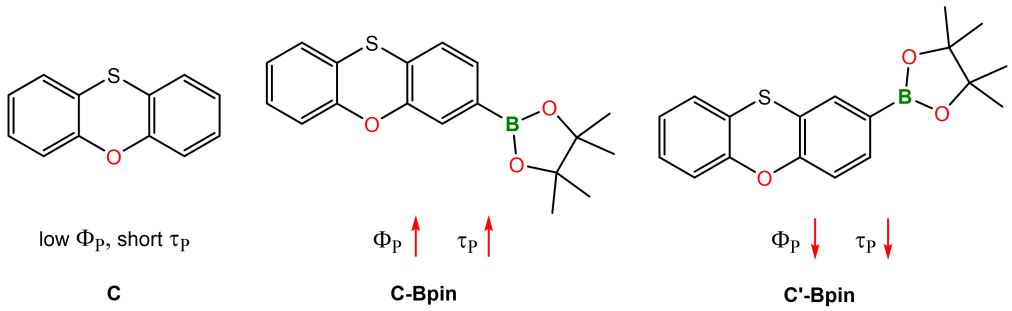

Figure 4: Influence of borylation of the chromophore on RTP properties.

Energetically low excited states can be achieved by means of strong π–π stacking interactions in the solid state.[20] This was demonstrated by Su and coworkers in 2019.[23] Phenoxathiine **C** (see Figure 4) was borylated in positions 3 (**C-Bpin**) and 2 (**C′-Bpin**) and the effect on the phosphorescent emission was studied. The authors found improved RTP in **C-Bpin** and worse quantum yields and a shorter lifetime in **C′-Bpin**. This observation was rationalized by the intermolecular packing mode which becomes tighter in the following order: **C′-Bpin**, **C**, **C-Bpin**. Quantum mechanical calculations showed the stabilization of triplet excited states in the tetramer with respect to the monomer. This effect becomes more pronounced for tightly packed molecular environments. Furthermore, non–radiative relaxation is inhibited which is beneficial to the preservation of long–lived excitons. Both arguments explain why **C-Bpin** exhibits improved RTP in comparison to **C**.

In 2017, Chai *et al.* investigated a series of phenyl boronic acid derivatives and their corresponding dehydrated boroxine trimers (see Figure 5).[24] In the same vein

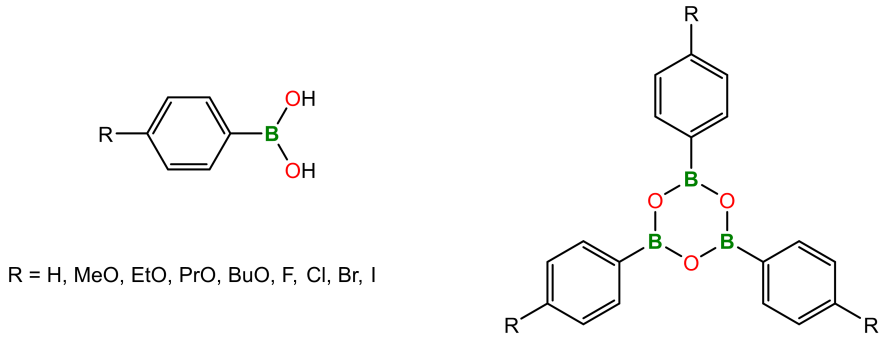

Figure 5: Phenyl boronic acid derivatives with RTP properties.

as the previous example, the authors argue that a rigid conformation in the solid state and effective π–π stacking lead to bright and persistent RTP for small molecular systems. They suggest an approach to building a "Boron–containing Phosphors Toolbox"[24] based on strong intermolecular interactions in the form of hydrogen bonds.

So far, all discussed compounds contained free electron lone pairs which facilitate spin orbit coupling (SOC) through El–Sayed's rule[25]. Sufficient SOC accelerates intersystem crossing (ISC) which enables the phosphorescence process to compete with other relaxation pathways like fluorescence or non–radiative decay. Wu *et al.* reported an unprecedented example of RTP in a triaryl boron compound devoid of any lone pair bearing heteroatoms.[26] Detailed study and comparison of the crystal framework of the phosphorescent BAr_3 with similar non–phosphorescent compounds revealed that strong intermolecular interactions are more favorable in terms of RTP than a dense packing mode alone. Quantum chemical calculations showed that the ISC process is accelerated by transitions between local σ and π excitation which exhibit considerable SOC. The SOC that was found leads to an ISC rate of the same order of magnitude as the calculated fluorescence rate, rendering phosphorescence a competible relaxation process.

A different mechanism for ISC was proposed by Kuno *et al.* in 2017.[27] According to Kuno, the generation of the triplet state in crystalline 1,4–phenylenediboronic acid is a result of hyperfine coupling in radical ion pairs. The excited monomer redistributes its energy via a charge transfer (CT) process onto an adjacent monomer in the solid state. The CT complex then transitions from a singlet excited state to a triplet excited state, leading to phosphorescence emission. The hyperfine coupling is dependent on the magnetic properties of the environment and can be manipu-

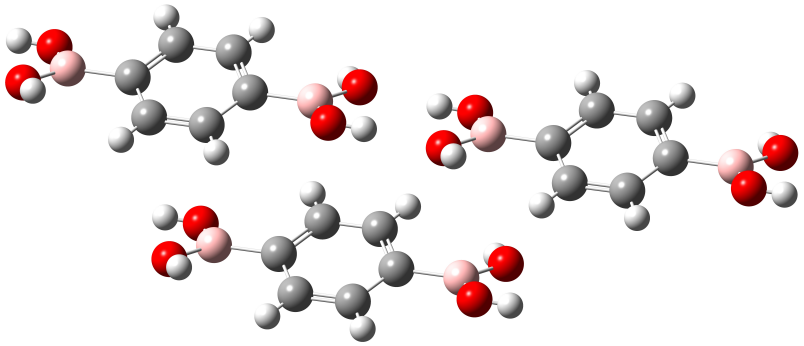

Figure 6: 1,4–Phenylenediboronic acid trimer from the corresponding crystal.

lated by an outer magnetic field as well as spin–isotope effects, i.e. when hydrogen atoms in the compound are replaced by deuterium. Both factors have been shown to influence the RTP intensity of 1,4–phenylenediboronic acid. TD–DFT calculations revealed no CT transition for the head–to–tail dimer, but if a third molecule is considered (see Figure 6), an obvious CT transition between the H–bond bridged monomers appears. Moreover, the crystalline 1,4–boronic esters of 1,2–propanediol, 2,3–butanediol and pinacol (pin) were studied. The authors report diminishing RTP for the bulkier head groups. The bis–Bpin substituted aryl compound doesn't show any RTP, which is explained by the CT inhibiting size of the head group due to large intermolecular distances.

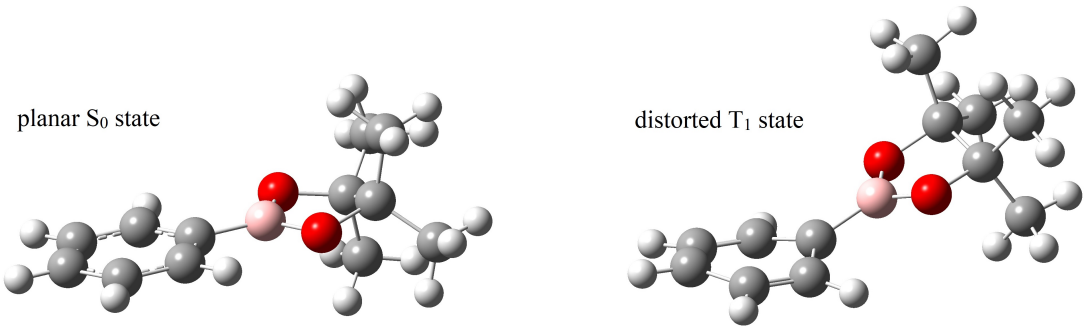

Figure 7: Geometry distortion in the triplet excited state.

In the same year, Fukushima and coworkers published a now well–cited paper on long–lived RTP in simple arylboronic esters.[28] A variety of Bpin–substituted aryl compounds was studied and 14 of the 19 investigated compounds were reported to emit persistent RTP in the solid state. Inspection of single–crystal X–ray data revealed no special features indicating RTP facilitation. To back up the measured RTP emission data, quantum chemical calculations were performed. The authors report a close match between the calculated $T_1 \rightarrow S_0$ transition and the peak in the

emission spectrum of mono–Bpin–substituted benzene (calc. 475 nm, exp. 465 nm). Furthermore, optimization of the lowest triplet excited state showed an out–of–plane distortion of the Bpin group (see Figure 7), for which non–zero SOC for the $T_1 \rightarrow S_0$ transition was calculated using a CASSCF(6,6) method. Fast ISC is attributed to the geometry distortion which enables the mixing of π and σ orbitals and subsequent SOC.

A review on the discussed ISC mechanisms was published by Kuno and Yuasa in 2018.[29]

2 Theoretical Background

Traditionally, there are two distinct approaches to solving the electronic Schrödinger equation that are applied in quantum chemistry. Wavefunction–based theory aims at constructing and manipulating the electronic wavefunction of a system, which contains all information about the system, such as position and spin of its electrons. Prominent examples thereof are the Hartree–Fock (HF), Configuration Interaction (CI), Coupled Cluster (CC), and Multiconfigurational Self–Consistent Field (MCSCF) methods. While the latter (post–HF) approaches offer a rigorous description of electron correlation and can provide accurate results for strongly correlated systems, they become computationally too demanding for molecular applications that involve large systems, as the computational effort scales superlinearly. For instance, CCSD and CCSDT calculations are commonly known to be of $O(N^6)$ and $O(N^8)$ complexity, respectively. Hereby, N is a measure of system size. In contrast, density–based methods, i.e. Density Functional Theory (DFT), take a different approach. Instead of directly manipulating the wavefunction, DFT focuses on the electron density, a function describing the probability distribution of electrons in the system. DFT has gained widespread popularity due to its computational efficiency, allowing for the study of larger molecular systems. However, the inherent approximations in the exchange–correlation functionals can lead to challenges in accurately capturing correlation effects, especially for systems with strong electron correlation or open–shell character.

In the following sections, the DLPNO–CCSD (domain–based local pair natural orbital) method will be discussed exemplarily as a wavefunction–based method and approximations therein are described that make the high–level CC method feasible even for large systems. Subsequently, an overview over DFT and more specifically Ionization Potential (IP) tuning is presented. When the systems of interest become too large for pure electronic structure methods, hybrid or multi–scale methods can be employed. Another section of this chapter briefly introduces the ONIOM method to elucidate the basic concepts of these approaches. Finally, the Nudged Elastic Band (NEB) method is discussed as a tool to explore the potential energy surface.

2.1 The CCSD Method and its DLPNO Implementation

A popular *ab initio* method to describe electron correlation is the Coupled Cluster (CC) approach. The basic ideas are presented here in accordance to Jensen[30] and Cramer[31].

In CC theory, the Schrödinger equation is formulated as follows:

$$\hat{H}e^{\hat{T}}\Psi_{HF} = Ee^{\hat{T}}\Psi_{HF} \tag{2}$$

Ψ_{HF} is the HF wavefunction and $\hat{T}$ is the cluster operator with terms up to the n–th order, whereby n is the number of electrons that are present in the investigated system:

$$\hat{T} = \hat{T}_1 + \hat{T}_2 + \ldots + \hat{T}_n \tag{3}$$

$$\hat{T}_1 = \sum_{i}^{occ}\sum_{a}^{vir} t_i^a \psi_i^a \tag{4}$$

$$\hat{T}_2 = \sum_{i<j}^{occ}\sum_{a<b}^{vir} t_{ij}^{ab} \psi_{ij}^{ab} \tag{5}$$

When the exponential operator from (2) is truncated at second order (which resembles the CCSD (singles and doubles) approximation) and expanded in a Taylor series, one obtains:

$$e^{\hat{T}_1+\hat{T}_2} = 1 + \hat{T}_1 + (\hat{T}_2 + \frac{1}{2}\hat{T}_1{}^2) + (\hat{T}_2\hat{T}_1 + \frac{1}{6}\hat{T}_1{}^3) + (\frac{1}{2}\hat{T}_2{}^2 + \frac{1}{2}\hat{T}_2\hat{T}_1{}^2 + \frac{1}{24}\hat{T}_1{}^4) + \ldots \tag{6}$$

The cluster amplitudes t are then determined by multiplying (2) from the left by trial wavefunctions which are expressed as determinants of the HF orbitals. The resulting expressions form coupled non–linear equations that are solved by iterative techniques. In comparison to the Configuration Interaction of second order (CISD) CCSD includes more correlation energy, because the exponential formulation of the cluster operator leads to the inclusion of higher order excitations. The fourth term on the right side of (6) describes so called "disconnected" triple excitations as opposed to the "connected" excitations that are obtained by the $\hat{T}_3$ excitation operator. Identically, the fifth term describes disconnected quadruple excitations which enter the amplitude equations weighted by products of single and/or double amplitudes. The inclusion of the excitations of higher order than the truncation of the cluster operator makes the CC method size consistent. In contrast, truncated CI methods do not include higher order excitations and therefore lack size consistency. A downside of CC theory is that the approach is non–variational which means that it is possible to obtain more than 100% of the full CI correlation energy.

As previously mentioned, the CCSD method is far from linear scaling ($O(N^6)$). The reason for the high computational effort is that the standard implementation of CC theory builds on canonical HF orbitals which are delocalized over the entire molecule. In principle, all orbitals contribute to the electronic wavefunction even if

only a specific part of the molecule is considered. As a consequence, the CC approach is generally not feasible in molecular applications except for rather small systems. As the physical force that leads to electron correlation is only at play between pairs of particles, the scaling of the CC method might be regarded as "non-physical" [30]. To make the calculations more efficient, so called localized molecular orbital (LMO) methods began to emerge.[32, 33] The use of a set of localized orbitals promises a more compact wavefunction and therefore less computational effort. However, as the Fock matrix is only diagonalized by canonical molecular orbitals, implementation of a LMO based method is not straight–forward. As an example, the basic ideas of the DLPNO–CCSD method according to Neese and coworkers[34] are summarized below.

Initially, an efficient local coupled cluster method with single and double excitations based on pair natural orbitals (LPNO–CCSD)[35] was devised by Neese *et al.* in 2009. The newer DLPNO–CCSD method improves on the previous method by introducing electron pair correlation domains. The domains are constructed by first localizing the canonical occupied orbital space which the authors also call the internal orbital space. There are several possibilities to obtain LMOs.[30] The general procedure involves unitary transformations of canonical MOs (7). The unitary transformation preserves the orthogonality of the canonical MOs.

$$\begin{aligned} \phi' &= U\phi \\ \phi'_i &= \sum_{j=1}^{N_{orb}} u_{ij}\phi_j \end{aligned} \tag{7}$$

One possibility to define a set of LMOs is to optimize the expectation value of a two–electron operator Ω which depends on the u parameters from (7):

$$\langle\Omega\rangle = \sum_{i=1}^{N_{orb}} \langle\phi'_i\phi'_i|\Omega|\phi'_i\phi'_i\rangle \tag{8}$$

The Foster–Boys (FB) localization scheme[36] aims at minimizing the expectation value of the squared distance of an electron pair:

$$\langle\Omega\rangle_{FB} = \sum_{i=1}^{N_{orb}} \langle\phi'_i\phi'_i|(\mathbf{r}_1 - \mathbf{r}_2)^2|\phi'_i\phi'_i\rangle \tag{9}$$

The resulting FB-type LMOs minimize the spatial extent of the orbitals which yields a very compact description of the system. Another possibility is the Pipek-Mezey

(PM) localization scheme[37] in which the sum of the Mulliken atomic charges is maximized:

$$\begin{aligned} \rho_A &= \sum_{i=1}^{N_{orb}} \sum_{\alpha \in A}^{M_{basis}} \sum_{\beta}^{M_{basis}} c_{\alpha i} c_{\beta i} S_{\alpha\beta} \\ \langle \Omega \rangle_{PM} &= \sum_{A=1}^{N_{atoms}} |\rho_A|^2 \end{aligned} \tag{10}$$

$S_{\alpha\beta}$ is the overlap matrix of the atomic orbitals (AO) α and β, whereby the index α runs over all AOs that belong to atom A. The coefficients c are obtained from the density matrix of the system. While most localization schemes yield similar LMOs, an important difference arises between FB and PM-type LMOs. While PM LMOs preserve σ/π separation, FB LMOs mix both bond types and produce bent "banana" bonds.[30]

For the DLPNO–CCSD method, both of the two described localization approaches can be used, but Neese and coworkers chose the FB localization criterion for localizing the internal orbital space. The resulting internal LMOs $|i\rangle$ are each assigned a separate correlation domain $\{A\}_i$ which consists of all atoms A that contribute to $|i\rangle$ with a significant amplitude, i.e. an amplitude above a certain threshold. For each electron pair ij the pair domain $\{A\}_{ij}$ then spans the union of the individual correlation domains. In the next step, electron pairs are prescreened by the calculation of electron pair correlation energies ε_{ij}. To keep the prescreening efficient, a series of approximations is made, one of which is the resolution of identity approximation, i.e. density fitting.[38–43] Starting from the canonical second order Møller–Plesset (MP2)[44] pair energy

$$\varepsilon_{ij}^{MP2} = -\sum_{ab} \frac{4(ia|jb)(ia|jb) - 2(ia|jb)(ib|ja)}{\varepsilon_a + \varepsilon_b - \varepsilon_i - \varepsilon_j} \tag{11}$$

which features the eigenvalues of the diagonalized Fock matrix, i.e. the orbital energies ε, the so called semi-canonical MP2 (SC–MP2) approximation is applied. For semi–canonical MP2 the virtual part of the Fock matrix is diagonal, but the occupied part is not. Hence the corresponding orbital energies are replaced by the diagonal elements F_{ii} while off–diagonal elements F_{ij} are ignored:

$$\varepsilon_{ij}^{SC-MP2} = -\sum_{ab} \frac{4(ia|jb)(ia|jb) - 2(ia|jb)(ib|ja)}{\varepsilon_a + \varepsilon_b - F_{ii} - F_{jj}} \tag{12}$$

The second exchange–type matrix element is omitted as the exchange integral is assumed to fall quickly to zero for large electron–electron distances. The remaining

Coulomb–type term is approximated by expressing the canonical virtual orbitals (a) in a specific set of virtual orbitals $\{\tilde{a}\}$ which contains special correlating orbitals $\{\tilde{a}_i\}$ for each occupied orbital $|i\rangle$. These orbital specific virtual orbitals (OSV)[45] are then truncated to further reduce calculation cost and the resulting expression for the approximated pair energy is:

$$\varepsilon_{ij}^{SC-OSV} \approx -4 \sum_{\tilde{a}_i \tilde{b}_j} \frac{\left(i\tilde{a}_i | j\tilde{b}_j\right)^2}{\varepsilon_{\tilde{a}_i} + \varepsilon_{\tilde{b}_j} - F_{ii} - F_{jj}} \tag{13}$$

The OSVs are not expanded in virtual orbitals as in the original literature, but in terms of local projected atomic orbitals (PAO):

$$\begin{aligned} |\tilde{a}_i\rangle &= \sum_{\tilde{\mu}' \in \{i\}} d^i_{\tilde{\mu}' a} \, |\tilde{\mu}'\rangle \\ |\tilde{\mu}'\rangle &= \left(1 - \sum_i |i\rangle\langle i|\right) |\mu\rangle \end{aligned} \tag{14}$$

The AO $|\mu\rangle$ is projected onto the localized occupied space ($\sum_i |i\rangle\langle i|$) to obtain PAOs $|\tilde{\mu}'\rangle$ that span the corresponding virtual space. Finally, a multipole expansion is performed to yield the so–called OSV–dipole pair energy (OSV–DIP):

$$\varepsilon_{ij}^{OSV-DIP} = -\frac{8}{R_{ij}^3} \sum_{ab} \frac{\left(\langle i|\mathbf{r}|\tilde{a}_i\rangle \left\langle j|\mathbf{r}|\tilde{b}_j\right\rangle\right)^2}{\left(\varepsilon_{\tilde{a}_i} + \varepsilon_{\tilde{b}_j} - F_{ii} - F_{jj}\right)} \tag{15}$$

$\varepsilon_{ij}^{OSV-DIP}$ is computed for all electron pairs. It is the main criterion by which the algorithm decides which electron pairs are kept for the actual CCSD calculation. When $\varepsilon_{ij}^{OSV-DIP}$ is above a conservatively chosen threshold, the corresponding pair natural orbitals[46, 47] are generated and used for the subsequent CC iterations.

In summary, the further development of the LPNO–CCSD approach towards the DLPNO–CCSD by Neese and coworkers yields a near linear scaling method with respect to system size. By efficient, domain–based prescreening of electron pair terms before the CC iterations computational cost is reduced considerably. The CCSD calculations on the remaining electron pairs exploit the locality and compactness of the PNO ansatz. Truncation thresholds for the inherent approximations have been chosen conservatively, which means they do not need adjustment by the user and give rise to the black box character of the method.

2.2 Density Functional Theory and IP Tuning

The principles of DFT are summarized according to Jensen[30] and Cramer[31] in the following section.

According to the Hohenberg–Kohn existence theorem, there is a functional of the non–degenerate ground state electron density that is biuniquely linked to the external potential, i.e. the charges and positions of the nuclei, of a given system. In other words, the electron density determines the exact Hamiltonian and therefore also the exact wavefunction which contains all information about the system. The second Hohenberg–Kohn theorem, the variational theorem, proves that for the exact density functional the variational principle from MO theory still holds. Consider an arbitrary electron density that determines a candidate wavefunction. The energy expectation value for this candidate wavefunction is always greater than or equal to the expectation of the ground state wavefunction which in turn is determined by the ground state density. It is important to note that approximations to the exact density functional eliminate this relation and it is therefore possible to obtain energies that lie below the exact energy.

However, determining the energy expectation value by the wavefunction route does not yield any simplification in comparison to a wavefunction–based ansatz, as the many–body Schrödinger equation needs to be solved regardless. In a fundamental breakthrough, Kohn and Sham[48] developed a methodology in which the simplified Hamilton operator contains a sum over one electron operators for non–interacting electrons. In such a fictitious system without electron–electron (ee) interaction, the overall ground state density must be identical to a real system which includes interaction, as the external potential is the same. The energy functional of the resulting Kohn–Sham ansatz can be partitioned in the following way:

$$E\left[\rho(\mathbf{r})\right] = T_{ni}\left[\rho(\mathbf{r})\right] + V_{ne}\left[\rho(\mathbf{r})\right] + V_{ee}\left[\rho(\mathbf{r})\right] + \Delta T\left[\rho(\mathbf{r})\right] + \Delta V_{ee}\left[\rho(\mathbf{r})\right] \tag{16}$$

T_{ni} gives the kinetic energy of the non–interaction electrons, V_{ne} is the nuclear–electron interaction and V_{ee} is the classical ee repulsion. The terms denoted with Δ correspond to correction terms which must be included to account for ee interaction. ΔT corrects for the influence of ee interactions on the kinetic energy and ΔV_{ee} includes all non–classical corrections to the ee repulsion energy. When the density

in (16) is expressed in orbitals one obtains the following equation:

$$\begin{aligned} E[\rho(\mathbf{r})] = &\sum_{i}^{N} \left(\left\langle \chi_i \left| -\frac{1}{2}\nabla_i^2 \right| \chi_i \right\rangle - \left\langle \chi_i \left| \sum_{k}^{\text{nuclei}} \frac{Z_k}{|\mathbf{r}_i - \mathbf{r}_k|} \right| \chi_i \right\rangle \right) \\ &+ \sum_{i}^{N} \left\langle \chi_i \left| \frac{1}{2} \int \frac{\rho(\mathbf{r}')}{|\mathbf{r}_i - \mathbf{r}'|} d\mathbf{r}' \right| \chi_i \right\rangle + E_{\text{xc}}[\rho(\mathbf{r})] \end{aligned} \tag{17}$$

The term $E_{\text{xc}}[\rho(\mathbf{r})]$ represents the sum of the correction terms in (16) and is called the exchange–correlation functional. In contrast to canonical MO theory, it also includes the correction to the kinetic energy which does not appear in wavefunction–based exchange and correlation terms. The Kohn–Sham one–electron operator is then defined as

$$\begin{aligned} h_i^{\text{KS}} = -\frac{1}{2}\nabla_i^2 - \sum_{k}^{\text{nuclei}} \frac{Z_k}{|\mathbf{r}_i - \mathbf{r}_k|} + \int \frac{\rho(\mathbf{r}')}{|\mathbf{r}_i - \mathbf{r}'|} d\mathbf{r}' + V_{\text{xc}} \\ V_{\text{xc}} = \frac{\delta E_{\text{xc}}}{\delta \rho} \end{aligned} \tag{18}$$

When the Kohn–Sham orbitals are expanded in a set of basis functions, the orbital coefficients can be determined analogously to HF theory.

There is an important difference of wavefunction–based approaches and DFT with an approximate exchange–correlation functional. While wavefunction–based methods deliberately choose approximate equations for the many–body problem and yield the exact solutions to those equations, DFT equations are exact but their solutions must be approximated since the exact exchange–correlation operator is unknown.[31] As a consequence, a hierarchy of distinct approximations have been developed which often are classified along Perdews "Jacob's ladder" classification[49]:

The first tier of DFT theory is the local spin density approximation (LSDA). Within the LSDA ansatz, the density functional is evaluated in analogy to the Thomas–Fermi–Dirac model[50], i.e. the assumption of a uniform electron gas. Hereby, the electron density at a specific point in space, hence the addition of local to the acronym, is assumed to behave like a uniform electron gas with the same density. For significant changes in the density throughout space, which is obviously the case for molecular systems, the LSDA introduces a large error. Therefore, the gradient of the density is included in the density functional to include local density changes. This yields the so called generalized gradient approximation (GGA). GGA functionals constitute the DFT tier above the LSDA methods. As a further improvement, the second derivative, i.e. the Laplacian, of the density can be included into the functional. This higher order gradient correction is called *meta*–GGA and

represents the third tier on Jacob's ladder. It can be shown that the orbital kinetic energy density τ carries the same information as the Laplacian of the density. As the calculation of τ is more numerically stable, τ is also commonly used in *meta*–GGA functionals. All the above DFT approximations suffer from self–interaction error. In contrast to HF theory, the ee interaction for, e.g., a single electron system generally does not cancel out for DFT functionals as there are no equivalent Coulomb and exchange integrals. To remedy the self–interaction error, the DFT exchange is admixed with a fixed portion of exact nonlocal HF exchange, resulting in the fourth DFT tier, the *hyper*–GGA or hybrid GGA functionals. While the use of hybrid GGA methods somewhat improves on the self–interaction error, the exchange potential shows a wrong asymptotic behavior for large ee distances. Therefore, a long–range correction (LC, *vide infra*) is introduced in the so–called LC–GGA functionals. To capture dynamical correlation and long–range interaction effects, e.g. van der Waals interactions, unoccupied Kohn–Sham orbitals are included at the fifth and last tier of Jacob's ladder. Based on these orbitals, additional corrections to the correlation energy are calculated by second order perturbation theory. Functionals that combine the hybrid GGA approach and contributions from wavefunction–based methods are called double hybrid functionals.

LC–GGA functionals, also called range–separated hybrid (RSH) functionals, are methods in which the exchange energy term is split into long–range (LR) and short–range (SR) contributions.[51, 52] This can be achieved by the use of the standard error function[53] that governs the mixing of local DFT exchange and nonlocal HF exchange:

$$\begin{gathered}\frac{1}{u} = \frac{1 - erf(\omega u)}{u} + \frac{erf(\omega u)}{u} \\ u = |\mathbf{r}_1 - \mathbf{r}_2|\end{gathered} \tag{19}$$

The splitting of the Coulomb operator according to (19) leads to an exchange–correlation (XC) functional that is dependent on the mixing parameter ω:

$$E_{XC}^{LC-DFT} = E_X^{SR-DFT}(\omega) + E_X^{LR-HF}(\omega) + E_c^{DFT} \tag{20}$$

For large u the entire exchange energy is coming from the LR–HF part of (20) and the correct asymptotic behavior is obtained.

Kronik and coworkers[54–56] showed that the description of the fundamental gap is enhanced when the ω parameter is tuned specifically for the investigated system. As the determination of the fundamental gap requires accurate ionization potential (IP) and electron affinity (AE), the ω parameter is chosen such that Koopmans'

theorem is obeyed as closely as possible for the IP of the system (N) and the IP of the corresponding anion (N+1). The IP of the anion is approximately equal to the AE when relaxation effects are neglected. As in exact Kohn–Sham theory the highest–occupied (HO) Kohn–Sham eigenvalue, i.e. the HOMO energy ε_{HOMO}, is equal and opposite to the IP[57, 58], the following expression needs to be minimized in order to tune ω:

$$\begin{gathered} J(\omega) = |\varepsilon^{\omega}_{HOMO}(N) + IP^{\omega}(N)| + |\varepsilon^{\omega}_{HOMO}(N+1) + IP^{\omega}(N+1)| \\ \text{with } IP^{\omega}(N) = E_0(N-1,\omega) - E_0(N,\omega) \end{gathered} \tag{21}$$

The term E_0 is the ground state energy of the respective system. Consequently, the ground state energy has to be calculated for the original (N), the singly reduced (N+1) and singly oxidized (N-1) system.

Recently, Engels and coworkers[59, 60] showed that time-dependent (TD) DFT calculations with the use of an optimally tuned RSH functional give excellent agreement with experimental data for organic semi–conductors. The reason for the improvement is argued to be the result of the more accurate ionization potentials of the system which in turn refines the description of charge transfer (CT) states. It was shown that experimental absorption spectra represent bands of excitations with considerable CT character. Therefore, if accurate peak assignment and in–depth understanding of the corresponding photo physics is desired, IP tuning seems to be mandatory.

2.3 The ONIOM Method

When the chemical system of interest is too large to employ a pure electronic structure method, there are typically two approaches to model the problem. One way to tackle a prohibitively large system is to reduce its size by focusing on the parts of the molecules which are important to the investigated phenomenon. For instance, if spectroscopical properties of a chromophore are to be elucidated, it can be a sound choice to truncate certain residues like extensive alkyl chains and replace them by methyl groups. Oftentimes these residues are necessary from a synthetic point of view, e.g. to improve solubility, but they have little influence on the electronic transitions of the chromophore and therefore can be omitted in excited state calculations. However, in some cases the size of the system can not be reduced to an effective model system, because environmental effects play an important role in the investigated chemistry. This is the case for systems such as enzymes, where the active site in which reactions take place is small in comparison to the entire protein.

But nevertheless, the protein backbone can not be omitted in modelling the system, because it holds the reactive residues in place and it might be subjected to changes throughout the reaction. Another possible case is the influence of solvent on a given system. If solvent molecules have to be treated explicitly to capture all important effects, the amount of atoms in the solute and the surrounding solvation shell can easily become too costly for pure electronic structure methods. To deal with these challenges, so–called hybrid or multi–scale methods have been developed. For a comprehensive multi-scale method review the reader can refer to Chung et al.[61] The general idea is to partition the investigated system into a core region which is treated by an expensive quantum mechanical (QM) method and the remaining environment. The environment is then treated with cheap molecular mechanics (MM) or a more affordable, lower–level QM method. Both regions are commonly referred to as layers.

When the first "generic" QM/MM scheme was proposed by Warshel and Levitt in 1976[62], the Hamiltonian was formally divided as follows:

$$\hat{H}_{total} = \hat{H}_{QM} + \hat{H}_{MM} + \hat{H}_{QM/MM} \tag{22}$$

The main problem for multi–scale methods is the description of the interaction between layers $\hat{H}_{QM/MM}$. The simplest way to define this correction term is called mechanical embedding.[63] For mechanical embedding, the electronic parts of the two layers do not interact with each other. However, the QM atoms experience additional forces by the MM framework and vice versa. The resulting non–bonded energy expression can be illustrated by a Lennard–Jones potential[30]

$$\hat{H}_{QM/MM} = \sum_{a}^{N_{MM}} \sum_{b}^{N_{QM}} \varepsilon_{ab} \left[\left(\frac{R_0}{R_{ab}} \right)^{12} - 2 \left(\frac{R_0}{R_{ab}} \right)^{6} \right]. \tag{23}$$

Here N_{MM} denotes the atoms in the MM layer and N_{QM} the atoms in the QM layer. Because in this ansatz the QM wavefunction is not polarized by the environment, the mechanical embedding scheme is a rather crude approximation. It can be improved if the electric potential of the MM layer is included in the QM Hamiltonian by addition of a $\hat{V}_{QM/MM}$ term to the one–electron matrix elements[30]:

$$\hat{V}_{QM/MM} = \sum_{a}^{N_{MM}} \frac{Q_a}{|\mathbf{R}_a - \mathbf{r}_i|} \tag{24}$$

Q_a denotes the partial charges of the MM atoms from the MM calculation and $\mathbf{r}_i$ the electron coordinate in the QM calculation. The inclusion of this term in the QM

Hamiltonian is called electrostatic embedding.

Because the $\hat{H}_{QM/MM}$ term has to account for the entire coupling of the QM and MM layer, it is not easily defined. A simpler approach is used in the ONIOM[64] (Our Own N-layered Integrated Molecular Orbital and Molecular Mechanics) scheme. The energy of the total system in the two-layered ONIOM scheme is calculated as follows:

$$E_{total} = E_{QM,model} + E_{MM,real} - E_{MM,model} \tag{25}$$

This approach is called subtractive scheme, in contrast to the original additive scheme in (21). In a subtractive scheme, the system is also divided in a model system, i.e. the QM layer, and the environment. Importantly, the environment is not calculated separate of the model system as it is the case for the generic QM/MM scheme. Instead, the model system is included in the MM calculation, which now consists of the entire, real system. To remove the double counting of MM contributions, the model system is calculated both with the QM as well as the MM method and the latter is subtracted in the total energy expression. In principle, the subtractive scheme allows for the implementation of an arbitrary number of layers, which is not possible with the additive scheme.

The separation of a system in different layers is straight-forward when there is no covalent bond at the layer boundary, as it is usually the case when e.g. the solvation shell is considered. For systems like proteins the treatment of the layer boundary is not trivial, as the layers are connected by covalent bonds. There are several possibilities to avoid issues like ”dangling” bonds, i.e. radicals in the QM region.[61] One of which is the link atom approach[65], where the radical site is saturated by a link atom, oftentimes a H atom. Another way is to localize and freeze the orbitals at the radical sites, as it is the case for the localized self–consistent field (LSCF) method by Ferenczy et al.[66]

2.4 The Nudged Elastic Band Method as Important Tool in Reaction Mechanism Investigations

The Nudged Elastic Band (NEB)[67] method by Jónsson and coworkers is a powerful tool in exploring the potential energy surface (PES) of a system. More specifically, it assists in finding the minimum energy path (MEP) between two local PES minima. In principle, this can also be achieved by so–called relaxed scans along one or more coordinates x. The one–dimensional coordinates x in the Z matrix representation, i.e. interatomic distances, angles and dihedrals, are assumed to be closely related to the multi–dimensional reaction coordinate that spans all coordinates of the system

and connects the PES minima of interest. The coordinate x is fixed at certain increments while the rest of the system is optimized, i.e. relaxed. When the scan is divided in n increments or steps for each coordinate x and more than one coordinate is considered, the amount of required optimizations scales as n to the power of the number of coordinates. Therefore, a relaxed scan approach is viable if the geometry change along the reaction coordinate is mainly associated with one or two one–dimensional coordinates. If the geometry change along the reaction is more complex, it is challenging to obtain the MEP by relaxed scans. Another draw–back of this approach is the inherent bias of the choice of scan coordinates. It might result in finding a path that is higher in energy than the MEP. The NEB method avoids these problems, as no specific coordinates are required. Instead, a guess MEP is extrapolated between the starting structure R_0 and the final structure R_N which is divided by N–1 intermediate structures called "images". The sum over the energies of all images R_i plus a penalty term defines the target function, i.e. the elastic band[67]:

$$T_{NEB}\left(R_0,\ldots,R_i,\ldots,R_N\right) = \sum_{i=1}^{N-1} E\left(R_i\right) + \sum_{i=1}^{N-2} \frac{1}{2} k_i \left(R_{i+1} - R_i\right)^2 \tag{26}$$

The penalty term which is dependent on the spring constant k is distributing the images along the path. If the same k is chosen for each image, the distribution is equidistant. The MEP is then achieved by minimizing the T function with respect to the coordinates R_i. However, the result of optimizing T straight-forwardly depends on the choice of k. For large k the final path tends to "cut corners" of the PES, whereas for small k the images might be driven to the PES minima R_0 and R_N.[30] This problem can be avoided by "nudging" the elastic band. The effective force F_i^{eff} on an image R_i is then calculated by:

$$F_i^{\text{eff}} = F_i^{\perp} + F_i^{sp,\parallel} \tag{27}$$

$F_i^{\perp}$ is the component of the atom force F_i that is perpendicular to the tangent τ of the path, while $F_i^{sp,\parallel}$ is the component of the spring force that is parallel to τ:

$$\begin{aligned} F_i^{\perp} &= F_i - (F_i \cdot \tau_i)\tau_i \\ F_i^{sp,\parallel} &= \left(k_i|R_{i+1} - R_i| - k_{i-1}|R_i - R_{i-1}|\right)\tau_i \\ \tau_i &= \frac{R_{i+1} - R_i}{|R_{i+1} - R_i|} + \frac{R_i - R_{i-1}}{|R_i - R_{i-1}|} \end{aligned} \tag{28}$$

τ_i is simply the linear combination of the vectors that connect from images R_{i+1} and

R_{i-1} to image R_i.

While the NEB method eliminates the dependency of the MEP search on specific coordinates, a new problem arises. To achieve a fast–converging NEB calculation, a reasonable guess for the initial MEP is important. One possibility to generate a discrete MEP guess is the linear extrapolation of the cartesian coordinates from R_0 to R_N. But, if the reaction involves e.g. rotations of atoms around a certain axis, a linear extrapolation will yield images in which the atoms will be unphysically pushed towards the axis. This can result in overlapping atoms and cause the calculation to fail. A better choice for guess generation is the image dependent pair potential (IDPP)[68] method by Jónsson and coworkers. First, the ideal interpolated distances r_{ab}^i between atoms a and b at positions r_a and r_b in an image R_i are calculated:

$$\begin{aligned} r_{ab}^i &= r_{ab}^0 + i(r_{ab}^N - r_{ab}^0)/N \\ r_{ab} &= |\vec{r}_a - \vec{r}_b| \end{aligned} \tag{29}$$

There are way more pairwise distances than atom coordinates, which means that the interpolated values of the atom coordinates cannot satisfy the constraints rigorously. Therefore, the extrapolated IDPP path is found by minimizing the objective function

$$S_i^{IDPP}(R_i) = \sum_{a}^{N_{atoms}} \sum_{b>a}^{N_{atoms}} \omega(r_{ab}) \left(r_{ab}^i - r_{ab}\right)^2 \tag{30}$$

ω is a weight function which gives more weight to short distances, since the energy of an atomic system rises strongly when two atoms come too close together. Because the optimization of the S function is performed for each image, the procedure is analogous to a NEB calculation on an effective energy surface defined by S. Since no electronic structure computations are needed, the IDPP method requires very little computational effort.

3 Multifaceted Behavior of a Doubly Reduced Arylborane in B–H–bond Activation and Hydroboration Catalysis

This paper was published in S. E. Prey, C. Herok, F. Fantuzzi, M. Bolte, H.–W. Lerner, B. Engels, M. Wagner, *Chemical Science* **2023**, *14*, 849–860.
From the electronically available Supporting Information (ESI) only the section regarding the quantum chemical calculations is reprinted.

Reproduced from [69] with permission from the Royal Society of Chemistry.

When Sven Prey from the Wagner group in Frankfurt embarked on the investigation of diboraanthracene(DBA)–mediated hydroboration reactions, little was known about the underlying reaction mechanisms. Prof. Matthias Wagner approached the Engels group to elucidate the process for which only little experimental indications were found. Essentially two different types of reactivity of the DBA scaffold were observed, depending on the substrate (*vide infra*). During the hydroboration of *N*–*t*Bu–benzylimine, the product of a B–H bond activation at the DBA moiety was observed. All other unsaturated substrates underwent [4+2]–cycloaddition to the central DBA heterocycle, forming adducts that persisted throughout the hydroboration process. With only the X–ray data of the compounds corresponding to the first respective reaction step in hand, we began proposing and investigating possible reaction mechanisms by means of DFT. Initially, the work was focused on the special case of the *N*–*t*Bu–benzylimine hydroboration, as the formation of a new B–B bond in the process sparked our interest. During the course of our analysis, it became clear that we were missing key intermediates in the reaction cycle. After discussion with our experimental coworkers, we discovered that pinacolborane is prone to decomposition in a reductive environment. Taking this into account, we proposed the final "hidden" catalysis mechanism which is included in the publication. Additionally, as the calculations indicated that free BH_3 should be present in the reaction mixture, we requested a test reaction with a borane scavenger. It resulted in the detection of BH_3 during the hydroboration, as predicted. While investigating the first reaction mechanism, preliminary calculations showed that extensive environment modeling was crucial to accurately describe the reaction. Equipped with this knowledge, we found that this was also true for the second reaction mechanism which involved [4+2]–cycloaddition products as catalysts. We showed that the rate determining

step is considerably stabilized by the counterions of the catalytic species, and a reasonable mechanism was proposed.

In summary, the following reprinted publication is the result of a tight collaboration between the Engels and the Wagner group. Frequent discussions and helpful suggestions on both sides brought about profound insight in the multifaceted behavior of the reduced DBA molecule.

All experimental work was performed by Sven Prey at the University Frankfurt, whereas all computational results were contributed by the author of this work.

Chemical Science

ROYAL SOCIETY OF CHEMISTRY

EDGE ARTICLE

View Article Online
View Journal | View Issue

Check for updates

Cite this: *Chem. Sci.*, 2023, **14**, 849

All publication charges for this article have been paid for by the Royal Society of Chemistry

Multifaceted behavior of a doubly reduced arylborane in B–H-bond activation and hydroboration catalysis†

Sven E. Prey,‡[a] Christoph Herok,‡[b] Felipe Fantuzzi,[bc] Michael Bolte,[a] Hans-Wolfram Lerner,[a] Bernd Engels*[b] and Matthias Wagner*[a]

Alkali-metal salts of 9,10-dimethyl-9,10-dihydro-9,10-diboraanthrancene (M_2[DBA-Me_2]; M^+ = Li^+, Na^+, K^+) activate the H–B bond of pinacolborane (HBpin) in THF already at room temperature. For M^+ = Na^+, K^+, the addition products M_2[**4**] are formed, which contain one new H–B and one new B–Bpin bond; for M^+ = Li^+, the H^- ion is instantaneously transferred from the DBA-Me_2 unit to another equivalent of HBpin to afford Li[**5**]. Although Li[**5**] might commonly be considered a $[Bpin]^-$ adduct of neutral DBA-Me_2, it donates a $[Bpin]^+$ cation to Li[$SiPh_3$], generating the silyl borane Ph_3Si–Bpin; Li_2[DBA-Me_2] with an aromatic central B_2C_4 ring acts as the leaving group. Furthermore, Li_2[DBA-Me_2] catalyzes the hydroboration of various unsaturated substrates with HBpin in THF. Quantum-chemical calculations complemented by *in situ* NMR spectroscopy revealed two different mechanistic scenarios that are governed by the steric demand of the substrate used: in the case of the bulky Ph(H)C=N*t*Bu, the reaction requires elevated temperatures of 100 °C, starts with H–Bpin activation which subsequently generates Li[BH_4], so that the mechanism eventually turns into "hidden borohydride catalysis". Ph(H)C=NPh, Ph_2C=O, Ph_2C=CH_2, and *i*PrN=C=N*i*Pr undergo hydroboration already at room temperature. Here, the active hydroboration catalyst is the [4 + 2] cycloadduct between the respective substrate and Li_2[DBA-Me_2]: in the key step, attack of HBpin on the bridging unit opens the bicyclo[2.2.2]octadiene scaffold and gives the activated HBpin adduct of the Lewis-basic moiety that was previously coordinated to the DBA-B atom.

Received 5th October 2022
Accepted 2nd December 2022

DOI: 10.1039/d2sc05518j

rsc.li/chemical-science

Introduction

The activation of chemical bonds by main-group compounds is not only conceptually appealing, but also holds great application potential. A prominent class of p-block catalysts is that of Frustrated Lewis Pairs (FLPs), which contain suitable combinations of sterically encumbered Lewis acids (LA) and bases (LB). Together, these functional units contribute the vacant orbital and electron lone pair which, in classical catalysis, are provided by one single transition metal center with partially filled d orbitals.[1,2] More recently, alternative systems based on doubly boron-doped (hetero)arenes have been reported.[3,4] Common to all of them is a central six-membered ring featuring an aromatic π-electron system and two mutually cooperating B atoms integrated therein at opposite positions. As an example, Kinjo *et al.* disclosed that the 1,3,2,5-diazadiborinine **A** (Fig. 1) adds the single bond of H_3C–OSO_2CF_3, the double bonds of alkenes and carbonyls, as well as the triple bonds of alkynes across its B sites. As mode of action, Kinjo postulated that **A** has a B(I)/B(III) mixed-valence character,[5–7] which would render it formally analogous to an LB/LA FLP. A related 1,4,2,5-diazadiborinine activates H–H, B–H, Si–H, and P–H bonds. Here, it was proposed that the two chemically equivalent B atoms "act as both nucleophilic and electrophilic centers, demonstrating ambiphilic nature".[8,9] Catalytic cycles based on these diazadiborinines have not yet been described, with one notable exception: *in situ*-generated [4 + 2] cycloadducts of **A** and Ph(Me)C=O or H_2C=CH_2 act as "electrostatic catalysts" to promote hydroboration of carbonyl compounds with pinacolborane (HBpin; see Fig. 3 below).[7]

Wagner and coworkers have introduced 9,10-dihydro-9,10-diboraanthracene (DBA) dianions $[DBA\text{-}R_2]^{2-}$ into catalysis (Fig. 1; R = H, Me). These species have indistinguishable, sterically accessible B atoms along with high-lying HOMO-

[a]*Institut für Anorganische und Analytische Chemie, Goethe-Universität Frankfurt, Frankfurt am Main D-60438, Germany. E-mail: matthias.wagner@chemie.uni-frankfurt.de*

[b]*Institut für Physikalische und Theoretische Chemie, Julius-Maximilians-Universität Würzburg, Würzburg D-97074, Germany. E-mail: bernd.engels@uni-wuerzburg.de*

[c]*School of Chemistry and Forensic Science, University of Kent, Canterbury CT2 7NH, UK*

† Electronic supplementary information (ESI) available: Synthetic procedures, NMR spectra, X-ray crystallographic data and computational details. CCDC 2207512–2207520. For ESI and crystallographic data in CIF or other electronic format see DOI: https://doi.org/10.1039/d2sc05518j

‡ These authors contributed equally.

View Article Online
Chemical Science
Edge Article

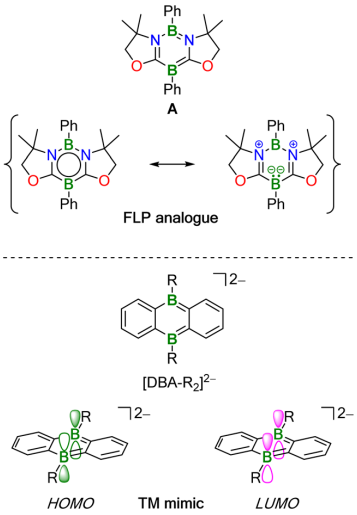

Fig. 1 (Top) 1,3,2,5-Diazadiborinine **A** can be regarded as B(I)/B(III) mixed-valence system, which activates substrate molecules in a similar manner to LB/LA-FLPs. (Bottom) The frontier orbital symmetries of the 9,10-dihydro-9,10-diboraanthracene (DBA) dianion $[DBA\text{-}R_2]^{2-}$ allow concerted transition metal-like (TM-like) reactions.

energy levels and are therefore particularly reactive. Apart from reacting with H–H and C–H bonds, $[DBA\text{-}R_2]^{2-}$ dianions undergo facile [4 + 2] cycloaddition with various unsaturated organic molecules.[10–14]

The HOMO and LUMO of $[DBA\text{-}R_2]^{2-}$ have the same local symmetries about the B atoms as, respectively, the LUMO and HOMO of H_2, and quantum-chemical calculations suggest a concerted, transition metal-like (TM-like) bond-cleavage pathway (Fig. 1).[11] H_2 activation by $[DBA\text{-}R_2]^{2-}$ is at the core of two recently developed catalytic hydrogenation- and H^--transfer cycles.[13] In addition, it has been shown that $[DBA\text{-}R_2]^{2-}$ can catalyze the disproportionation of CO_2 to CO and $[CO_3]^{2-}$.[12,15]

In a joint experimental and theoretical effort, we are herein unveiling the capacity of the $[DBA\text{-}R_2]^{2-}$ platform to activate B–H bonds and catalyze hydroborations. Besides our system, there are also numerous FLPs that catalyze hydroborations. Various modes of action have been discussed.[16] The hydroboration reaction is therefore an ideal tool to put into context the behavior of $[DBA\text{-}R_2]^{2-}$ dianions with those of other main group catalysts and to learn more about the subtleties of subvalent boron species.

Three key results are disclosed: (i) HBpin activation by $[DBA\text{-}R_2]^{2-}$ is a means of forming new B–B bonds. (ii) Depending on the steric bulk of the substrate, the hydroboration mechanism differs between "hidden borohydride catalysis"[17] and actual DBA-driven catalysis. (iii) To gain accurate theoretical insights into the mechanisms, one must explicitly include the counter cations and their coordinating solvent molecules in the calculations, since simple continuum approaches are too imprecise.

Results and discussion

All reactions were performed in (deuterated) tetrahydrofuran (THF, THF-d_8).

Activation of HBpin by $M_2[DBA\text{-}R_2]$

Pinacolborane (HBpin) was selected as the hydroboration reagent for the following reasons: (i) in contrast to, *e.g.*, B_2H_6 or $(9\text{-BBN})_2$ (BBN = 9-borabicyclo[3.3.1]nonane), HBpin is strictly monomeric[18] and does not form solvent adducts in THF, which facilitates the theoretical assessment of its reactivity. (ii) The alkyl boronic ester products (R′–Bpin) are comparatively stable to air and moisture, easy to purify, and have a wide range of applications.[19] The aforementioned assets are the result of pronounced O=B π donation, decreasing the electrophilicity of the B atom. On the other hand, less Lewis-acidic boranes are less prone to spontaneous addition to unsaturated substrates, so that a catalyst is often required. Thus, hydroboration reactions with HBpin provide the ideal setting to further explore the scope of $M_2[DBA\text{-}R_2]$-mediated reactions.

Our investigations into the activation of HBpin by $M_2[DBA\text{-}R_2]$ were carried out with $M^+ = Li^+\text{–}K^+$ as counter cations and R = H, Me as B-bonded substituents (Li_2[**1**]–K_2[**1**], Li_2[**2**]–K_2[**2**]; Scheme 1). In all cases, the reaction with HBpin was already instantaneous at room temperature, as judged by the rapid fading of the intensely colored $M_2[DBA\text{-}R_2]$ solutions after addition of the borane ($M^+ = Li^+$: red; $M^+ = Na^+$, K^+: green). According to *in situ* NMR spectroscopy, 1 equiv. of HBpin was sufficient to quantitatively convert Na_2[**1**], K_2[**1**], and K_2[**2**] to

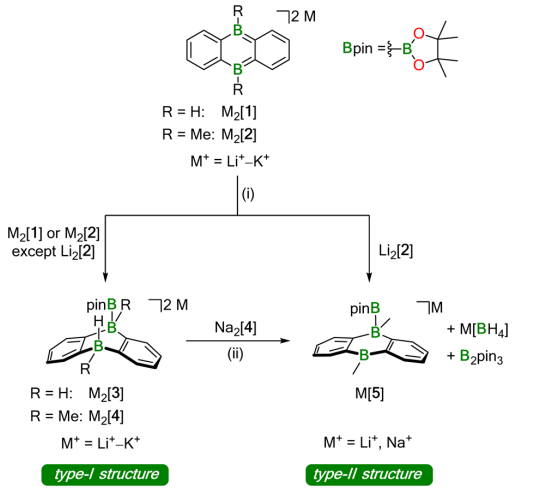

Scheme 1 Addition of pinacolborane (HBpin) across the two B atoms of 9,10-dihydro-9,10-diboraanthracene (DBA) dianions to form B–B bonds. Depending on the nature of the counter cations, the dianionic type-I structures compete with monoanionic type-II structures, which are formed by transfer of the H^- ligand onto a second equivalent of HBpin. (i) 1–5 equiv. HBpin (see ESI†), THF-d_8, room temperature; (ii) prolonged storage in 1,2-dimethoxyethane (DME) during crystallization experiments.

Na_2[**3**], K_2[**3**], and K_2[**4**], respectively, featuring newly formed B–H and B–Bpin bonds together with two tetracoordinate B centers on their DBA cores (type-I structures; Scheme 1). In contrast, equimolar mixtures of Li_2[**1**] or Na_2[**2**] with HBpin contained Li_2[**3**] or Na_2[**4**] and significant amounts of still unconsumed starting materials. Full conversion of the DBA-dianion salts to the corresponding type-I addition products required the use of excess HBpin. These $[DBA\text{-}R_2]^{2-}$-reactivity trends are the same as those previously reported for H_2 activation:[13] (i) M^+ ions with larger charge-radius ratio have a higher tendency to form contact–ion pairs with $[DBA\text{-}R_2]^{2-}$ in solution, which leads to the reactivity order $Li_2[DBA\text{-}R_2] < Na_2[DBA\text{-}R_2] < K_2[DBA\text{-}R_2]$.[11] (ii) Smaller B-bonded substituents R impede substrate access to $[DBA\text{-}R_2]^{2-}$ less than bulkier groups, resulting in the reactivity order $[\mathbf{2}]^{2-} < [\mathbf{1}]^{2-}$.

The accordingly least reactive Li_2[**2**] is indeed a peculiarity, since a type-I product (putative Li_2[**4**]) could not even be detected as an intermediate. Rather, the monoanion salt Li[**5**] was formed without H^- ligand at the DBA moiety (type-II structure; Scheme 1). Again, an excess of HBpin was necessary to enforce quantitative transformation of Li_2[**2**] to Li[**5**], which is accompanied by a formal release of LiH. According to quantum-chemical calculations, this would be an energetically unfavorable process[20,21] and it is, therefore, reasonable to assume that excess HBpin acts as H^- scavenger. The NMR-spectroscopically observed formation of $[BH_4]^-$ and B_2pin_3 (ref. 22) supports this assumption, since H^- is known to induce a corresponding decay of HBpin.[17] In summary, we propose that Li_2[**2**] and HBpin are in a dynamic addition–elimination equilibrium, which is shifted towards Li[**5**] formation by H^- transfer to HBpin and the subsequent irreversible decomposition of the resulting $[H_2Bpin]^-$ adduct. Consistent with this view, addition of LiH to a THF-d_8 solution of Li[**5**] leads back to Li_2[**2**] and HBpin (NMR-spectroscopic control).

The characteristic NMR data of type-I/II structures are exemplarily discussed with reference to the Na_2[**4**]/Li[**5**] couple. The ^{11}B NMR spectrum of Na_2[**4**] contains three signals. Two of them appear in the chemical shift range of tetracoordinate B nuclei [−22.0 ppm (*B*Bpin), −17.4 ppm (d, $^1J_{BH}$ = 68 Hz, BH)] and the third is characteristic of a tricoordinate B center [42.6 ppm (broad, Bpin)].[23] The $\delta(^{11}B)$ values of Li[**5**] prove the presence of one tetra- and two tricoordinate B atoms [−19.7 ppm (*B*Bpin), 41.6 ppm (Bpin), 61.8 ppm (BC_3)]. Accordingly, only the $^1H\{^{11}B\}$ NMR spectrum of Na_2[**4**] shows the signal of a B-bonded H atom (2.14 ppm). The ^{1}H integral values in the spectra of both Na_2[**4**] and Li[**5**] are consistent with the presence of one Bpin substituent in each of these molecules. In line with the proposed average C_s symmetry of Na_2[**4**] and Li[**5**] in solution, their $^{13}C\{^1H\}$ NMR spectra exhibit only six resonances in the aromatic region. Single crystals of the type-II compound [Li(thf)$_2$][**5**] were grown by gas-phase diffusion of *n*-hexane into a C_6H_6 solution of thf-solvated Li[**5**] (Fig. 2). Attempts at the crystallization also of type-I compounds gave specimens suitable for X-ray diffraction only from 1,2-dimethoxyethane (DME) solutions of thf-solvated Na_2[**4**] (room temperature, 1–2 d). Since X-ray analysis revealed that the crystals consisted of [Na(thf)$_2$][**5**] as opposed to Na_2[**4**] (Fig. 2), it appears that Na_2[**4**] is also susceptible to formal NaH elimination (triggered by residual HBpin under the crystallization conditions). The DBA moiety of [Na(thf)$_2$][**5**] has one sp^3-hybridized [B(1)] and one sp^2-hybridized B atom [B(2); $\sum(\measuredangle CBC) = 360.0°$]. At B(1), the Bpin substituent is attached in an axial position and with a bond length of B(1)–B(3) = 1.731(9) Å.[24] The $[Na(thf)_2]^+$ cation is coordinated by an O atom belonging to Bpin and by the centroid of a phenylene ring, creating a contact–ion pair. The solid-state structure of [Li(thf)$_2$][**5**] does not merit further discussion, given that it differs from that of [Na(thf)$_2$][**5**] mainly in details of cation–anion association.[20]

Reactivities of M_2[DBA-R_2]/HBpin addition products

Hydridoborate ions $[R_3B\text{–}H]^-$ and negatively charged adducts $[R_3B\text{–}Bpin]^-$ are widely used sources of H^- and $[Bpin]^-$ nucleophiles, respectively.[25,26] Type-I compounds such as Na_2[**4**] provide both functionalities in the same molecule, which raises the question of whether H^- or $[Bpin]^-$ are preferentially transferred to, *e.g.*, chlorosilanes as archetypal electrophiles. Treatment of freshly prepared Na_2[**4**] with 1 equiv. of Et_3SiCl resulted in selective H^- abstraction to form Na[**5**] and Et_3SiH, showing that H^- wins the competition [*cf.* abstraction of MH by HBpin during the formation of M[**5**] ($M^+ = Li^+, Na^+$)]. What about the possibility of $[Bpin]^-$ transfer in the absence of a competing H^- ion? We have found that Li[**5**] is inert to Et_3SiCl, Et_3SiBr, and MeI at room temperature for several days and therefore does not

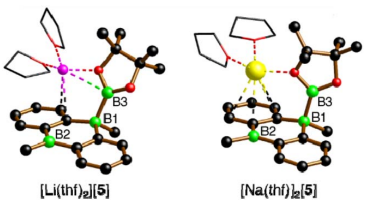

Fig. 2 X-ray-crystallographically derived solid-state structures of the solvates [Li(thf)$_2$][**5**] and [Na(thf)$_2$][**5**], featuring one B–Bpin bond. C-bonded H atoms are omitted for clarity; the thf ligands are simplified as wireframes; Li: pink, B: green, C: black, O: red, Na: yellow spheres.

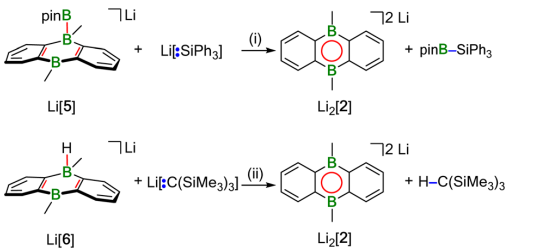

Scheme 2 Reactions of Li[**5**] and Li[**6**] with an Si-centered nucleophile and a C-centered Brønsted base to demonstrate transfer of $[Bpin]^+$ and H^+ along with the suitability of $[\mathbf{2}]^{2-}$ as leaving group. (i) THF-d_8, room temperature, overnight; (ii) THF-d_8, 115 °C, 35 h.

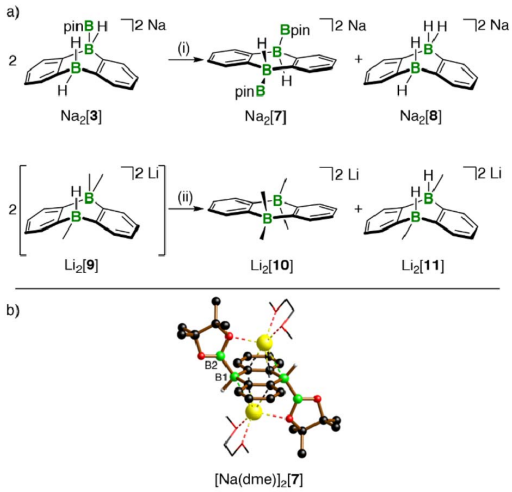

Scheme 3 (a) Substituent-redistribution reaction at Na_2[**3**] producing Na_2[**7**] with two B–Bpin bonds. Substituent-redistribution reaction at Li_2[**9**] leading to the pair of more symmetric compounds Li_2[**10**]/Li_2[**11**]. (b) X-ray-crystallographically derived solid-state structure of the solvate [Na(dme)]$_2$[**7**], featuring two B–Bpin bonds. C-bonded H atoms are omitted for clarity; the dme ligands are shown as wireframes; B: green, C: black, O: red, Na: yellow spheres. (i) DME, room temperature, prolonged storage during crystallization experiments; (ii) THF-d_8, room temperature.

appear to be a $[Bpin]^-$ donor. To probe if a polarity-inverted reactivity is present, Li[**5**] was next combined with the silanide salt Li[$SiPh_3$], which indeed gave pinB–$SiPh_3$ (ref. 27) in a clean reaction.[28] Here, the highly delocalized byproduct $[\mathbf{2}]^{2-}$ turns out to be a good enough leaving group to promote the transfer of a $[Bpin]^+$ electrophile (Scheme 2). To confirm this remarkable result further, we also prepared the formal hydridoborate anion Li[**6**] through H^--adduct formation between the Lewis acid **2** and the H^- source LiH and then removed H^+ by deprotonation of Li[**6**] with Li[$C(SiMe_3)_3$][29] (Scheme 2).[20] Again, $[\mathbf{2}]^{2-}$ is liberated, accompanied by the formation of $HC(SiMe_3)_3$, which renders Li[**6**] a model system of Li[**5**] in which all reactive parts are stripped down to their absolute essence.[30]

The reactions between M_2[**1**]/M_2[**2**] and HBpin described up to this point are not only relevant for H–B-bond activation, but also represent B–B-bond formation reactions off the beaten track. The latter aspect gains additional weight because Na_2[**3**] (one B–B bond) is prone to H^-/$[Bpin]^-$ scrambling, thereby generating a DBA with two B–B bonds: When a DME solution of Na_2[**3**] was stored at room temperature, [Na(dme)]$_2$[**7**] precipitated in single-crystalline form (Scheme 3).

The dianion $[\mathbf{7}]^{2-}$ can be regarded as Lewis pair {**1**·2[$Bpin]^-$}; the necessary byproduct Na_2[**8**][11,13] remained in the mother liquor and was detected by NMR spectroscopy after workup.

The ^{1}H, ^{11}B, and $^{13}C\{^1H\}$ NMR spectroscopic characterization of re-dissolved [Na(dme)]$_2$[**7**] was in line with an average C_{2v} or C_{2h} symmetry but allowed no conclusion regarding a mutual *cis* or *trans* orientation of the two Bpin ligands. The assignment of [Na(dme)]$_2$[**7**] as a C_i-symmetric *trans* complex ($\triangleq$ C_{2h} in solution) was finally achieved by X-ray crystallography (B(1)–B(2) = 1.711(3), Scheme 3). Note that the attempted synthesis of *cis*-Na_2[**7**] from Na_2[**1**] and B_2pin_2 failed, because the two compounds do not react with each other. Also the investigation of the transformation 2 Na_2[**3**] → Na_2[**7**] + Na_2[**8**] was complemented by a model reaction, in which a Me group mimicked the Bpin group of Na_2[**3**] (Scheme 3): Addition of MeLi (1 equiv.) to Li[**6**] did not lead to an NMR-spectroscopically detectable diadduct Li_2[**9**], but rather to an equimolar mixture of the more symmetric Li_2[**10**] and Li_2[**11**][13] scrambling products,[20] the former corresponding to Na_2[**7**].

Taken together, a clear picture of the reactivity trends of the DBA substituents emerges from the model studies, which is of immediate importance with respect to the transfer of H or Bpin fragments onto substrates in the course of hydroboration reactions: a substituent R residing on the tetracoordinate B atom of a B(sp^2),B(sp^3)-DBA can be removed as an R^+ fragment because the formerly B–R-bonding electron pair subsequently becomes part of a Clar's sextet[31] within the central B_2C_4 ring. However, in a B(sp^3),B(sp^3)-DBA, this energetically favorable electron delocalization after R^+ transfer is blocked by the second tetracoordinate B atom, which is why the same R now possesses mainly R^- character.

Hydroboration reactions

The substrates under investigation contained less polar (C=C) as well as more polar (C=N, C=O) double bonds and possessed different steric demands (*e.g.*, Ph(H)C=NPh < Ph(H)C=N*t*Bu). Hydroborations were regularly performed with a loading of 25 mol% Li_2[**2**] to facilitate the NMR-spectroscopic detection of reaction intermediates, side products, and byproducts; in the selected case of Ph_2C=O, it was confirmed that a Li_2[**2**] loading of 5 mol% is sufficient for full conversion of the starting materials and thus the reactions are truly catalytic in the DBA. To ensure full comparability, we always added the HBpin to a mixture of freshly prepared Li_2[**2**] and the unsaturated substrate.[32]

Two fundamentally different reaction mechanisms were found to be operative under these conditions.[33] Which of the two comes into play depends decisively on the steric requirements of the substrate. Only in the case of the bulkiest substrate, the imine Ph(H)C=N*t*Bu, does HBpin activation by Li_2[**2**] initiate the transformation; the actual catalytic cycle is a textbook example of "hidden borohydride catalysis".[17] In all other cases, [4 + 2] cycloaddition of the substrates' double bonds occurs prior to HBpin addition; subsequent hydroboration is then catalyzed by the cycloadducts.

Mechanism I: hidden borohydride catalysis. NMR spectra recorded on a freshly prepared mixture of Li_2[**2**], Ph(H)C=N*t*Bu, and HBpin showed the characteristic resonances of the above-mentioned HBpin-activation product Li[**5**], together with the signals of Li[BH_4] and B_2pin_3. The resonances of the imine were still prominently visible, and the spectrum did not indicate transformation of this starting material. The situation remained unchanged for several hours at room temperature.

Yet, heating the sample to 100 °C for 40 h led to 85% conversion of the imine, but it took another 50 h at 100 °C to drive the reaction to completion. The NMR data of the borylamine primary product agreed well with literature data;[34] after *in situ* hydrolysis, we observed the resonances of the free amine $Ph(H)_2C–N(H)tBu$.[13] We took the initial appearance of the $[BH_4]^-$ ion as a warning signal that the present case might be an example of hidden catalysis by the system $BH_3\cdot thf/[BH_4]^-$.[17] Indeed, preliminary quantum-chemical calculations indicated that such a process might be at play (see below for an in-depth theoretical treatment of the reaction mechanism). To substantiate the assumption of hidden borohydride catalysis further, we adapted a test reaction recommended by Thomas and coworkers[17] and repeated the experiment in the presence of *N*,*N*,*N*′,*N*′-tetramethylethylenediamine (TMEDA), which is supposed to act as a BH_3 scavenger. Subsequently, we detected the diagnostic signal of $(BH_3)_2\cdot tmeda$[35] and noted a significantly slower reaction. All in all, this confirmed our working hypothesis that the hydroboration of Ph(H)C=N*t*Bu by HBpin is only initiated by Li_2[**2**], but catalyzed by $BH_3\cdot thf/[BH_4]^-$.

Mechanism II: DBA-cycloadduct catalysis. Hydroborations of Ph(H)C=NPh, Ph_2C=O, and Ph_2C=CH_2 with HBpin in the presence of Li_2[**2**] proceeded quantitatively already at room temperature (Table 1). We found that the key elements of each reaction scenario are the same for all three substrates. It is therefore sufficient to discuss the experimental facts using Ph(H)C=NPh as an example. Imine Ph(H)C=NPh undergoes an instantaneous and quantitative [4 + 2] cycloaddition reaction with Li_2[**2**] to afford the dianionic bicyclo[2.2.2]octadiene derivative Li_2[**12**] (Scheme 4). As a distinct difference, the corresponding cycloaddition with the bulkier Ph(H)C=N*t*Bu is very slow at room temperature (and underlies a dynamic addition–elimination equilibrium at 100 °C).[13] Consequently, under the prevailing reaction conditions, only in the case of Ph(H)C=N*t*Bu is free Li_2[**2**] still available for initial HBpin activation, while in the other cases the actual active species must be a different one. Thus, the different steric demands of Ph(H)C=N*t*Bu and, *e.g.*, Ph(H)C=NPh lead to a bifurcation of the reaction mechanism into Mechanism I and a new Mechanism II.

Probable candidate catalysts under Mechanism II would be the respective [4 + 2] cycloadducts. This assumption is supported by crossover experiments in which the hydroboration of Ph(H)C=NPh was efficiently mediated by pre-formed Li_2[**13**] or Li_2[**14**], obtained from Li_2[**2**] and Ph_2C=O or H_2C=CH_2, respectively. According to *in situ* NMR spectroscopy, the reactions furnished exclusively $Ph(H)_2C–N(Bpin)Ph$ (and no

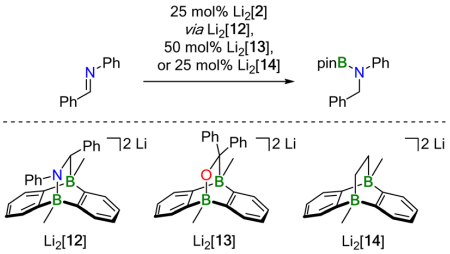

Scheme 4 Crossover experiment to demonstrate that hydroboration of Ph(H)C=NPh with HBpin can be mediated not only by Li_2[**2**] (actual catalyst: Li_2[**12**]), but also by pre-formed Li_2[**13**] or Li_2[**14**] without generating $Ph_2(H)C–OBpin$ or $H_3C–CH_2Bpin$ as crossover side product, respectively (THF-d_8, room temperature). Note that the high catalyst loadings were used for the sole purpose of being able to detect any catalyst degradation or trace formation of crossover products by NMR spectroscopy.

Table 1 Hydroboration of unsaturated substrates proceeding *via* DBA-cycloadduct catalysis

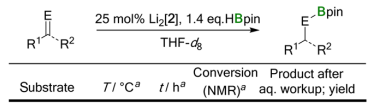

Substrate	*T*/ °C[a]	*t*/ h[a]	Conversion (NMR)[a]	Product after aq. workup; yield
	r. t. (100)	4 (35)	100% (29%)	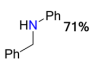 71%
	r. t. (50)	< 0.1 (3)	100% (40%)	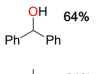 64%
	r. t. (100)	21 (18)	100% (0%)	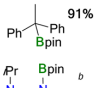 91%
	r. t. (r. t.)	< 0.1 (24)	100% (54%)	 [b]

[a] Numbers in brackets refer to the blind test in the absence of Li_2[**2**]. [b] Pure samples of *i*PrN=C(H)–N(Bpin)*i*Pr were only obtained by sublimation from the reaction mixture, albeit with substantial decrease of the yield.

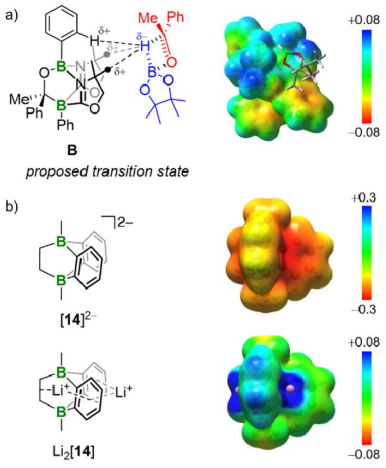

Fig. 3 Comparison of Lewis structures and computed charge densities of (a) Kinjo's bicyclic catalyst **B** and (b) compounds $[\mathbf{14}]^{2-}$ and Li_2[**14**].

View Article Online
Chemical Science Edge Article

$Ph_2(H)C–OBpin$ or $H_3C–CH_2Bpin$), leaving Li_2[**13**] or Li_2[**14**] intact (Scheme 4).

At first glance, the molecular scaffolds of $[\mathbf{12}]^{2-}$, $[\mathbf{13}]^{2-}$, and $[\mathbf{14}]^{2-}$ may appear similar to Kinjo's bicyclic compound **B** (Fig. 3a), which he employed as "electrostatic catalyst" for the hydroboration of various aldehydes and ketones. Here, the key to activation of the H–Bpin bond is believed to lie in electrostatic interactions between the negative partial charge on the borane's H atom and positively polarized regions in the binding pocket of **B**.[7]

However, decisive differences between Kinjo's and our catalysts should arise from (i) the presence of electronegative N and O atoms in **B**, which are (largely) absent in $[\mathbf{12}]^{2-}$, $[\mathbf{13}]^{2-}$, and $[\mathbf{14}]^{2-}$, and (ii) the fact that **B** is a neutral compound whereas our catalysts are dianion salts. A comparison of the computed charge densities of **B**, $[\mathbf{14}]^{2-}$, and Li_2[**14**] confirms this view (Fig. 3b): while positively polarized regions are indeed found in the binding pocket of **B**, they are completely missing in $[\mathbf{14}]^{2-}$. If the Li^+ counter cations are included in the charge-density calculations, positively polarized areas also emerge for Li_2[**14**] but remain largely associated with Li^+. Although the charge distribution in Li_2[**14**] does not directly correspond to the charge distribution in the binding pocket of **B**, it would nevertheless be conceivable that an interaction between the negatively polarized borane-H atom and one of the Li^+ cations could still activate the H–Bpin bond.[36] However, our calculations show that Li^+ and HBpin preferentially interact *via* an O atom (and not the H atom) of the borane (Fig. S93†).[37,38] Kinjo's mechanism is therefore not applicable to our case.

What is a plausible alternative? Although a dynamic equilibrium Li_2[**C**] ⇄ Li_2[**2**] + substrate does not exist at room temperature for the substrates Ph(H)C═NPh, Ph_2C═O, and Ph_2C═CH_2, it is conceivable that HBpin attack induces the reversible cleavage of one E–B(bridgehead) bond of Li_2[**C**] (Scheme 5; E = CH_2, NPh, O). In other words, there may be a competition between the B atoms of DBA and HBpin for the same E^- donor. Precedence exists in the form of the acetone/Na_2[**2**] cycloadduct Na_2[**15**], which straightforwardly inserts CO_2 into its O–B bond to afford Na_2[**16**] (Scheme 5).[12] In the putative

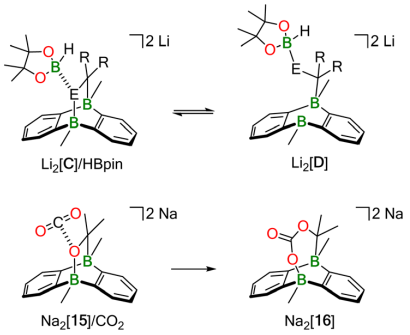

Scheme 5 Conceptual relationship between H–Bpin activation by Li_2[**C**] and CO_2 activation by Na_2[**15**] ($R_2C–E$ = $H_2C–CH_2$, $Ph_2C–CH_2$, Ph(H)C–NPh, $Ph_2C–O$).

negatively charged adduct $[\mathbf{D}]^{2-}$, the electronic situation at the H–B bond should be comparable to the case of, *e.g.*, $[BH_4]^-$. Thus, hydride transfer from $[\mathbf{D}]^{2-}$ to the unsaturated substrate, followed by "$[Bpin]^+$" transfer, would yield the respective hydroboration product and regenerate the catalyst Li_2[**C**]. Like Mechanism I, the essence of Mechanism II has also been confirmed by quantum-chemical calculations (*vide infra*).

Switch between Mechanisms I and II in the double hydroboration of *i*PrN═C═N*i*Pr. The carbodiimide *i*PrN═C═N*i*Pr has two C═N bonds and can therefore be singly or doubly hydroborated. So far, no catalyst has been described to promote both reaction scenarios.[39–43] We now report that Li_2[**2**] can catalyze the monohydroboration of *i*PrN═C═N*i*Pr to give *i*PrN═C(H)–N(Bpin)*i*Pr (room temperature, instantaneous). The reaction is selective even in the presence of 2.4 equiv. of HBpin and proceeds *via* Mechanism II (the moderate steric bulk of the heterocumulene allows formation of its [4 + 2] cycloadduct, which has been fully characterized).[20] Upon heating the sample to 100 °C (23 h), a second hydroboration furnishes *i*Pr(pinB)N–CH_2–N(Bpin)*i*Pr. Due to the larger steric bulk of *i*PrN═C(H)–N(Bpin)*i*Pr compared to *i*PrN═C═N*i*Pr, Mechanism I is operative in the second step (the $[BH_4]^-$ ion was detected by *in situ* NMR spectroscopy).

Quantum chemical calculations

Technical details. Geometry optimizations and Hessian calculations were performed at the ωB97XD/6-31+G(d,p)[44–46] level of theory including implicit solvation by the solvent model based on density (SMD).[47] Our analysis showed that explicit treatment of solvent molecules is crucial to obtain a correct description of entropy contributions along the reaction path as well as reliable kinetic barrier heights. Therefore, the optimal solvent coordination number for each intermediate was determined by free energy calculations (for details, see Fig. S94†). Unless otherwise denoted, optimized geometries were confirmed to be the desired minimum-energy structures or transition states by vibrational frequency analysis. Single-point calculations were performed at the SMD/ωB97XD/6-311++G(d,p) level (solvent: THF; ε = 7.4257). All free-energy values were calculated for the corresponding experimental temperature and included a concentration correction[48,49] that accounts for the change in standard states going from gas phase to condensed phase. All calculations were performed in Gaussian 16, Revision A.03.[50]

Computational characterization of hydroboration Mechanism I. Since well-explored hidden borohydride catalysis plays a prominent role in Mechanism I while our primary interest lies in the characterization of DBA-catalyzed hydroboration reactions, we limited the investigation of Mechanism I to key intermediates and did not calculate kinetic barriers. In order to determine the reaction mechanism, a variety of possible reaction paths was considered (at the experimental temperature of 100 °C).

Since our above-mentioned experimental results exclude direct H^- transfer from Li_2[**4**] to Ph(H)C═N*t*Bu, a corresponding reaction mechanism was not considered theoretically.

Rather, inspired by experiments of Clark and coworkers,[51] we presumed that HBpin would be able to take up the H^- ion provided by Li_2[**4**], forming Li[H_2Bpin], analogous to Clark's reactive species [*t*BuO(H)Bpin]$^-$. HBpin could thereby act as H^- shuttle to Ph(H)C=N*t*Bu. Indeed, this approach led to an overall exergonic reaction (−24 kcal mol^{-1}) with the free energy of the highest-lying intermediate Li[H_2Bpin] being +13 kcal mol^{-1} (Fig. S96†).

Despite its thermodynamic feasibility, this mechanism fails to explain the experimentally observed formation of [BH_4]$^-$ and B_2pin_3. To take these two species into account, we further investigated their formation from decomposition of [H_2Bpin]$^-$.

We first calculated the complete reduction of 1 equiv. HBpin by 3 equiv. Li_2[**4**]. The energetically costly formation of 1 equiv. Li_2[pin] per equivalent of Li[BH_4] generated renders this reaction exceedingly endergonic and thermodynamically out of scope (+36 kcal mol^{-1}, Fig. S95†; H_2pin = pinacol).

As an alternative approach, we propose a stepwise decomposition of Li[H_2Bpin] *via* B–H/B–O σ-bond metathesis with 2 equiv. HBpin (Fig. S97†). Formation of the final products Li[BH_4] and B_2pin_3 is exergonic by −21 kcal mol^{-1}, likely due to the isodesmic nature of this reaction and to the formation of two stable BO_3 motifs. Once formed, Li[BH_4] takes on the role as the actual imine-reducing agent. On this basis, we can now establish a catalytic cycle for hydroboration of Ph(H)C=N*t*Bu by HBpin that is fully consistent with all our experimental results (Fig. 4): in a first step, transition metal-like addition of HBpin to precatalyst Li_2[**2**] affords Li_2[**4**], the starting point of catalytic Cycle I (Fig. 4a, right). While the newly formed B–B bond persists throughout all subsequent reaction steps, the H^- ligand on Li_2[**4**] is transferred to a second HBpin molecule from solution. The free energy of the intermediates Li[**5**] and Li[H_2Bpin] amounts to +19 kcal mol^{-1} when referenced to the starting point of the cycle, Li_2[**4**] (Fig. 4b, right). This energy penalty, which is equivalent to the most endergonic step of the reaction sequence, results from the loss of π conjugation in the H^- carrier Li[H_2Bpin]. As outlined above, decomposition of Li[H_2Bpin] generates Li[BH_4]. In a slightly exergonic reaction,

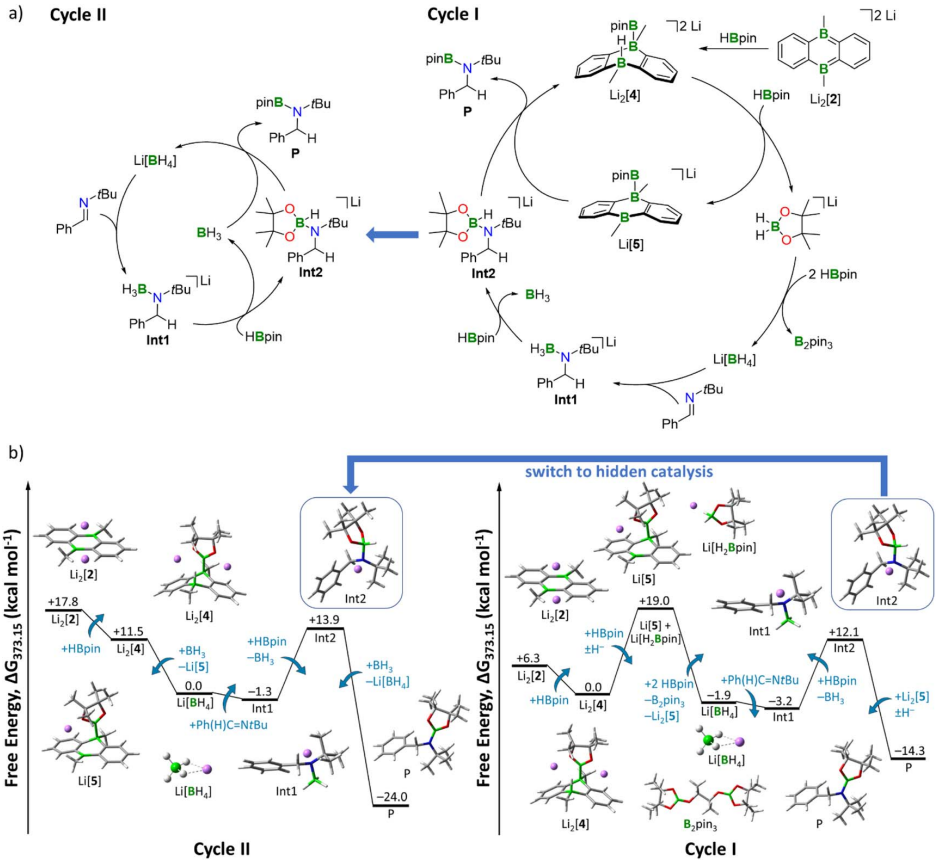

Fig. 4 (a) (Right) Catalytic Cycle I (hydride shuttle: Li[H_2Bpin]). (Left) Catalytic Cycle II, hidden catalysis (hydride shuttle: Li[BH_4]). (b) (Right) Free energy diagram for catalytic Cycle I. (Left) Free energy diagram for hidden catalysis Cycle II including BH_3·thf/Li[BH_4]. Energies are referenced to the starting point of the respective cycle. Level of theory: SMD(solvent = THF)/ωB97XD/6-311++G(d,p) from optimized structures at SMD(solvent = THF)/ωB97XD/6-31+G(d,p). Explicit thf molecules are omitted for clarity.

the double bond of Ph(H)C=N*t*Bu inserts into a B–H bond of $[BH_4]^-$, affording the amide-borane adduct **Int1**. The next step involves a ligand exchange at the negatively charged N atom of **Int1** through nucleophilic attack of **Int1** on HBpin from solution, which releases BH_3·thf and forms **Int2**.[52] **Int2** possesses an activated H–Bpin bond (compare again Clark's intermediate) and thus represents the second highest thermodynamic barrier (+12 kcal mol^{-1}) of Cycle I (Fig. 4b, right). For the last reaction step, there are two possible options, which leads to a bifurcation of the catalytic cycle into Cycles I and II (Fig. 4a). Following Cycle I, Li[**5**] abstracts the H^- ligand from **Int2** in a notably exergonic reaction (−26 kcal mol^{-1}). As a result, the hydroboration product **P** is formed and Cycle I can start anew. The second possibility to produce **P** is H^- transfer from **Int2** to BH_3·thf (generated in the preceding step), thereby entering Cycle II (left panels of Fig. 4a and b). The driving force to **P** is significantly higher along Cycle II (−38 kcal mol^{-1}) than along Cycle I (−26 kcal mol^{-1}). Moreover, since Cycle II starts from Li[BH_4] rather than Li_2[**4**], it bypasses the formation of Li[**5**] and Li[H_2Bpin], the highest-lying intermediate of Cycle I. The steps between the formation of Li[BH_4] and the formation of **Int2** are equivalent in both cycles. Given that BH_3·thf has the highest H^- affinity of all species along Cycles I and II (Table S8†), it will take over the role as H^- shuttle as soon as it is available, effectively making the DBAs Li_2[**4**] and Li[**5**] obsolete. We, therefore, predict that only in the beginning the reaction proceeds with activation of HBpin by Li_2[**2**]. After a few cycles, the mechanism switches to hidden catalysis, where BH_3·thf is the catalytically active species. From this point on, Cycle II outcompetes Cycle I.

Computational characterization of hydroboration Mechanism II. As previously discussed, less sterically demanding substrates than Ph(H)C=N*t*Bu readily form bicyclo[2.2.2]octadiene derivatives by [4 + 2] cycloaddition to Li_2[**2**] at room temperature. For the following reasons, the combination of Ph(H)C=NPh and Li_2[**14**] was chosen as representative model system for our theoretical study: (i) Li_2[**14**] should be the most challenging candidate to evaluate the feasibility of the key ring-opening step in our proposed catalytic mechanism, because, unlike bridging O or NR units, CH_2 fragments do not carry electron lone pairs as obvious sites of attack for incoming HBpin molecules (see Scheme 5). (ii) Li_2[**14**] possesses a symmetric scaffold so that only one kind of reactive center has to be considered.

Our proposed catalytic cycle for the Li_2[**14**]-mediated hydroboration of Ph(H)C=NPh is shown in Fig. 5; the corresponding free energies of the intermediates/transition states along the reaction path are depicted in Fig. 6. Similar to Mechanism I, the first step of Mechanism II is again activation of HBpin, but the actual mode is different: instead of the previously observed transition metal-like cleavage of the H–Bpin bond, the borane is now nucleophilically attacked by a bridging CH_2 group of Li_2[**14**].[53]

As a consequence, the tricyclic scaffold is opened, leading to formation of a tetracoordinate C–(H)Bpin unit and a tricoordinate DBA-B center (**Int3**; Fig. 6). **Int3** lies about +7 kcal mol^{-1} above the reactants. The corresponding barrier (**TS1**) amounts to about +25 kcal mol^{-1}. The activated H^- ligand of the C–(H)Bpin moiety in **Int3** is subject to intramolecular H^- transfer to the tricoordinate DBA-B center. This H^- shift restores the π-conjugated BO_2 motif in the Bpin residue and an electron octet on the DBA-B atom to afford the stabilized intermediate **Int4**, which lies only about +1 kcal mol^{-1} above the reactants. The corresponding barrier (**TS2**) is about +15 kcal mol^{-1} higher in energy than the reactants, *i.e.* considerably lower than the barrier of the first step. **Int4** then acts as an H^- donor to the imine, generating the amide [Ph(H_2)C–NPh]$^-$. The barrier of this step is about +3 kcal mol^{-1} and the resulting **Int5** is −18 kcal mol^{-1} lower in energy than the reactants.[54] [Ph(H_2)C–NPh]$^-$ forms an adduct with the Bpin residue of **Int5**, affording **Int6** (−13 kcal mol^{-1}). The corresponding barrier lies −1 kcal mol^{-1} below the reactants and +17 kcal mol^{-1} above **Int5**. The latter barrier height would have to be overcome if the reaction energy of the **Int4** → **Int5** step is instantaneously dissipated into the solvent. If this is not the case, the barrier associated with **TS4** would in fact be lower. In any case, the barrier of the **Int5** → **Int6** step is at least 8 kcal mol^{-1} lower than the rate-determining **TS1** (+25 kcal mol^{-1}). The catalytic cycle is completed by the restitution of the tricyclic framework of $[\mathbf{14}]^{2-}$ and the simultaneous release of the hydroboration product Ph(H_2)C–N(Bpin)Ph (**P′**). The barrier of this last step is about +3 kcal mol^{-1} above the reactants (+16 kcal mol^{-1} above the previous intermediate) while the exothermicity of the overall reaction is high (−29 kcal mol^{-1}).

As a final remark on key technical details of the calculations, we emphasize that the first step of the mechanism, *i.e.*, nucleophilic attack of the C_2 bridge on HBpin, possesses by far the highest barrier (**TS1**; Fig. 6). It is about +10 kcal mol^{-1} higher

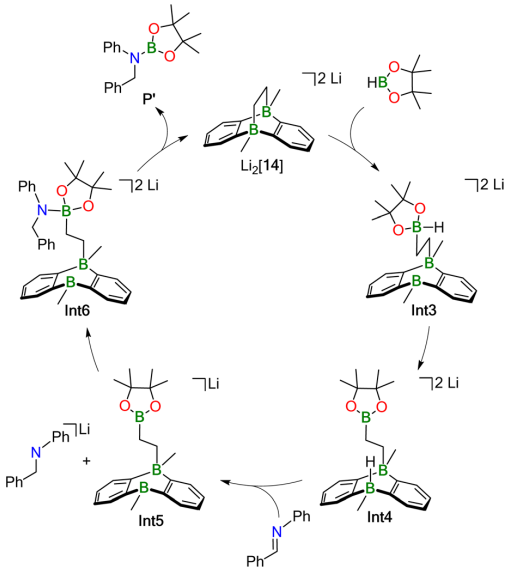

Fig. 5 Hydroboration Mechanism II for less sterically demanding substrates. The corresponding energy diagram is given in Fig. 6.

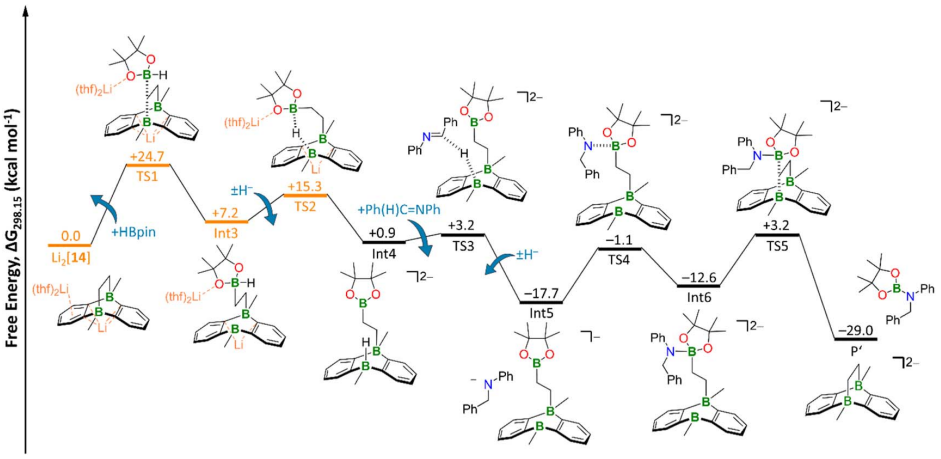

Fig. 6 Free energy diagram of hydroboration Mechanism II. Orange: transition states and intermediate including counterions and explicit solvent molecules. The **TS2** geometry was obtained *via* a relaxed scan (Fig. S100†) and subsequent restricted optimization of the counterions and explicit THF molecules. **TS3** and **TS4** geometries were obtained *via* relaxed scans (Fig. S101 and S102,† respectively). Level of theory: SMD(solvent = THF)/ωB97XD/6-311++G(d,p) from optimized structures at SMD(solvent = THF)/ωB97XD/6-31+G(d,p).

than the second highest barrier (**TS2**) with respect to the reactants. Concerning the respective preceding intermediate, the difference is even larger (+25 kcal mol^{-1} *vs.* +8 kcal mol^{-1}) since **Int3** lies about +7 kcal mol^{-1} above the reactants.

Hence, we investigated the influence of the counterions and their first solvation shell on the performance of the catalyst for both steps in more detail. Rather than modeling the effects of the Li^+ counter cations and explicit THF solvent molecules, we tested the consequences of a mere inclusion of continuum effects by the SMD model. We found the resulting barrier for the trigonal-bipyramidal transition state (**TS1**) to increase by +7 kcal mol^{-1} to +32 kcal mol^{-1}, which is too high considering the experimental conditions. Furthermore, **TS2** is also destabilized by +4 kcal mol^{-1} (Fig. S98†). This effect can be rationalized by considering coordination of the Li^+ cation *via* the O atom of the HBpin molecule. Electron density is thereby withdrawn from the adjacent B center, rendering it more electrophilic and, in turn, facilitating its attack on the electron-rich C_2 bridge of Li_2[**14**]. Furthermore, the tetracoordinate B center in the resulting **Int3** is also stabilized by a $Li^+\cdots O$ interaction (Fig. S98†). Since all other barriers are significantly lower than **TS1** and **TS2**, we calculated them – as well as the corresponding intermediates – without explicit counterions and THF molecules to reduce calculation cost.

Conclusions

We have successfully expanded the range of $[DBA\text{-}Me_2]^{2-}$-catalyzed reactions to include hydroborations with pinacolborane (HBpin; DBA-Me_2 = 9,10-dimethyl-9,10-dihydro-9,10-diboraanthracene). In comparison to analogous hydrogenation reactions, distinct differences become apparent: the general entry step for $[DBA\text{-}Me_2]^{2-}$-catalyzed hydrogenations is H–H-bond addition across the two B atoms of the doubly reduced arylborane. Thus, any competing [4 + 2] cycloaddition reaction between the unsaturated substrate (to be hydrogenated) and the $[DBA\text{-}Me_2]^{2-}$ dianion leads to catalyst poisoning. Although H–Bpin-bond activation with $[DBA\text{-}Me_2]^{2-}$ is also possible, it only plays a role in the hydroboration of sterically loaded substrates such as Ph(H)C=N*t*Bu and proceeds *via* HBpin degradation to $[BH_4]^-$ and B_2pin_3, providing an example of "hidden borohydride catalysis". In all other cases where [4 + 2] cycloaddition to $[DBA\text{-}Me_2]^{2-}$ is not hampered by the steric demands of the substrates (*e.g.*, Ph(H)C=NPh), the cycloadducts are not dead ends, but rather constitute the active hydroboration catalysts. Using the hydroboration of Ph(H)C=NPh with HBpin, mediated by the cycloadduct between $[DBA\text{-}Me_2]^{2-}$ and $H_2C{=}CH_2$, as representative model reaction, we have unveiled the underlying reaction mechanism in a joint experimental and theoretical effort: the 1,2-ethanediyl-bridged tricyclic catalyst can be viewed as intramolecular B–C adduct, in which a Lewis-acidic tricoordinate DBA-B center protects a Lewis-basic $[:CH_2\text{–}CH_2\text{–}B(Me)Ar_2]^{2-}$ fragment to create a stable resting state. In the presence of HBpin, the tricycle can reversibly open to form an HBpin-alkyl adduct in which the H–Bpin bond is activated for H^- transfer to the tricoordinate DBA-B center, from which H^- migrates further to the polar Ph(H)C=NPh bond. The resulting amide $[Ph(H)_2C\text{–}NPh]^-$ takes up $[Bpin]^+$ from $[pinB\text{–}CH_2\text{–}CH_2\text{–}B(Me)Ar_2]^-$ to form $Ph(H)_2C\text{–}N(Bpin)Ph$, thereby regenerating the catalyst and completing the catalytic cycle. According to thorough DFT calculations, our mechanistic proposal is energetically feasible under the experimentally applied reaction conditions (room temperature, THF-d_8, Li^+ counter cations). Quantum-chemical calculations by Kinjo and coworkers have led them to explicitly rule out such a scenario for their related neutral bicyclo[2.2.2]octadienes, assembled from 1,3,2,5-diazadiborinines rather than $[DBA\text{-}Me_2]^{2-}$ dianions.[7] Instead, they postulated

H–Bpin-bond activation through electrostatic interactions with positively polarized regions of the still intact tricyclic catalyst. This comparison clearly demonstrates the multifaceted character of doubly B-doped bicyclo[2.2.2]octadienes and shows how seemingly subtle modifications of their molecular scaffolds can significantly alter their catalytic properties. In the future, it will be interesting to explore what else this class of compounds can contribute to the field of main group catalysis.

Data availability

The datasets supporting this article have been uploaded as part of the ESI.†

Author contributions

S. E. P. performed all preparative experiments. C. H. performed all calculations. M. B. performed the X-ray crystal structure analyses. F. F., H.-W. L, B. E., and M. W. supervised the project. The manuscript was written through contributions of all authors.

Conflicts of interest

There are no conflicts to declare.

Notes and references

1 G. Erker and D. W. Stephan, *Frustrated Lewis Pairs I & II*, Springer, Heidelberg, 2013.
2 A. R. Jupp and D. W. Stephan, *Trends Chem.*, 2019, **1**, 35–48.
3 S. E. Prey and M. Wagner, *Adv. Synth. Catal.*, 2021, **363**, 2290–2309.
4 Y. Su and R. Kinjo, *Chem. Soc. Rev.*, 2019, **48**, 3613–3659.
5 D. Wu, L. Kong, Y. Li, R. Ganguly and R. Kinjo, *Nat. Commun.*, 2015, **6**, 7340.
6 D. Wu, R. Ganguly, Y. Li, S. N. Hoo, H. Hirao and R. Kinjo, *Chem. Sci.*, 2015, **6**, 7150–7155.
7 D. Wu, R. Wang, Y. Li, R. Ganguly, H. Hirao and R. Kinjo, *Chem*, 2017, **3**, 134–151.
8 B. Wang, Y. Li, R. Ganguly, H. Hirao and R. Kinjo, *Nat. Commun.*, 2016, **7**, 11871.
9 B. Wang and R. Kinjo, *Tetrahedron*, 2018, **74**, 7273–7276.
10 A. Lorbach, M. Bolte, H.-W. Lerner and M. Wagner, *Organometallics*, 2010, **29**, 5762–5765.
11 E. von Grotthuss, M. Diefenbach, M. Bolte, H.-W. Lerner, M. C. Holthausen and M. Wagner, *Angew. Chem., Int. Ed.*, 2016, **55**, 14067–14071.
12 E. von Grotthuss, S. E. Prey, M. Bolte, H.-W. Lerner and M. Wagner, *Angew. Chem., Int. Ed.*, 2018, **57**, 16491–16495.
13 E. von Grotthuss, S. E. Prey, M. Bolte, H.-W. Lerner and M. Wagner, *J. Am. Chem. Soc.*, 2019, **141**, 6082–6091.
14 E. von Grotthuss, F. Nawa, M. Bolte, H.-W. Lerner and M. Wagner, *Tetrahedron*, 2019, **75**, 26–30.
15 Harman *et al.* have reported a number of remarkable (catalytic) transformations mediated by Au complexes of bidentate diphosphine ligands with DBA backbones: (*a*) J. W. Taylor, A. McSkimming, M.-E. Moret and W. H. Harman, *Angew. Chem., Int. Ed.*, 2017, **56**, 10413–10417; (*b*) J. W. Taylor, A. McSkimming, L. A. Essex and W. H. Harman, *Chem. Sci.*, 2019, **10**, 9084–9090; (*c*) J. W. Taylor and W. H. Harman, *Chem. Commun.*, 2020, **56**, 4480–4483; (*d*) J. W. Taylor and W. H. Harman, *Chem. Commun.*, 2020, **56**, 13804–13807.
16 (*a*) M. A. Dureen, A. Lough, T. M. Gilbert and D. W. Stephan, *Chem. Commun.*, 2008, 4303–4305; (*b*) P. Eisenberger, A. M. Bailey and C. M. Crudden, *J. Am. Chem. Soc.*, 2012, **134**, 17384–17387; (*c*) D. W. Stephan, *Acc. Chem. Res.*, 2015, **48**, 306–316; (*d*) F.-G. Fontaine, M.-A. Courtemanche, M.-A. Légaré and É. Rochette, *Coord. Chem. Rev.*, 2017, **334**, 124–135; (*e*) P. Vasko, I. A. Zulkifly, M. Á. Fuentes, Z. Mo, J. Hicks, P. C. J. Kamer and S. Aldridge, *Chem.–Eur. J.*, 2018, **24**, 10531–10540; (*f*) A. Falconnet, M. Magre, B. Maity, L. Cavallo and M. Rueping, *Angew. Chem., Int. Ed.*, 2019, **58**, 17567–17571; (*g*) Y. Lebedev, I. Polishchuk, B. Maity, M. Dinis Veloso Guerreiro, L. Cavallo and M. Rueping, *J. Am. Chem. Soc.*, 2019, **141**, 19415–19423; (*h*) D. W. Stephan, *Chem*, 2020, **6**, 1520–1526.
17 A. D. Bage, K. Nicholson, T. A. Hunt, T. Langer and S. P. Thomas, *ACS Catal.*, 2020, **10**, 13479–13486.
18 K. Wade, *Electron Deficient Compounds*, Springer, New York, 1971.
19 I. A. I. Mkhalid, J. H. Barnard, T. B. Marder, J. M. Murphy and J. F. Hartwig, *Chem. Rev.*, 2010, **110**, 890–931.
20 See the ESI† for further details.
21 The free Gibbs energy for the reaction $[Li(thf)_2]_2$[**4**] + THF → $[Li(thf)_2]$[**5**] + $[Li(thf)_3]H$ amounts to +27.4 kcal mol^{-1} at room temperature.
22 W. Clegg, A. J. Scott, C. Dai, G. Lesley, T. B. Marder, N. C. Norman and L. J. Farrugia, *Acta Crystallogr., Sect. C: Cryst. Struct. Commun.*, 1996, **52**, 2545–2547.
23 The ^{11}B NMR signal of the Bpin group in Na_2[**4**] (42.6 ppm; THF-d_8) may seem unusually downfield shifted, as the resonance of B_2pin_2 appears at 32.6 ppm (own measurement in THF-d_8). However, the signals of Bpin groups attached to anionic, tetracoordinate B centers appear in the same range as that of Na_2[**4**] (*cf.* $K[B_2pin_2 \cdot OtBu]$ δ = 41.1; THF-d_8): S. Pietsch, E. C. Neeve, D. C. Apperley, R. Bertermann, F. Mo, D. Qiu, M. S. Cheung, L. Dang, J. Wang, U. Radius, Z. Lin, C. Kleeberg and T. B. Marder, *Chem.–Eur. J.*, 2015, **21**, 7082–7099. The calculated ^{11}B NMR shifts of $[Na(thf)_2]_2$[**4**] are: δ = 45.8 (Bpin), −18.9 (BH), −23.3 (*B*Bpin) (GIAO method at the SMD(solvent = THF)/ωB97XD/6-311++G(d,p) level).
24 Further B–Bpin bond lengths (Å) useful for comparison are (a) B_2pin_2 = 1.7041(15), (b) $[K(18\text{-c-}6)][B_2pin_2OMe]$ = 1.753(2); $[Me_4N][B_2pin_2F] \cdot THF$ = 1.736(8), and (c) $[Mg(HC\{(Me)CN(2,6\text{-}iPr_2C_6H_3)\}_2)][pinB\text{–}BPh_3]$ = 1.718(7): (*a*) C. Kleeberg, A. G. Crawford, A. S. Batsanov, P. Hodgkinson, D. C. Apperley, M. S. Cheung, Z. Lin and T. B. Marder, *J. Org. Chem.*, 2012, **77**, 785–789; (*b*) ref. 23; (*c*) A.-F. Pécharman, M. S. Hill, C. L. McMullin and M. F. Mahon, *Angew. Chem., Int. Ed.*, 2017, **56**, 16363–16366.

25 E. C. Neeve, S. J. Geier, I. A. I. Mkhalid, S. A. Westcott and T. B. Marder, *Chem. Rev.*, 2016, **116**, 9091–9161.
26 A. B. Cuenca, R. Shishido, H. Ito and E. Fernández, *Chem. Soc. Rev.*, 2017, **46**, 415–430.
27 C. Kleeberg and C. Borner, *Eur. J. Inorg. Chem.*, 2013, **2013**, 2799–2806.
28 Li[$SiPh_3$] was chosen as the nucleophile, because its high steric demand disfavors the formation of a stable adduct with the tricoordinate DBA-B atom in Li[**5**]. Moreover, silylboranes such as Ph_3Si–Bpin have considerable application potential: (*a*) T. Ohmura and M. Suginome, *Bull. Chem. Soc. Jpn.*, 2009, **82**, 29–49; (*b*) M. Oestreich, E. Hartmann and M. Mewald, *Chem. Rev.*, 2013, **113**, 402–441; (*c*) S. Bähr, W. Xue and M. Oestreich, *ACS Catal.*, 2019, **9**, 16–24; (*d*) C. Moberg, *Synthesis*, 2020, **52**, 3129–3139; (*e*) K. Hirano and M. Uchiyama, *Adv. Synth. Catal.*, 2021, **363**, 2340–2353; (*f*) J.-J. Feng, W. Mao, L. Zhang and M. Oestreich, *Chem. Soc. Rev.*, 2021, **50**, 2010–2073.
29 G. Becker, H.-M. Hartmann, A. Münch and H. Riffel, *Z. Anorg. Allg. Chemie*, 1985, **530**, 29–42.
30 Quantitative deprotonation of Li[**6**] is also possible using $Ph(H)_2C$–N(Li)*t*Bu as the base. Given that the amide can be formed through H^- transfer to Ph(H)C=N*t*Bu, this deprotonation experiment also marks the hitherto missing keystone of the reaction mechanism previously proposed for the catalytic hydrogenation of the imine by Li_2[**2**]/H_2: In contrast to conventional FLPs, the H_2-activation product Li_2[**11**] (Scheme 3) delivers first an H^- and second an H^+ ion (*cf.* ref. 13).
31 T. Wassmann, A. P. Seitsonen, A. M. Saitta, M. Lazzeri and F. Mauri, *J. Am. Chem. Soc.*, 2010, **132**, 3440–3451.
32 For the following reasons, Li_2[**2**] was chosen despite its somewhat different behavior toward HBpin compared to the other M_2[**1**]/M_2[**2**] compounds: (i) the neutral Me-substituted DBA **2** is more convenient to handle than its H-substituted congener **1**. (ii) We have already published the Li^+ salts of some cycloadducts between $[DBA\text{-}Me_2]^{2-}$ and unsaturated substrates, which are the actual catalytically active species and thus the focus of our mechanistic investigations (*cf.* ref. 12 and 13). (iii) Since our DFT calculations include the counter cations, the computational cost for the treatment of Li^+ is lower than for the treatment of Na^+/K^+.
33 We initially relied on this protocol because it is most similar to the one applied for our earlier hydrogenation reactions (*cf.* ref. 13), which we want to use for comparison. Later, it was found that adding the unsaturated substrate first is essential to exclude contributions of the hidden borohydride catalysis as an undesired background reaction.
34 X. Wang and X. Xu, *RSC Adv.*, 2021, **11**, 1128–1133.
35 A. R. Gatti and T. Wartik, *Inorg. Chem.*, 1966, **5**, 329–330.
36 M. Magre, M. Szewczyk and M. Rueping, *Chem. Rev.*, 2022, **122**, 8261–8312.
37 Sen *et al.* identified a comparable $Li^+\cdots O$ coordination as the key interaction in lithium phenolate-catalyzed HBpin additions to carbonyl compounds. The resulting decrease in O=B π donation leads to an increase in the Lewis acidity of the HBpin molecule and in turn facilitates its interaction with the carbonyl-O atom. We adopted such a scenario to Li_2[**14**] and computed a corresponding reaction barrier of +31 kcal mol^{-1}. Although this value is lower than that of the uncatalyzed reaction by −14 kcal mol^{-1}, it is still higher than **TS1** by +6 kcal mol^{-1}. Since **TS1** represents the highest barrier in our hydroboration Mechanism II (see the ESI† for details), also Sen's mechanism can be ruled out for our case: M. K. Bisai, T. Das, K. Vanka and S. S. Sen, *Chem. Commun.*, 2018, **54**, 6843–6846.
38 Hydroboration of Ph(H)C=NPh with HBpin in THF-d_8 required about the same time, regardless of whether Li_2[**14**] or Na_2[**14**] was used as the catalyst (NMR-spectroscopic control). We take this as justification that Li_2[**14**] is a representative example catalyst to study Mechanism II. It should also be noted that the necessary explicit treatment of the counter cation's coordination sphere is much more complex in the case of the larger Na^+. Its coordination sphere includes six neighbors while the one of Li^+ only contains four. Consequently, not only does the size of the system increase, but also a greater variety of coordination polyhedra can be expected.
39 C. Weetman, M. S. Hill and M. F. Mahon, *Chem.–Eur. J.*, 2016, **22**, 7158–7162.
40 D. Mukherjee, S. Shirase, T. P. Spaniol, K. Mashima and J. Okuda, *Chem. Commun.*, 2016, **52**, 13155–13158.
41 M. D. Anker, M. Arrowsmith, R. L. Arrowsmith, M. S. Hill and M. F. Mahon, *Inorg. Chem.*, 2017, **56**, 5976–5983.
42 A. Ramos, A. Antiñolo, F. Carrillo-Hermosilla, R. Fernández-Galán and D. García-Vivó, *Chem. Commun.*, 2019, **55**, 3073–3076.
43 N. Sarkar, S. Bera and S. Nembenna, *J. Org. Chem.*, 2020, **85**, 4999–5009.
44 J.-D. Chai and M. Head-Gordon, *Phys. Chem. Chem. Phys.*, 2008, **10**, 6615–6620.
45 R. Krishnan, J. S. Binkley, R. Seeger and J. A. Pople, *J. Chem. Phys.*, 1980, **72**, 650–654.
46 T. Clark, J. Chandrasekhar, G. W. Spitznagel and P. von Ragué Schleyer, *J. Comput. Chem.*, 1983, **4**, 294–301.
47 A. V. Marenich, C. J. Cramer and D. G. Truhlar, *J. Phys. Chem. B*, 2009, **113**, 6378–6396.
48 A. Ben-Naim, *J. Phys. Chem.*, 1978, **82**, 792–803.
49 J. R. Pliego Jr and J. M. Riveros, *Phys. Chem. Chem. Phys.*, 2002, **4**, 1622–1627.
50 M. J. Frisch, G. W. Trucks, H. B. Schlegel, G. E. Scuseria, M. A. Robb, J. R. Cheeseman, G. Scalmani, V. Barone, G. A. Peterson, H. Nakatsuji, X. Li, M. Caricato, A. V. Marenich, J. Bloino, B. G. Janesko, R. Gomperts, B. Mennucci, H. P. Hratchian, J. V. Ortiz, A. F. Izmaylov, J. L. Sonnenberg, D. Williams-Young, F. Ding, F. Lipparini, F. Egidi, J. Goings, B. Peng, A. Petrone, T. Henderson, D. Ranasinghe, V. G. Zakrzewski, J. Gao, N. Rega, G. Zheng, W. Liang, M. Hada, M. Ehara, K. Toyota, R. Fukuda, J. Hasegawa, M. Ishida, T. Nakajima, Y. Honda, O. Kitao, H. Nakai, T. Vreven, K. Throssell, J. A. Montgomery Jr, J. E. Peralta, F. Ogliaro,

M. J. Bearpark, J. J. Heyd, E. N. Brothers, K. N. Kudin, V. N. Staroverov, T. A. Keith, R. Kobayashi, J. Normand, K. Raghavachari, A. P. Rendell, J. C. Burant, S. S. Iyengar, J. Tomasi, M. Cossi, J. M. Millam, M. Klene, C. Adamo, R. Cammi, J. W. Ochterski, R. L. Martin, K. Morokuma, O. Farkas, J. B. Foresman and D. J. Fox, *Gaussian 16 (Revision A.03)*, Gaussian Inc., Wallingfort, CT, USA, 2016.

51 I. P. Query, P. A. Squier, E. M. Larson, N. A. Isley and T. B. Clark, *J. Org. Chem.*, 2011, **76**, 6452–6456.

52 Another possible source of Bpin residues is Li[**5**]. Attack of **Int1** at the Bpin substituent of Li[**5**] would lead to the immediate formation of **P** and Li_2[**2**] *via* $[Bpin]^+$ transfer and with release of BH_3·thf (*cf.* the analogous reaction $Li[SiPh_3]$ + Li[**5**] → pinB–$SiPh_3$ + Li_2[**2**]; Scheme 2). According to our calculations this alternative scenario would lead to a decrease in the driving force of the overall reaction from −14 kcal mol^{-1} to −8 kcal mol^{-1}. On the other hand, formation of **Int2** (+15 kcal mol^{-1}) would be bypassed. However, an interaction between the amide anion of **Int1** and negatively charged $[5]^-$ is electrostatically unfavorable and the reactive B(pin) center of $[5]^-$ is sterically less accessible than that of HBpin. We therefore assume that the thermodynamically less favorable formation of **Int2** (+15 kcal mol^{-1}) is preferred by kinetics. Since the formation of Li[**5**] and $Li[H_2Bpin]$, which is the energetically most costly step of Cycle I, is not circumvented, a switch to Cycle II will take place in any case.

53 An analogous attack of a B-bonded Me residue on HBpin or a B–H/B–C σ-bond metathesis leading directly to **Int4** (Fig. 5) can be ruled out due to significantly higher reaction barriers (Fig. S98,† **TSa** and **TSb**).

54 H^- transfer to the alternative electrophile HBpin would be thermodynamically less favorable by +13 kcal mol^{-1}. In general, HBpin appears to be the weakest H^- acceptor of the investigated species (see Table S8†).

7. Additional details on quantum chemical calculations

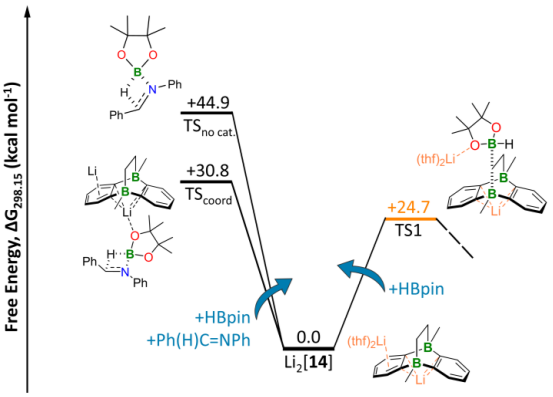

Figure S92. *Syn*-addition of HBpin to Ph(H)C=NPh as alternative hydroboration mechanism. Left: The hydroboration reaction without catalyst is characterized by a high barrier (**TS$_{no\ cat.}$**). Coordination of HBpin by Li_2[**14**] stabilizes the transition state of the *syn*-addition by about –14 kcal mol^{-1} (**TS$_{coord}$**), but the barrier is still too high if experimental reaction conditions are considered. The stabilization of **TS$_{coord}$** is resulting from the electron withdrawing effect of the Li^+ cation which renders the B center of HBpin more electrophilic. Solvation effects are included via the SMD model, but no explicit thf are taken into account. Right: Proposed rate determining step of Mechanism II, including explicit thf molecules (orange).

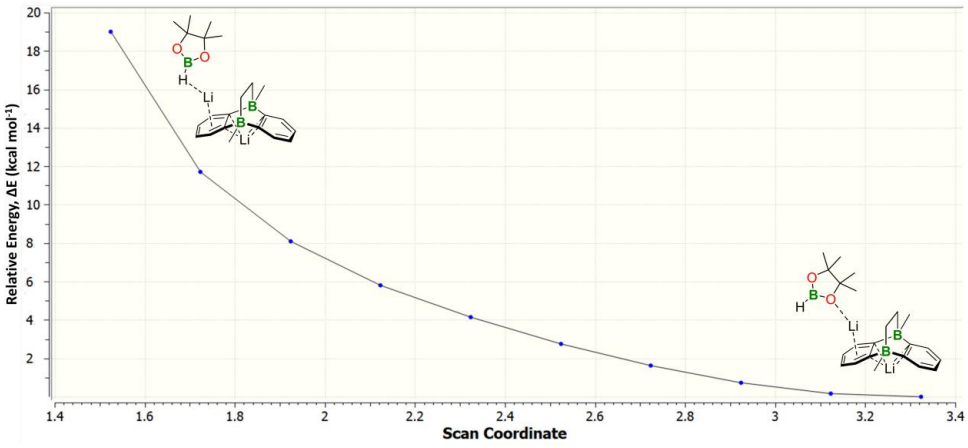

Figure S93. Interaction of HBpin with Li_2[**14**]. Relaxed scan of the H(Bpin)–Li distance.

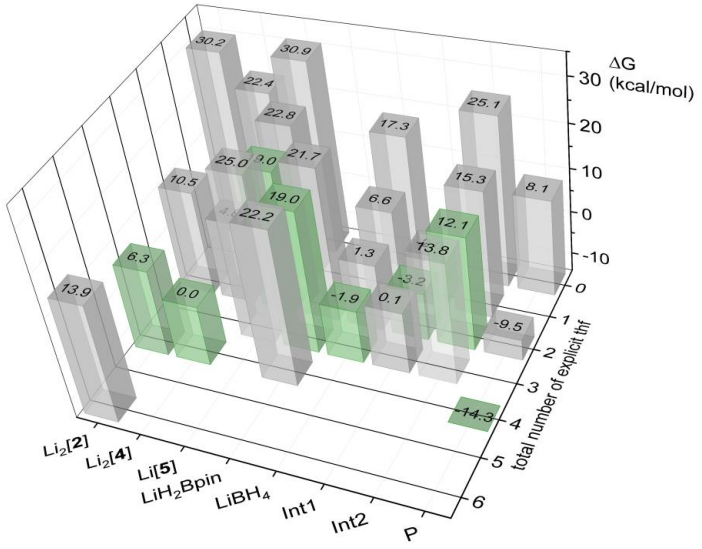

Figure S94. Solvent coordination number for each intermediate determined by free energy calculations. Marked in green: Lowest energy path with optimal coordination number.

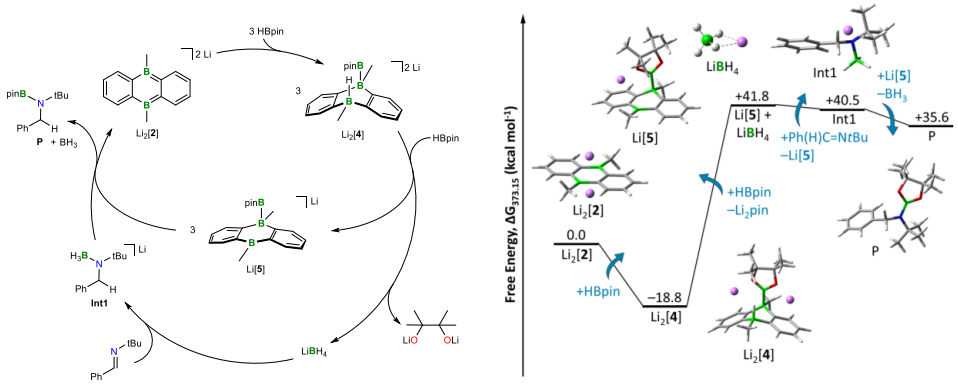

Figure S95. Initial hypothesis for the hydroboration mechanism. Three equivalents of Li_2[**4**] reduce one equivalent HBpin to Li[BH_4] and Li_2[pin]. The formation of Li_2[pin] is exceedingly endergonic. Thus, this mechanism is thermodynamically not possible and can be excluded. Explicit thf molecules are omitted for clarity.

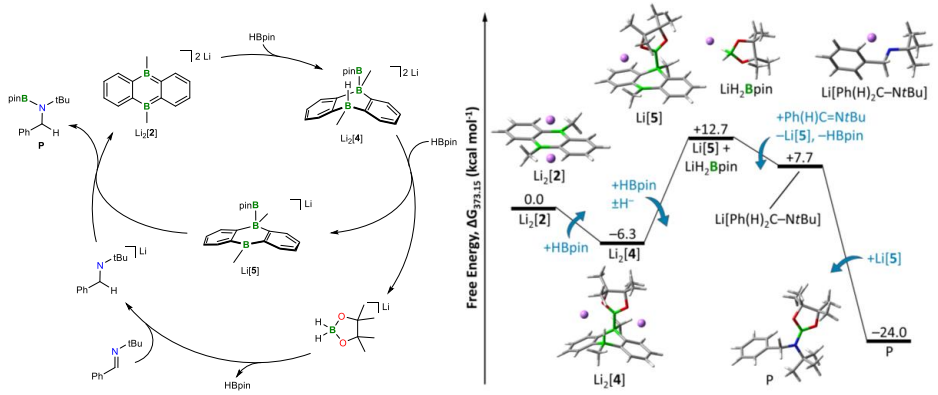

Figure S96. Second hypothetical mechanism without HBpin decomposition. Excess HBpin acts as a hydride shuttle to transport the activated hydride of Li_2[**4**] to the substrate which is subsequently reduced. This mechanism does not explain the formation of $[BH_4]^-$ and can be excluded. Explicit thf molecules are omitted for clarity.

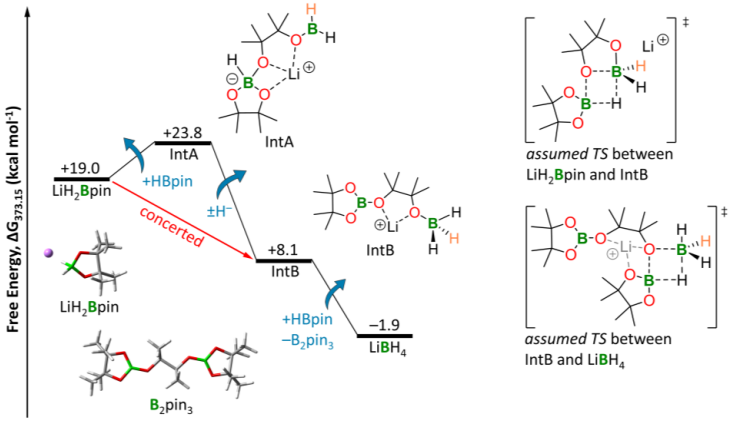

Figure S97. Decomposition of Li[H_2Bpin]. There are two possible ways of starting the decomposition reaction. One way is the formation of **IntA** which is the result of the O atom of Li[H_2Bpin] nucleophilically attacking excess HBpin from solution. Subsequently, the hydride from the destabilized tetracoordinate B center is transferred to the terminal B center, forming **IntB**. Another way is a concerted σ-bond metathesis in which **IntB** is formed directly. In the last step, we assume a second σ-bond metathesis which leads to the formation of the stable side product B_2pin_3 and Li[BH_4]. Explicit thf molecules are omitted for clarity.

Table S8. Hydride Affinities. Free Energies of Hydride Transfer from Li[BH_4] to X at 100°C.

X	Li[HX]	$\Delta G_{373.15}$ (kcal mol^{-1})
BH_3·thf	Li[BH_4]	0.0
Li[**5**]	Li_2[**4**]	+11.5
Ph(H)$_2$C–N(BH_2)*t*Bu	**Int1**	+23.1
Ph(H)C=N*t*Bu	Li[Ph(H)$_2$C–N*t*Bu]	+25.5
HBpin	Li[H_2Bpin]	+30.5

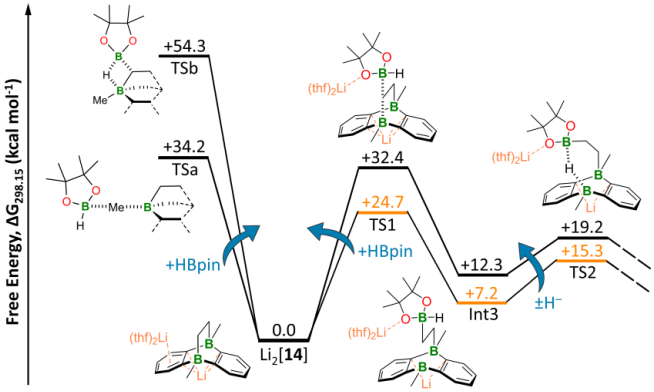

Figure S98. Left: Alternative nucleophilic attacks on HBpin. Right: Comparison of environment modelling (including explicit solvent and counterions, orange) vs SMD calculation without THF and counterions (black). **TSb** geometry was obtained via a relaxed scan (see Figure S98).

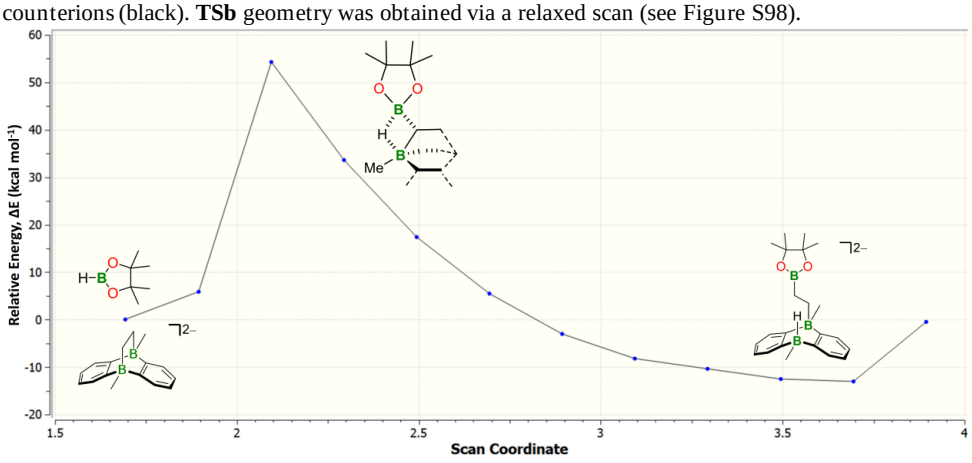

Figure S99. **TSb**: HBpin activation via σ-bond metathesis. Relaxed scan of the C(Bpin)–B(DBA) distance.

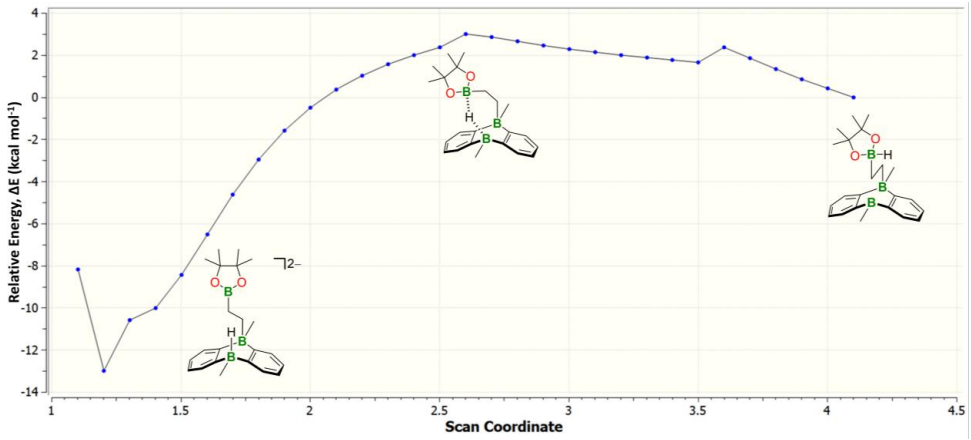

Figure S100. **TS2**: Intramolecular hydride transfer. Relaxed scan of the H(Bpin)–B(DBA) distance.

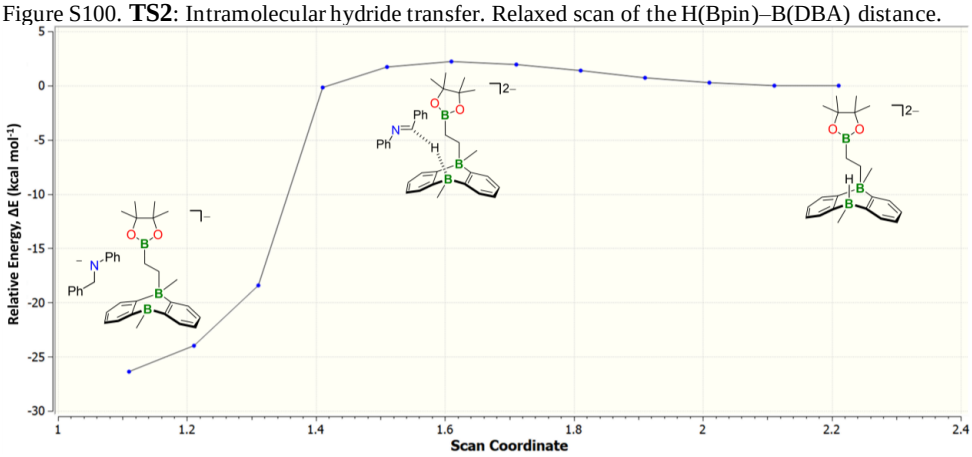

Figure S101. **TS3**: Intermolecular hydride transfer to Ph(H)C=NPh. Relaxed scan of the H(DBA)–C(H)Ph distance.

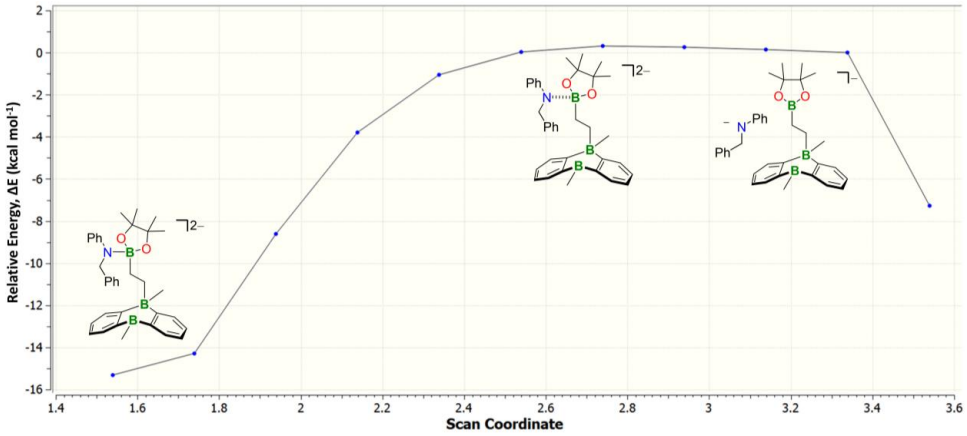

Figure S102. **TS4**: Nucleophilic attack of $[Ph(H)_2C–NPh]^-$ on the B(pin) center. Relaxed scan of the N–B(pin) distance.

4 Benchmark of First–Shell Solvation Effects

4.1 Introduction

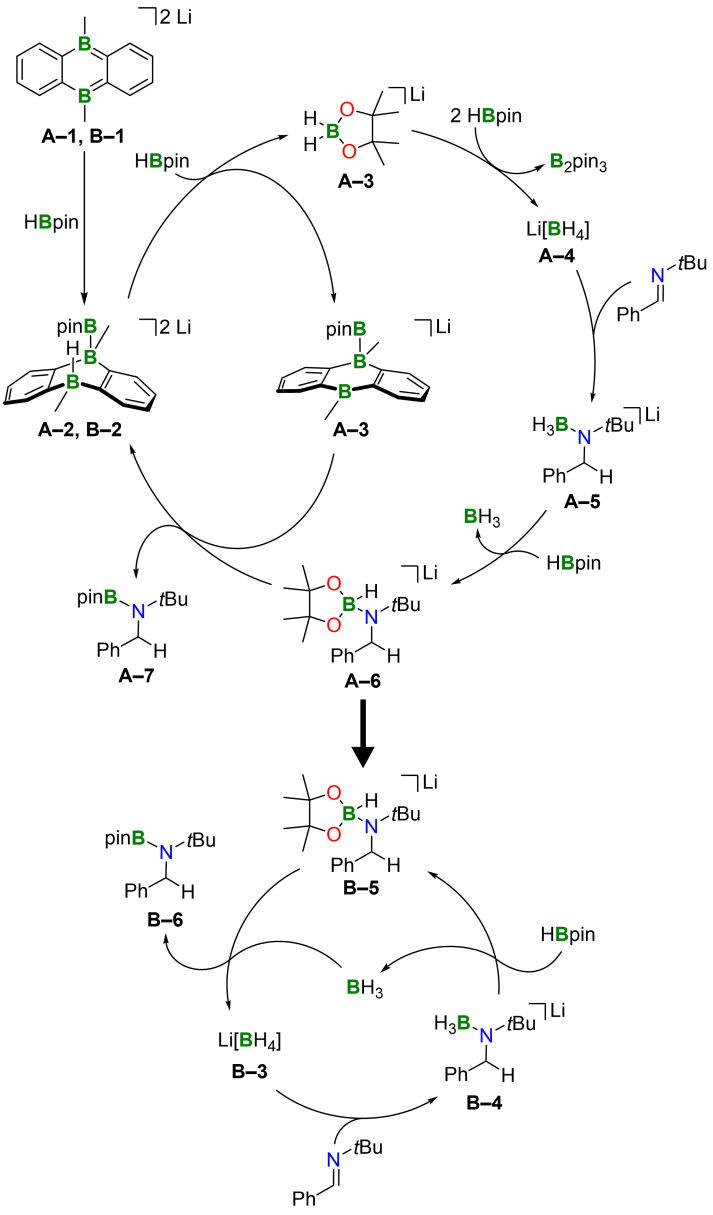

Figure 4.1: Catalytic Cycles A and B. Explicit solvent is omitted for clarity.

In chapter 3 the multifaceted behavior of a doubly reduced arylborane in B–H–bond activation and hydroboration catalysis was investigated in detail, both experimentally and theoretically. As we observed that the energetics of the theoretically modeled reactions depend significantly on the environment, we chose to investigate this effect further and benchmark the chosen electronic structure method with more

sophisticated approaches. The results of this investigation are presented within this chapter.
We focused on the reaction mechanism that encompasses the hidden BH_3 catalysis, as we were particularly interested in the changes in reaction profile prediction when the environment model is changed or simplified. By the model that is proposed in chapter 3, we predict that instead of the targeted diboraanthracene (DBA)–based hydroboration an undesired ("hidden") BH_3–based reaction takes place for one of the imine substrates. We argue that the latter is thermodynamically more favorable, because the key intermediates are lower in energy and the total reaction energy is more exergonic.

For the sake of simplicity, the notation of the intermediates from chapter 3 is changed to Cycle **A** and Cycle **B** (see Figure 4.1). The reaction mechanism is summarized in the following section, for additional details refer to our corresponding publication[69].

In a first step, the reduced DBA (**A–1**) activates the pinacol borane HBpin by splitting the H–B bond. The H and Bpin residues add across the central ring and intermediate **A–2** is formed. Further reaction with excess HBpin results in the reduction of HBpin by transfer of a hydride ion from **A–2**, yielding intermediates **A–3**. The original double negative charge of **A–2** is split and a singly charged DBA molecule with one Bpin residue at boron is produced (DBA–Bpin). Intermediate $[H_2Bpin]^-$ (**A–3**) is highly reactive and decomposes by reaction with HBpin to the fully reduced boron species $[BH_4]^-$ (**A–4**). **A–4** is able to reduce the substrate imine by formal *syn*–addition to the N=C double bond, yielding intermediate **A–5**. **A–5** reacts in a subsequent step with excess HBpin from solution. By nucleophilic attack of the formally negatively charged N atom on the B center in HBpin, the BH_3 residue is interchanged with an HBpin moiety (**A–6**). Finally, the activated HBpin moiety reacts with the DBA–Bpin molecule generated in step **A–3** which abstracts the hydride ion. This leads to the formation of the product **A–7** and the catalyst **A–2**. Because Cycle **A** generates one equivalent of the borane BH_3 per equivalent of product, another reaction cycle is possible (Cycle **B**). Instead of the reduction of HBpin after step **A–1** → **A–2** or equivalently **B–1** → **B–2**, the BH_3 that is present in the reaction mixture can abstract the hydride from **A–2** (**B–2**) to form intermediate **B–3** directly. The subsequent reaction of **B–3** is analogous to Cycle **A**, but in the final step the hydride is not transferred back to DBA–Bpin. Instead the free BH_3 intercepts the reaction and **B–3** is regenerated as the new catalyst. Because computed hydride affinities were larger for **B–3** in comparison to **A–2**, the

reaction preferably proceeds according to Cycle **B** after sufficient BH_3 is formed by a few iterations of Cycle **A**.

4.2 Computational Details

Incipient calculations were performed with the Gaussian 16 software[70]. To expand the scope of applicable methods and basis sets, the ORCA 5 program package [71, 72] was used as well. In Gaussian, implicit solvation effects were incorporated by the Solvation Model for Density (SMD) variant[73] of the Polarizable Continuum Model with integral equation formalism (IEFPCM)[74]. Because PCM is not available in ORCA, the Conductor–like PCM (CPCM)[75] was used instead, both in the standard and the SMD variant. In all cases THF ($\varepsilon = 7.43$) was used as solvent. As the implementation of the ωB97XD[76] functional in Gaussian differs from that in ORCA, the ORCA version is denoted as ωB97X-D3[77]. Unless otherwise stated, single point calculations were performed on the ωB97XD/6-31+G(d,p) equilibrium geometry which was confirmed by vibrational frequency analysis. As the reaction of interest takes place at 100°C, corrections to the Gibbs energy were calculated at 373.15 K unless indicated otherwise. Temperature dependent standard state and solvent concentration corrections to entropy were added according to the commonly known method by Ben–Naim[78]. For a comprehensive summary of all applied electronic structure methods and basis sets and their corresponding references refer to Table 4.1. All ORCA calculations include the RIJCOSX approximation [103] to save computational time. Matching auxiliary basis sets were used when available. To the best of our knowledge, no ma-def2 auxiliary basis sets have been defined yet. Therefore, for the ma-def2 basis sets the automatically generated auxiliary basis (AutoAux) as implemented in ORCA was used. For the ma-def2-QZVP basis specifically, self-consistent field (SCF) instabilities occured with the AutoAux basis set. Thus, it was replaced by the corresponding aug-cc-pVQZ auxiliary basis. As some auxiliary basis sets do not cover the Li atom, in these cases AutoAux was also used for Li to complete the auxiliary basis.

In principle, there are two possibilities to consider the influence of solvent effects on the properties of a chemical system. On one hand, explicit solvent molecules can be included in the calculation which makes it more expensive. On the other hand, continuum solvation models like PCM aim at modelling the solvation shell in a more economic way. If the structure of the solvation shell is ill defined or volatile and the computational model is attempting to describe it by inclusion of explicit solvent, it is necessary to sample many conformations to obtain information from the re-

Table 4.1: Methods and basis sets.

Methods	
Gaussian 16	ORCA 5
ωB97XD[76]	ωB97X-D3[77]
B3LYP-D3[79–81]	revDSD-PBEP86-D3BJ[82]
M06-2X[83]	DLPNO-CCSD(T)[84]
PBE0-D3[81, 85]	B97-3c[86]
SCS-MP2[87, 88]	
Basis sets	
6-31+G(d,p), 6-311++G(d,p)[89–92]	
cc-pVDZ, cc-pVTZ[93, 94]	
def2-SVP, def2-TZV, def2-TZVP, def2-TZVPP, def2-QVZP[95]	
aug-cc-pVDZ, aug-cc-pVTZ, aug-cc-pVQZ[94, 96]	
ma-def2-SVP, ma-def2-TZVP, ma-def2-QVZP[95, 97]	
Auxiliary basis sets	
def2/J[98]	
cc-pVDZ/C, cc-pVTZ/C[99, 100]	
def2-SVP/C, def2-TZVP/C, def2-QVZPP/C[101]	
aug-cc-pVDZ/C, aug-cc-pVTZ/C, aug-cc-pVQZ/C[99, 100]	
Automatic Generation of Auxiliary Basis Set (AutoAux)[102]	

sulting statistical ensemble. An example of this approach is the study by Tongraar and Rode[104], in which the solvation shell of Na^+ and K^+ in water was studied by means of ab initio QM:MM molecular dynamics simulations. Remarkably, the water molecules were not constrained to either the QM or the MM region, as a flexible transfer between both regions was implemented. In this way, no specific solvent molecules had to be choosen for the more accuratly described first solvation shell. As such sophisticated models are generally not feasible for large systems, continuum solvation modelling represents an attractive alternative. Albeit a cheap and in many cases sufficiently accurate approximation, there are limits to its applicability. It was shown that PCM-based models fail to replicate solvation energies obtained from experiments or calculations including explicit solvents for some systems.[105, 106]

To gauge the accuracy of our solvation model, we decided to benchmark it against available experimental data. In case of the DBA molecule and its derivatives, we compared the optimized geometry and the predicted coordination number in the first solvation shell to crystal structures. This approach can be rationalized by the follow-

ing experimental findings. Reduced and thus negatively charged DBA–type systems have been shown to form contact ion pairs with the corresponding counter ions in tetrahydrofuran (THF) solution, as demonstrated by ^{7}Li NMR spectroscopy[13]. The formation of contact ion pairs results in co–crystalization of solvent molecules in the solid phase, which represent a prominent feature in the crystal structures[14] of both Li_2DBA and Na_2DBA (see Figure 4.2). Based on these observations, we assume that the crystal structures provide reliable information on the coordination sphere in solution which we attempt to reproduce for the evaluation of reaction mechanisms. Preliminary calculations showed that a mixed approach of implicit and explicit solvation afforded the best agreement with X–ray data (see Figure 9.1). Therefore, all subsequent calculations included SMD as described in the Computational Details section, unless otherwise stated. For the calculation of solvation free energies, and consequently predictions of the coordination sphere, two types of thermodynamic cycles can be applied. Either the solvation consists of the reaction of the solute with isolated solvent molecules ($n \cdot (solvent)$) or the reaction of the solute with a solvent cluster ($(solvent)_n$). Bryantsev et al.[107] showed that for strongly interacting solvents like water, the latter approach yields more accurate results, as hydrogen bonds are described equally on both sides of the equation. As in our case THF is an aprotic solvent, we consider the first approach to be a viable route as dipole–dipole interactions between THF molecules are weak in comparison to the hydrogen bonds in water. Preliminary DFT calculations support this by revealing that the formation of THF clusters is an endergonic process, as the interaction between two THF molecules is not strong enough to out weight the entropy penalty.

4.3 Results and Discussion

4.3.1 Comparison of Model and Experiment

Figure 4.2 shows the stepwise solvation of Li_2DBA (Figure 4.2 a) and Na_2DBA (Figure 4.2 b) in THF. THF molecules were added symmetrically above and below the DBA plane. In both cases, the enthalpy of the system is lowered by the addition of solvent molecules, whereby for Li_2DBA the reaction enthalpy for the first step is larger (–39 kcal mol^{-1} vs. –31 kcal mol^{-1}), but declines more rapidly (–16 kcal mol^{-1} vs. –25 kcal mol^{-1} in the last step). From our experience, lowering the count of isolated species in a reaction by one results in a entropy penalty of about 10 kcal mol^{-1}, which is consistent with our findings for the entropy contributions in the solvation process. For Li_2DBA, the addition of two THF molecules to a complex containing four THF molecules is endergonic by 7.6 kcal mol^{-1}. This means

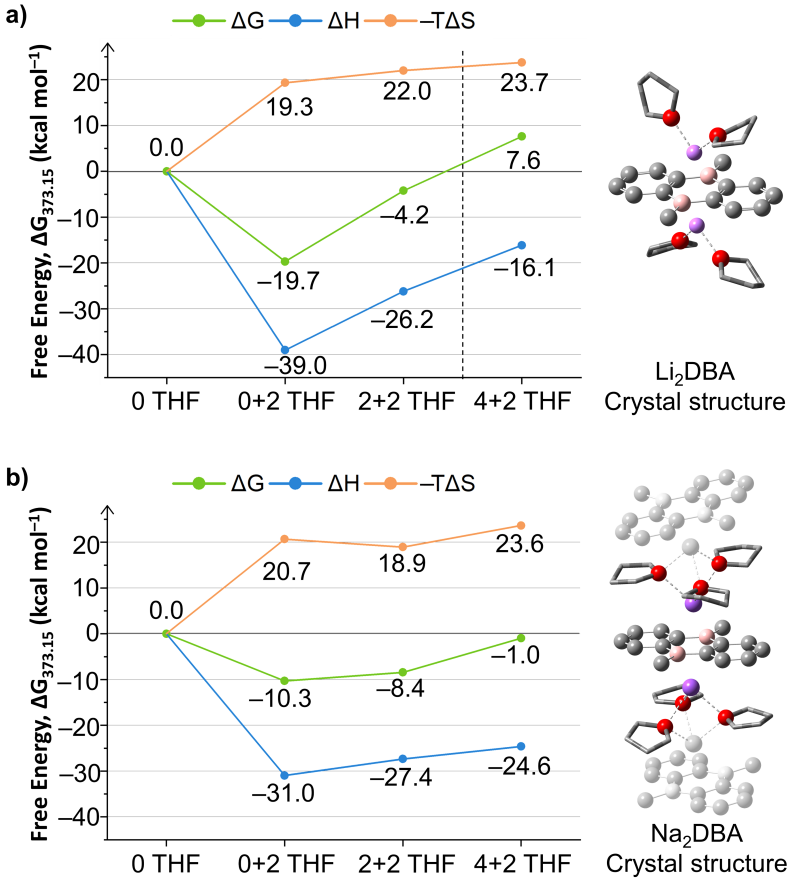

Figure 4.2: Prediction of coordination numbers. The depicted solvation energies are corresponding to stepwise solvation. The optimal coordination number is reached before the next solvent addition becomes endergonic. Hydrogen atoms are omitted for clarity.

that the global minimum is found at four THF molecules with a Gibbs free energy of –23.9 kcal mol^{-1} in comparison to the unsolvated contact ion pair. For Na_2DBA, the same step is still slightly exergonic by –1.0 kcal mol^{-1}, which means in this case we predict the coordination number to be six THF in total with a free energy difference of –19.7 kcal mol^{-1} in comparison to the unsolvated contact ion pair. In any case the limit for THF addition is six THF in total, as the complexes become sterically saturated and additional THF dissociate from the counterions. Both predicted coordination numbers can be observed in the corresponding crystal structures. Further inspection of key distances in the coordination sphere of the counter cations (see Table 9.1) show good agreement with X–ray data for Li^+, whereas Na^+ distances show slight deviations. This result can be rationalized by the unique crystallization pattern of Na_2DBA in the solid state. It forms chains of stacked DBA–counter ion contact pair units which share layers of three THF molecules in between them (see Figure 4.2 b). The comparison to experimental structural data confirmed our

approach of mixed implicit and explicit solvation. Therefore, the optimal coordination number for every species in the reaction that involves charged moieties was determined analogously (see ESI of our recent publication in chapter 3).

4.3.2 Influence of System Size and Entropy Corrections

After assessing the accuracy of the description of the first solvation shell, we were interested in the errors that are introduced by neglecting the explicit treatment of the environment. All charged intermediates that involve a coordination sphere including explicit THF molecules were reoptimized first without explicit solvent and in a subsequent step without the positively charged counterions. Gibbs free energies along both reaction paths were reevaluated for all obtained structures. The results are depicted in Figure 4.3.

We observe that the energetic order of the intermediates is strongly dependent on the treatment of the environment. When explicit THF are neglected, key intermediates are destabilized in comparison to the full system. Albeit in the first step of Cycle **A** (**A**–**1** → **A**–**2**) changes in free energy are small, in the subsequent steps there is a significant rise in energy for the neutral systems lacking explicit THF. This can be rationalized by the changes in the solvation shell that occur during the reaction. **A**–**1** resembles the structure that was found by X–ray spectroscopy, with two solvent molecules coordinated to the each of the Li^+ ions above and below the DBA plane. After addition of HBpin to DBA, the newly formed intermediate **A**–**2** also contains four THF molecules, with the corresponding Li^+ ions coordinated to the Bpin residue on one side of the DBA plane. Therefore, the total amount of solvent in the coordination sphere does not change, which causes only small changes in energy when it is neglected. On the contrary, intermediates **A**–**3**, **A**–**4**, **A**–**6** and the product **A**–**7** are destabilized by 5.9, 6.8, 16.0 and 13.4 kcal mol^{-1}, respectively. Analysis of the contributions to the free energy reveals that this effect is caused mainly by differences in electronic energy, whereas the entropy corrections have the opposite effect (see Table 9.2). The rise in electronic energy in comparison to the full system ranges from 1 to 30 kcal mol^{-1}, depending on the intermediate. Entropy contributions are lowered by up to 13 kcal mol^{-1} because association of solvent from solution to the newly formed intermediates and the corresponding entropy penalty is neglected. The same effect can be observed for Cycle **B**, however the changes in entropy are smaller and the destabilization of intermediates can be ascribed to changes in the electronic energy for the most part. An exception to this is the reaction step **B**–**3** → **B**–**4**, namely the reduction of the unsaturated starting material by formal *syn*–addition of BH_4^- to the double bond. In this case, the free energy is lower

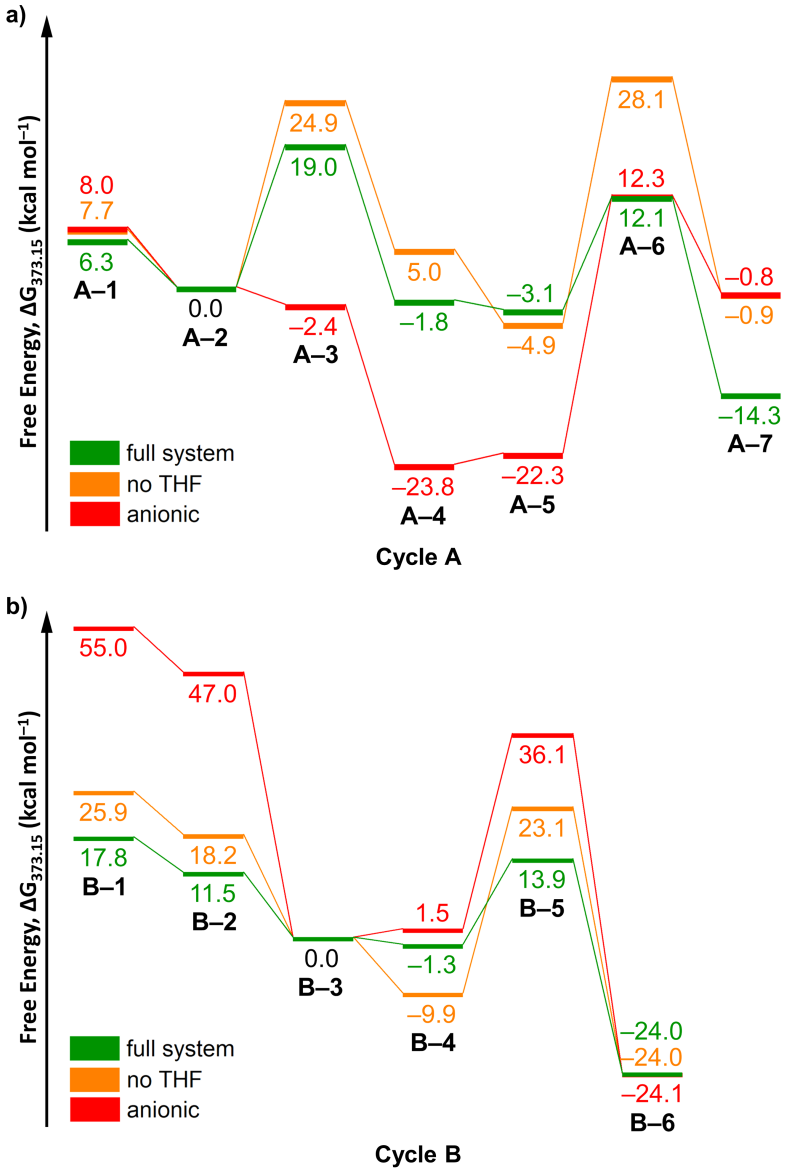

Figure 4.3: Dependence of the reaction profile on system size. The calculation including both explicit solvent and counterions is denoted with "full system". Accordingly, calculations without explicit solvent, but including the counterions are denoted with "no THF". Calculations on the anionic structures without environment are denoted "anionic".

in comparison to the full system. The reason for this deviation is the interaction of the negative charge in the intermediate with the corresponding Li^+ counterion. In **B–3**, the negative charge is formally distributed over four partially negatively charged hydrogen atoms in the BH_4^- moiety. This means, there is a weak electrostatic interaction with the cation, which is mostly stabilized by solvent molecules. After addition to the double bond, the negative charge is concentrated around the electronegative N atom. Consequently, the interaction with the coordinated cation

is stronger. In the full system where THF molecules are present, the stabilization of the cation is not as dependent on the negatively charged solute because of the coordination of explicit solvent. If the solvent is not treated explicitly, the difference in interaction between the negatively charged solute and the positively charged counterion is more important. Therefore, we observe the reaction step to be more exergonic for **B–4** where there is a strong N–Li^+ interaction. The analogous step in Cycle **A** (**A–5**) is subject to the same effect. Because for Cycle **A** the product is destabilized in comparison to the full system, the global minimum of the reaction shifts to **A–5**. In this case, the calculations fail to reproduce the experimentally found formation of the product **A–7**.

Aside from the entropy penalty that association of THF from solution brings about and the influence on cation stabilization, there is another solvation effect present in both reaction cycles. Cycle **A** produces free BH_3 in step **A–5** → **A–6**. We assume that in THF solution the Lewis acid-base complex BH_3·THF is formed and include this complex in our description of the full system. When explicit THF is neglected, consequently, each step which involves the BH_3 molecule is destabilized. In the reaction without explicit solvent, the free energy of intermediates **A–6** and **B–5** is raised by 33 kcal mol^{-1} when referenced to the previous step. In contrast, when THF is treated explicitly, the free energy difference is only 15 kcal mol^{-1} in comparison to the previous step. As the product of Cycle **A** (**A–7**) includes free BH_3 and the product of Cycle **B** (**B–6**) does not, we see the identical destabilization of **A–7** both when explicit THF and further the cations are neglected, but it does not occur for **B–6**. There is no change in the energy of the product **A–7** when further neglecting the cations, because the products of the reaction, namely the hydroborated substrate and BH_3, are neutral. The net free energy of Cycle **B** (**B–6**) is independent of explicit solvation and inclusion of counterions, because the product is neutral and there is no BH_3 formation.

When both explicit solvent and counterions are neglected, the energetic landscape of the reaction changes drastically. Most notably, intermediates **A–3** to **A–5** are stabilized with respect to the reactants (see Figure 4.3 a). Similarly, intermediates **B–1** and **B–2** are destabilized with respect to the reactants (see Figure 4.3 b). The relative free energy of the reaction step **1** → **2** in both cycles however is weakly affected by decreasing the size of the model. The reason for this is the anionic nature of the corresponding DBA intermediates. Whereas the intermediates **A–1**, **A–2**, **B–1** and **B–2** contain di–anionic DBA moieties, the negative charge is split in the subsequent reaction steps. In step **A–2** → **A–3** (analogously in step **B–2** → **B–3**), one negative charge remains at the DBA site and the second electron

is transferred concurrently with the activated hydride to a HBpin molecule from solution (for Cycle **B** the hydride is transferred directly to a BH_3 molecule that was generated in the previous reaction cycle). As the two negative charges are separated in the course of the reaction, the repulsive Coulomb interaction between them is avoided. Hence, without explicit counterion treatment, mono–anionic species are artificially stabilized in the calculation compared to their di–anionic counterparts. In Cycle **A** this leads to a wrong prediction of the reaction product (**A**–**4**) with a free energy difference of –23 kcal mol^{-1} in comparison to the experimentally found product **A**–**7**.

Because Cycle **B** runs independently of the di–anionic DBA site, as it is a hidden BH_3 catalysis, the error of neglecting counterions and solvent is partly migitated. The exception is intermediate **B**–**5**, which includes the uncoordinated BH_3 molecule and the poorly stabilized negative charge in the $[HBpin{\cdot}NR_2]^-$ complex. Although the anionic calculation yields the correct net free energy, the previous intermediate lies 36 kcal mol^{-1} above the reactants, which would inhibit the formation of the product. Thus, the reaction becomes trapped at step **B**–**3** and we again can not reproduce the results of the experiment.

In summary, reduction of the system size from the full system, i.e. explicit treatment of counterions and first solvation shell, to an unsolvated neutral as well as an unsolvated anionic system introduces large errors in the energetic sequence of the intermediates. By neglecting solvation effects, key intermediates are destabilized, whereas calculations based on anionic species yield considerably distorted free energy differences between di–anionic and mono–anionic systems. These errors have a large impact on the predictive power of the model and make it impossible to explain experimentally observed results.

As described in the Computational Details section, temperature dependent entropy corrections were added to the free energies of each species in the reaction. After we found the system size, i.e. the treatment of the environment of anionic species, is an important part of our model, we investigated the influence of said corrections on the results. Figure 4.4 shows the dependence of the reaction profile of Cycle **A** (Figure 4.4 a) and Cycle **B** (Figure 4.4 b) on the addition of entropy corrections. First, we calculated the thermochemistry according to the standard protocol as implemented in most quantum chemistry software. The molecules were treated as an ideal gas at standard conditions (a temperature of 298.15 K and a pressure of 1 atm). In a second step we accounted for the different standard state in solution at the same temperature. To each species the correction term $\Delta G^{0\rightarrow\star}(298.15\ \mathrm{K}) = 1.89$ kcal mol^{-1} was added which corresponds to a concentra-

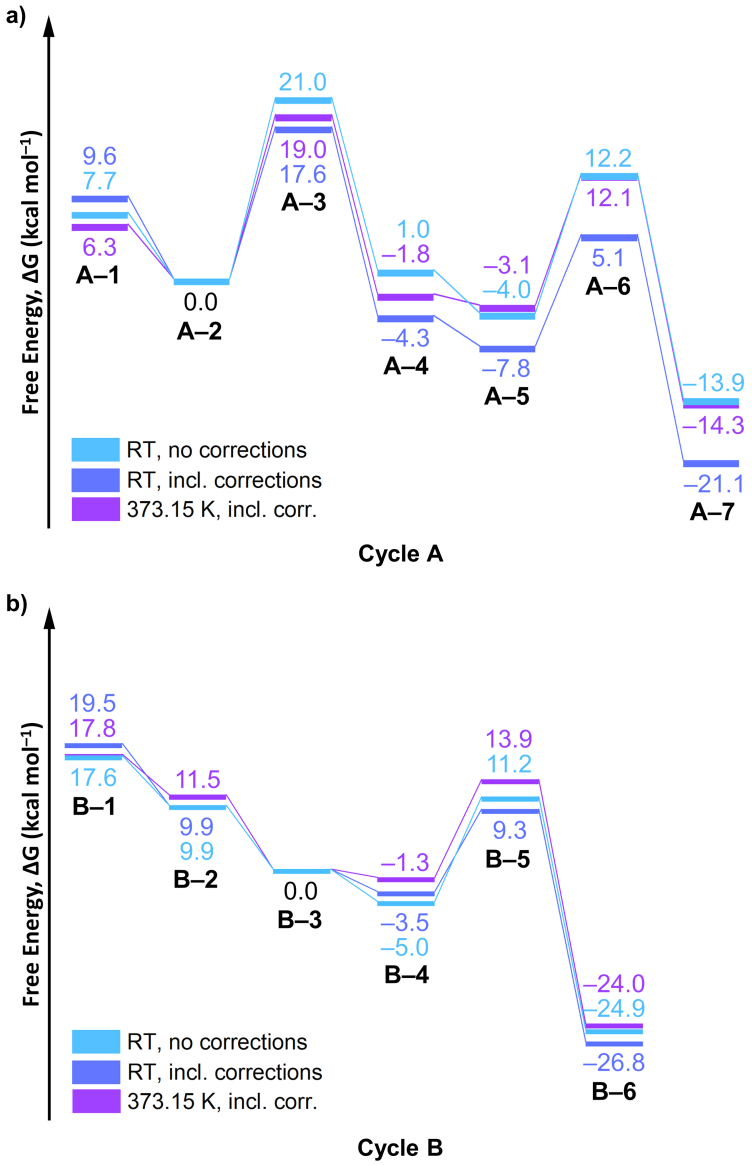

Figure 4.4: Dependence of the reaction profile on entropy corrections. The result of standard calculations as implemented in most quantum chemistry software is denoted "RT, no corrections". When additional standard state and concentration correction are included, results are denoted "RT, incl. corrections". When all corrections are calculated at the experimental temperature, the results are denoted "373.15 K, incl. corr.".

tion of 1 mol l^{-1}. As in the course of the reaction solvent molecules play a role, an additional correction $\Delta G^{\text{conc}}(298.15\ \text{K}) = 1.49$ kcal mol^{-1} was added to the isolated THF molecules. With this we correct for the much higher concentration than 1 mol l^{-1} of the solvent in the condensed phase. Finally, as the experimental reaction takes place at 373.15 K, we recalculated the thermochemistry for this temperature. The new correction terms were calculated to be $\Delta G^{0\rightarrow\star}(373.15\ \text{K}) = 2.54$ kcal mol^{-1}

and $\Delta G^{\text{conc}}(373.15\ \text{K}) = 1.78$ kcal mol^{-1}.

Generally, inclusion of the standard state and concentration corrections results in a stabilization of the intermediates with respect to the reactants (see Figure 4.4). In Cycle **A**, key intermediates **A–3** and **A–6** are lowered by 3 kcal mol^{-1} and 7 kcal mol^{-1}, respectively. The free energy of product **A–7** also drops by 7 kcal mol^{-1} in comparison to the uncorrected value. In Cycle **B**, intermediate free energies are mostly stabilized as well, but the effect is smaller than for Cycle **A**. As Cycle **B** runs independently of the dianionic DBA species, the changes in the solvation shell are less prominent and entropy corrections become less important. Interestingly, when thermochemistry is calculated at the same elevated temperature as the experimental conditions demand, the stabilizing effect of the correction terms at room temperature is cancelled out. While the free energy of **A–1**, **A–3**, and **A–4** is still lower in comparison to the uncorrected values, the rest of the reaction profile shows only small deviations from the reaction profile at room temperature without corrections. For Cycle **B**, again entropy plays a less important role and the changes in free energy are generally negligible.

4.3.3 Benchmark of Electronic Structure Methods

Additionally to bench–marking the influence of environment treatment and entropy corrections, we also investigated different electronic structure methods to check their applicability on the di–anionic system. As coupled cluster theory with single, double and perturbative triple excitations (CCSD(T)) is commonly known as the gold–standard in main group quantum chemistry, we aimed at obtaining energies at a comparable level of theory as a benchmark reference. Because the investigated intermediates become quite large when solvent is considered explicitly, even with the use of the domain-based local pair natural orbital (DLPNO) approximation, CC single point calculations with a sufficiently large basis set were not feasible given the available resources. Therefore, we chose to treat the system by means of a multiscale calculation approach. In the framework of a subtractive QM:QM ONIOM[61, 108] scheme, the ionic intermediate structures were split into a low–layer consisting of the explicit solvation shell and a high–layer consisting of the solute, i.e. the ion pair with a neutral net charge. Consequently, isolated THF molecules were treated at the low–layer level of theory whereas all neutral intermediates without ionic moieties were treated at the high–layer level of theory. In this way, the calculated energies are consistent throughout the entire reaction, irrespective of solvent rearrangement. In most standard applications of the ONIOM scheme the high– and the low–layer are structurally not separated. This leads to dangling bonds and e.g. the need of link

atoms in between the layers, which in turn necessitates a careful consideration of meaningful layer boundaries. In our case, there is a distinct separation between the solute and the solvation shell in terms of covalent bonding, effectively eliminating this issue. As a benchmark reference, we chose the DLPNO-CCSD(T)/ma-def2-QZVP:ωB97X-D3/ma-def2-TZVP level of theory. In this scheme, interaction between the solute and the solvent is treated at the DFT level because we assume the electronic structure of the solvent is well described by the cheaper ωB97X-D3/ma-def2-TZVP method. The anionic core and the counterions of the intermediates are treated by the sophisticated CC approach with a large basis set because the bulk of the electron density is centered here. Thus, correlation effects will have a stronger influence than in the solvation shell. The high–layer is polarized by the low–layer by means of electrostatic embedding. We deem this approach fitting as in the real system the interaction between the solvent and the solute is mainly electrostatic in nature as well. As we investigate gas phase calculations as well as implicit solvation with (C)PCM, both corresponding QM:QM references were also calculated either in the gas phase or including implicit solvent. Because an error occurs when the SMD variant of CPCM is requested together with a multiscale calculation in the ORCA 5.0.4 code, the reference calculation was performed with the standard CPCM instead. The developers are already aware of this issue.

To compare the accuracy of the investigated electronic structure methods we calculated single point energies on the ωB97XD/6-31+G(d,p) equilibrium geometries and evaluated the electronic energy differences along the reaction path. The root mean square deviations (RMSD) with respect to the aforementioned reference calculation are shown in Figure 4.5 (for relative free energies see tables Table 9.3 to Table 9.9). Deviations of Cycle **A** and Cycle **B** were calculated separately because they describe two distinct reactions and have a different reference point, i.e. starting point, in the catalytic cycle. Figure 4.5 a) represents the RMSD changes for a variety of methods and basis sets. For Cycle **A**, the DFT methods ωB97XD, M06-2X and PBE0-D3 have a comparable deviation of about 5 kcal mol^{-1} when used with the 6-311++G(d,p) basis set. B3LYP-D3 is an outlier with a deviation of 2.9 kcal mol^{-1} which suggests that it matches the reference best in this case. However, the deviation for Cycle **B** is considerably larger (about 5 kcal mol^{-1}). Contrarily, for the other functionals the deviation is generally smaller for Cycle **B** than for Cycle **A**. The lowest deviation of 1.6 kcal mol^{-1} can be attributed to the M06-2X method. As the quality of the description of the reaction path should not vary arbitrarily from one reaction to the other, an equal deviation from the reference value is desirable in favour of error compensation. In this respect, the ωB97XD functional

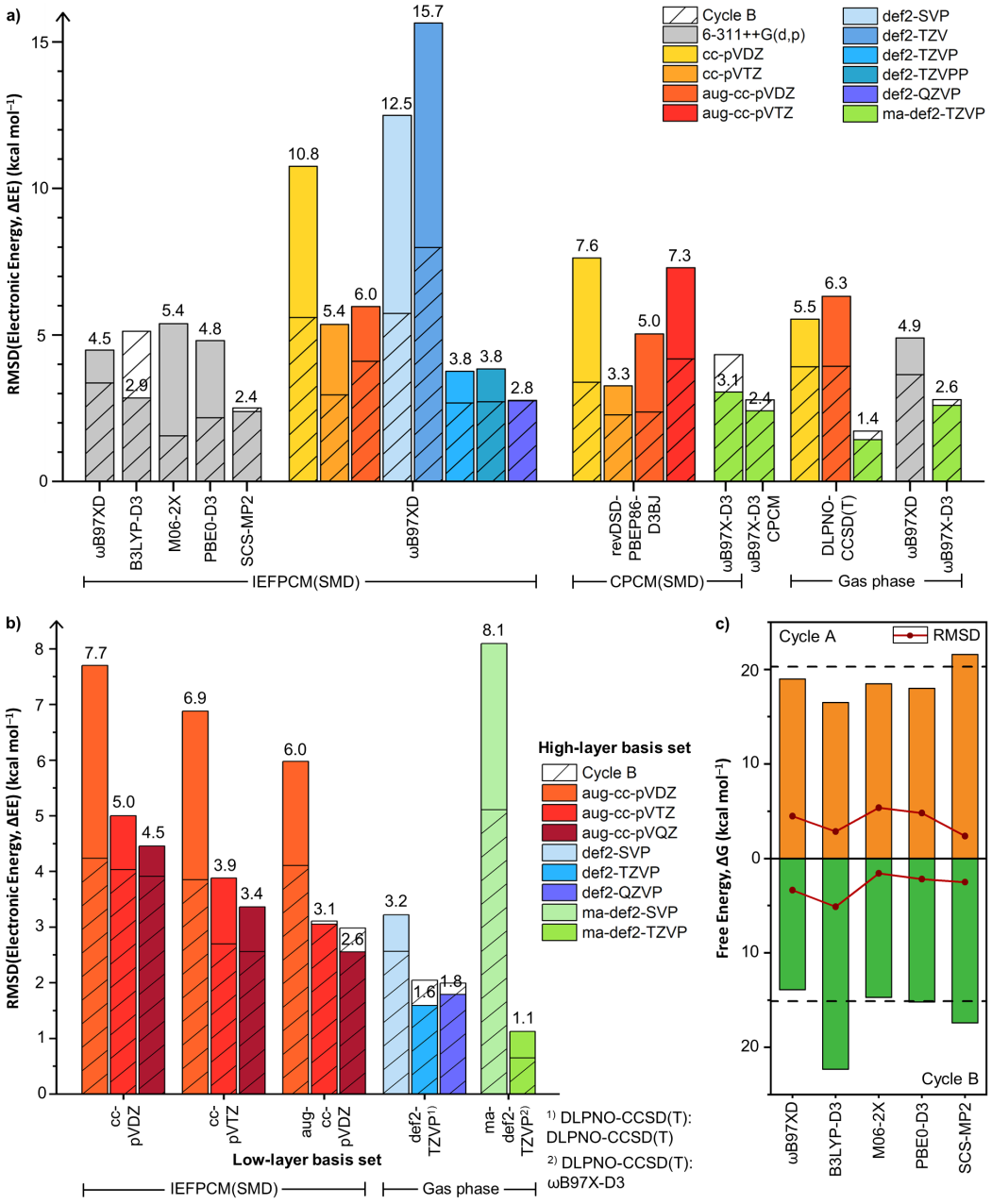

Figure 4.5: Benchmark of Electronic Structure Methods. RMSDs are calculated with respect to the DLPNO-CCSD(T)/ma-def2-QZVP:ωB97X-D3/ma-def2-TZVP level of theory. The reference includes CPCM for comparison with results with implicit solvation, otherwise the reference was calculated in gas phase. a) Comparison of different methods and basis sets applied to the full system. b) Comparison of different QM:QM schemes. The energies were calculated with the ωB97XD functional, unless otherwise denoted. c) Comparison of free energies from single point calculations with different methods and the 6-311++G(d,p) basis set. Free energies of intermediate **A**–**3** are shown in orange. Free energies of intermediate **B**–**5** are shown in green. The dashed line represents the reference value for both intermediates.

shows a more consistent behaviour with a deviation of 4.5 kcal mol^{-1} for Cycle **A** and 3.4 kcal mol^{-1} for Cycle **B**. The best results with the 6-311++G(d,p) basis are achieved with the SCS-MP2 method as implemented in Gaussian. The consistent error for both cycles is 2.4 and 2.5 kcal mol^{-1}, respectively.

The peculiar distribution of RMSD values among the DFT methods necessitates a more in–depth examination of their influence on the reaction path. To compare the prediction of the reaction course, corrections to the Gibbs energy from the optimization level of theory were added to the electronic energies obtained by single point calculations with the various methods. Figure 4.5 c) shows the least stable intermediates for both reaction cycles as a function of the electronic structure method. Because the least stable intermediate is closely tied to the rate determining step of the reaction, we base our prediction of the switch from Cycle **A** to Cycle **B** on the energy difference between the highest lying intermediates in both cycles, namely **A**–**3** and **B**–**5**. The ωB97XD functional underestimates both energies to approximately the same degree, which is reflected in the similar RMSD values throughout both Cycle **A** and B. Likewise, the SCS-MP2 method overestimates both energies but has the lower RMSD with respect to the complete reaction path in comparison. Interestingly, B3LYP-D3 underestimates the energy of the least stable intermediate in A (**A**–**3**) while also overestimating the least stable intermediate in B (**B**–**5**). As a result, Cycle **B** becomes unfavourable in comparison to A and we would not predict the experimentally observed switch to a hidden BH_3 catalysis. Both the M06-2X and the PBE0-D3 functionals yield energies close to the reference for Cycle **B**, but underestimate **A**–**3**. The inaccuracy in A results in the higher overall RMSD for A in both methods. Nevertheless, we still predict a switch to Cycle **B** as **A**–**3** is higher in energy than **B**–**5** in both cases.

Because the Pople–type basis sets do not approach the complete basis set limit systematically, we also tested the basis set error of both the Dunning and the Ahlrichs basis set family with the ωB97XD functional. Again, for Cycle **B** all errors are smaller than for Cycle **A**. High errors of about 10 kcal mol^{-1} occur with the double zeta and split valence quality basis sets, namely cc-pVDZ and def2-SVP. If the cc-pVDZ basis set is augmented with diffuse functions (aug-cc-pVDZ), the results closely resemble the calculations with the larger cc-pVTZ basis. Calculations with the aug-cc-pVTZ basis did not converge for the largest intermediates of the reaction, hence, they are not included in this analysis. The highest error is observed if polarization functions are omitted. The def2-TZV basis shows a deviation of 15.7 kcal mol^{-1} to the benchmark reference. This error is drastically reduced to 3.8 kcal mol^{-1} by including polarization functions with the def2-TZVP basis set.

Further augmentation of the def2-TZVPP basis has no influence on the electronic energy and gives nearly identical results to the def2-TZVP basis. In comparison to the triple zeta quality Pople–type basis 6-311++G(d,p), the def2-TZVP results are closer to the reference with a respective RMSD of 4.5 and 3.8 kcal mol^{-1}. The best match is achieved with the large def2-QZVP basis set, for which the RMSD for both reaction cycles converges to 2.8 kcal mol^{-1}.

Double hybrid (DH) DFT has gained popularity in the last decade as it promises to combine the accuracy of *ab initio* methods with the affordability of DFT.[109] Therefore, we decided to test a revised version of the DSD-PBEP86 DH functional with additional dispersion correction (Grimme's dispersion correction version 3 with Becke–Johnson damping). In comparison to the hybrid functional ωB97XD, the DH performs slightly better for the Dunning basis sets. The RMSD is reduced by 3.2, 2.1 and 1.0 kcal mol^{-1} for the cc-pVDZ, cc-pVTZ and aug-cc-pVDZ basis sets, respectively. The resolution of identity (RI) approximation as implemented in ORCA facilitated the use of the large aug-cc-pVTZ basis set which could not be employed otherwise with the Gaussian software package. Interestingly, the RMSD increases with the augmentation of the cc-pVTZ basis from the lowest DH value of 3.3 kcal mol^{-1} to the second highest value of 7.3 kcal mol^{-1}, a value that is close to the cc-pVDZ result. This unexpected deterioration of accuracy despite the large basis set hints at incomplete convergence with respect to basis set size. As a larger basis set could not be afforded with this method, it was not possible to fully clarify this observation.

When the ωB97XD/6-311++G(d,p) level of theory is compared to the ωB97X-D3/ma-def2-TZVP level in the gas phase, the latter yields a more accurate result. The RMSD is reduced from 4.9 to 2.6 kcal mol^{-1}. Moreover, the deviation is more consistent at the ωB97X-D3/ma-def2-TZVP level, as the RMSD is about the same for both Cycle **A** and Cycle **B**. When CPCM is included in the calculation, a similar effect is observed. The SMD variant causes a slight increase of the RMSD which can be rationalized with the reference method. As we were forced to use a standard CPCM calculation as a reference, all standard CPCM results are closer to the reference values then the CPCM(SMD) results. The effect of the SMD variant, i.e. the increase of the RMSD of 0.7 kcal mol^{-1} for Cycle **A**, is within the boundaries of chemical accuracy. For gas phase DLPNO-CCSD(T) calculations, the largest applicable basis set from the Dunning family is the aug-cc-pVDZ basis set. Unlike the previously discussed methods, augmentation of the double zeta quality cc-pVDZ basis with diffuse functions increases the RMSD for the DLPNO-CCSD(T) approach by 0.8 kcal mol^{-1}. Again, we interpret the worsening of the result with a not yet

converged calculation with respect to basis set size. Indeed, when the ma-def2-TZVP basis is employed, the RMSD drops to 1.4 kcal mol^{-1}, which is the lowest non multiscale value in this benchmark.

As with ωB97XD the largest applicable basis set is the aug-cc-pVDZ basis, we explored the aforementioned ONIOM QM:QM scheme to remedy this problem. The goal was to push the calculations as far to the complete basis set limit as possible. The results are depicted in Figure 4.5 b). By use of the multiscale ansatz, we achieved the treatment of the intermediates with an anionic core and their counterions with the sizeable aug-cc-pVQZ basis set. For all low–layer basis sets, increasing the size of the high–layer basis from aug-cc-pVDZ to aug-cc-pVTZ and finally aug-cc-pVQZ, causes the RMSD to decrease systematically by 3 and 0.5 kcal mol^{-1}, respectively. This shows good convergence of the high–layer electronic energy at the aug-cc-pVQZ level. In the low–layer, we observe augmentation of the cc-pVDZ basis set with diffuse functions to be more important than the addition of more ζ functions in the cc-pVTZ basis. Furthermore, the difference between the RMSD for Cycle **A** and Cycle **B** generally decreases with larger basis sets in the high– as well as the low–layer. It becomes negligible for the ωB97XD/aug-cc-pVTZ:ωB97XD/aug-cc-pVDZ level of theory. The benefit of the QM:QM scheme is apparent if the ωB97XD/aug-cc-pVDZ:ωB97XD/aug-cc-pVDZ result is compared to the ωB97XD/aug-cc-pVTZ:ωB97XD/aug-cc-pVDZ value. The former corresponds to the treatment of the whole system at the ωB97XD/aug-cc-pVDZ level of theory without the multiscale ansatz, whereas the latter is a refined calculation with a larger basis at the core of the ionic intermediates. By use of the QM:QM scheme, the RMSD is effectively halved. When both methods in the QM:QM scheme are changed from DFT to DLPNO-CCSD(T), augmented basis sets become much less affordable. Nevertheless, we managed to calculate the high–layer energy with the def2-QZVP basis in combination with the def-TZVP basis for the low–layer with an RMSD of 1.8 kcal mol^{-1}. As the previous analysis shows, augmentation with diffuse functions is important for the description of the anionic intermediates. Consequently, we decided to find a middle ground between the accuracy of CC methods and the affordability of DFT, favoring large diffuse basis sets to minimize basis set errors. In the gas phase, treatment of both the high– and the low–layer with the ma-def2-TZVP basis set while applying a DLPNO-CCSD(T):ωB97X-D3 ansatz results in the smallest deviation from the reference value (1.1 kcal mol^{-1}). Hence, we assume if the high–layer is calculated with the larger ma-def2-QZVP basis, the energy is sufficiently converged in terms of basis set size.
Considering these results, we chose the DLPNO-CCSD(T)/ma-def2-QZVP:ωB97X-

D3/ma-def2-TZVP level of theory as a benchmark reference. It combines the largest affordable basis sets with the accuracy of the DLPNO-CCSD(T) method for the electron-rich ionic intermediates and the cost efficiency of DFT for solute-solvent interactions.

4.3.4 Benchmark of ONIOM Scheme for Optimizations

Table 4.2: Optimization using the ONIOM scheme. "Full DFT" denotes calculations based on the geometries obtained on the ωB97X-D3/def2-SVP level of theory. "Anionic QM" and "Neutral QM" describe optimizations in which the counterions where treated at the low–layer and the high–layer level, respectively. All values are given in kcal mol^{-1}.

ΔG(EE)	**Full DFT**		**Full B97-3c**		**Anionic QM: B97-3c**		**Neutral QM: B97-3c**	
A–1	–0.2	(15.6)	1.3	(15.4)	–0.7	(15.2)	0.1	(14.9)
A–2	0.0	(0.0)	0.0	(0.0)	0.0	(0.0)	0.0	(0.0)
A–3	21.3	(8.9)	26.1	(11.4)	20.0	(7.1)	22.1	(8.8)
A–4	7.6	(–16.2)	7.9	(–19.0)	11.7	(–18.1)	13.2	(–16.4)
A–5	–1.9	(–32.0)	-2.7	(–34.8)	1.5	(–33.9)	3.0	(–32.3)
A–6	14.9	(–30.7)	16.0	(–33.5)	20.2	(–32.3)	21.8	(–30.7)
A–7	–9.2	(–55.6)	-8.7	(–55.7)	–4.1	(–55.5)	-3.8	(–55.5)
RMSD	**0.0**	**(0.0)**	**2.0**	**(2.1)**	**3.5**	**(1.4)**	**4.4**	**(0.3)**
B–1	7.0	(18.9)	9.2	(21.5)	7.7	(20.6)	6.9	(18.5)
B–2	7.2	(3.3)	7.9	(6.1)	8.3	(5.4)	6.8	(3.6)
B–3	0.0	(0.0)	0.0	(0.0)	0.0	(0.0)	0.0	(0.0)
B–4	–9.5	(–15.8)	–10.6	(–15.8)	–10.2	(–15.7)	–10.3	(–15.9)
B–5	7.3	(–14.5)	8.2	(–14.5)	8.5	(–14.2)	8.6	(-14.4)
B–6	–24.0	(–42.7)	–24.5	(–42.8)	–24.1	(–42.7)	–23.8	(–42.7)
RMSD	**0.0**	**(0.0)**	**1.1**	**(1.6)**	**0.8**	**(1.1)**	**0.7**	**(0.2)**

While the ONIOM scheme allows for the use of high level electronic structure methods in the ionic core of the molecules, its more traditional asset is the cost reduction of geometry optimizations. To gauge the speed up of a multiscale calculation, all intermediates were optimized at the B3LYP-D3/6-31+G(d,p) level of theory in gas phase as a initial guess structure. Subsequently, all structures were reoptimized at the ωB97X-D3/def2-SVP and the semi–empirical B97-3c levels of theory also in gas phase, as well as two distinct QM:QM approaches consisting of both methods (for details see Table 9.10). In the first QM:QM approach, the counterions were assigned to the low–layer. In the second QM:QM approach, the counterions were assigned to the high–layer. As a consequence, in the first calculation the high–layer becomes anionic, whereas in the second calculation it is neutral. In comparison to a full DFT calculation, the QM:QM ansatz performs best in terms of computational

time when a high number of solvent molecules are present in the first solvation shell. When intermediates with e.g. four THF molecules surrounding the solute are treated with the ONIOM scheme, the number of atoms that are treated with DFT is reduced considerably (from 84 to 32 atoms for **A**–**1** and from 106 to 54 for **A**–**2**). As a result, wall times for optimizations of these intermediates are about halved. For intermediates with fewer solvent molecules the ONIOM calculations become more costly then pure DFT in some cases and the net time savings are small. On average, the use of the semi–empirical B97-3c method for optimization reduces the wall time by 60 percent in comparison to a DFT calculation. When the geometrical RMSD of the B97-3c structures is compared to the full DFT geometries, it averages around 0.24 Å. The average RMSD for the anionic and the neutral high–layer geometries is 0.84 and 0.87 Å, respectively. However, after performing single point calculations on the ωB97X-D3/def2-TZVP level on all individual geometries and reevaluation of the relative energies along the reaction path, the trend appears to be reversed (see Table 4.2). For both reaction cycles, the RMSD of the electronic energy is reduced the more atoms are treated with DFT. For the B97-3c geometries, the energetic RMSD is 2.1 kcal mol^{-1} for Cycle **A** and 1.6 kcal mol^{-1} for Cycle **B**. The anionic QM:B97-3c geometries yield a RMSD of 1.4 and 1.1 kcal mol^{-1}, respectively. The smallest RMSD with 0.3 and 0.2 kcal mol^{-1} is obtained with the geometries that were optimized with the neutral QM:B97-3c scheme. When thermochemistry corrections from the optimization level of theory are added, we observe error cancellation in Cycle **A**. In terms of free energy, the B97-3c geometries yield the lowest RMSD of 2.0 kcal mol^{-1} whereas the highest RMSD is attributed to the geometries with a neutral high-layer (4.4 kcal mol^{-1}). For Cycle **B**, there is still an improvement of RMSD when thermochemistry is considered. On one hand, B97-3c gives overall good free energy values, but the key intermediate **A**–**3** is about 5 kcal mol^{-1} too high in energy. On the other hand, the neutral QM:B97-3c approach yields free energies that are generally too high in comparison to a DFT calculation, albeit the electronic energies are in good agreement. Similarly to the influence of different electronic structure methods, the changes in Cycle **B** are small by comparison to Cycle **A**. As a recommendation, semi–empirical methods like B97-3c are useful for the preliminary exploration of the potential energy surface of a reaction including solvent molecules. When molecules are encountered that demand a more sophisticated level of theory, but extensive explicit solvation is also desired, the ONIOM scheme represents a good middle ground between short wall times and accuracy. When free energies are of interest, geometries obtained in this way should be considered an appropriate guess for a higher level optimization and subsequent frequency calculation

with more consistent thermochemistry results.

4.4 Conclusions

In summary, the computational environment model is rationalized by comparison to experimental data, i.e. X–ray structure analysis. Coordination numbers are predicted correctly for the charged DBA species resembling alkali metal complexes. The dependency of the reaction path on the environment is confirmed by calculations of increasing complexity and system size. The most simple model involving anionic intermediates yields significantly different results from the fully modeled environment and does not predict the formation of the experimentally observed product. Because the inherent double negative charge of the DBA molecule is poorly handled by simple calculations, doubly charged intermediates are nonphysically destabilized with respect to singly charged intermediates. Similarly, the model of intermediate size that omits the explicit solvent molecules, in this case THF, results in the wrong description of the system. Key intermediates are destabilized in comparison to the full model. The increase in energy renders the entire reaction path unlikely. Furthermore, the wrong product is predicted. The full model including counterions and explicit solvent molecules yields an accurate description of the system, in which the correct product is found and key intermediates are stabilized in comparison to the simpler models. Furthermore, the effect of entropy corrections was investigated. For Cycle **A**, the changes in the coordination sphere along the reaction are more prominent which results in more influence of entropy effects in comparison to Cycle **B**. The same is true if the reaction path is evaluated at different temperatures. In the benchmark of electronic structure methods, the ONIOM scheme proves especially useful to achieve basis set convergence in combination with correlated methods in the important negatively charged parts of the intermediates. The first solvation shell is described sufficiently by a cheaper DFT method. Interestingly, the popular B3LYP-D3 functional does not predict the hidden BH_3 catalysis as a key intermediate in Cycle **B** is considerably destabilized with respect to the reference value. Finally, the applicability of the ONIOM approximation for geometry optimization is investigated. While the semi–empirical method B97-3c yields good geometries on its own, the results can be refined by treating central parts of the molecules by a DFT method.

5 Delayed Luminescence Phenomena in Arlyboronic Esters

5.1 Introduction

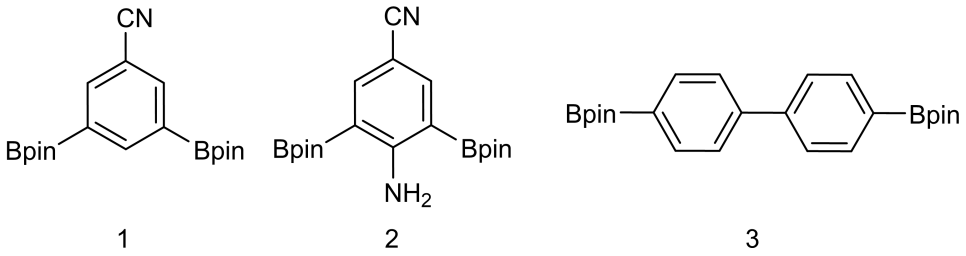

Figure 5.1: Lewis structures of the investigated compounds.

In 2017, Shoji *et al.* reported long–lived room temperature phosphorescence (RTP) in a series of heavy atom free molecules.[28] More specifically, 20 examples of simple arylboronic esters were shown to exhibit RTP in the crystalline state. Because the unusual phenomenon sparked interest in the group of Prof. Todd Marder at the University of Würzburg, the author of this work was employed to synthesize as many of the arlyboronic esters as possible in the context of an internship. Under supervision by the former PhD candidate Zhu Wu, different target molecules were synthesized and characterized spectroscopically. To our surprise, the long–lived luminescence phenomenon was not reproduced for the majority of the compounds. This prompted a thorough theoretical investigation of the remaining molecules that exhibited long–lived emission (see Figure 5.1). The results of the computational investigation are presented within this work.

Originally, compound **1** showed an emission with a half life of a few milliseconds which is why we focused on this molecule in our computations. After a few preliminary calculations which yielded no explanation for the phenomenon, Zhu Wu managed to identify an impurity in **1**: Compound **2**. Purified **1** does not show RTP any more. **2** initially exhibited delayed luminescence on its own. Therefore, the investigation proceeded by the comparison of **1** and **2**, as both molecules are very similar. While significant differences in the electronic structure were found (*vide infra*), there still was no explanation for the luminescence properties of **2**. However, after meticulous purification of **2**, the delayed luminescence was considerably reduced, which is in line with our calculations. To prove that the impurity **2** was responsible for the delayed luminescence in **1**, **2** was doped into **1** resulting in the **2**/**1**

system. For the **2**/**1** mixture, a delayed luminescence signal was detected that corresponded to the fluorescence emission of **2**. As a working hypothesis, we assume that Shoji *et al.* observed delayed luminescence caused by a similar impurity–induced mechanism as discussed in this chapter. In the case of **2**/**1**, the delayed fluorescence of **2** can be easily mistaken as RTP from **1**, as the corresponding excited states are in the same range on the spectrum.

5.2 Computational Details

For our theoretical investigations both the ORCA 5.0.4[71, 72] and the Turbomole[110, 111] program packages were employed. Optimizations were performed at the (u)ωB97X-D3/def2-SVP[77, 95] level of theory. Single point calculations were performed at the (u)ωB97X-D3/def2-SVP and SCS-CC2/def2-TZVP[95, 112–117] levels. The ωB97X-D3 functional was optimally tuned according to the procedure outlined in Chapter 2 to improve the description of charge transfer (CT) states. The letter 't' denotes the use of the optimally tuned functional. All calculations were performed in gas phase, unless otherwise denoted. Testing the accuracy of the DFT methods revealed that standard TD-DFT calculations yield singlet excitation energies which are too high in energy when compared to the experiment. The excitation energies are lower if the functional is optimally tuned, but the lowest values are obtained with the spin component scaled approximate coupled cluster singles and doubles model (SCS-CC2). The SCS-CC2 model as a higher-level method is assumed to give more accurate results. The CPCM model for implicit solvation was tested with the tuned functional but had no effect on the excitation energies as the solvent hexane is nonpolar. The Tamm–Dancoff approximation (TDA) was previously shown to be a good method for calculation of triplet states, therefore we included it in the benchmark.[118] Excited state analysis was performed with the TheoDORE program.[119]

5.3 Results and Discussion

5.3.1 Monomer 1

As we don't know if the experimentally observed absorption (Figure 9.2) is adiabatic, we calculated vertical excitations as well as the energy difference of the S_0 and S_1 equilibrium geometry (see Table 5.1). The SCS-CC2 value is closest to the experimental value (4.46 eV vs 4.34 eV) with a deviation of 0.12 eV. We therefore assume the SCS-CC2 model is the best method to investigate the excited singlet states in this molecule. TD–DFT and TDA give similar vertical excitation energies

for the first two singlet excited states. TD–DFT gives an energy for vertical T_1 that is considerably lower than the TDA value. In comparison to the SCS-CC2 value as a reference, the TDA calculation shows an smaller error than the TD–DFT calculation. The error with respect to SCS-CC2 is 0.84 eV for TD–DFT and 0.23 eV for TDA. For the higher triplet excitations both DFT methods yield similar energies. The calculated stokes shift for the S_1 is 0.2 eV for the SCS-CC2 method. Analogously, relaxation from the S_0 geometry to the T_1 geometry amounts to about 0.3 eV. The optimally tuned functional ($\omega = 0.18$) gives excitation energies that are up to 0.2 eV lower than the non–tuned functional. Remarkably, the T_1 state does not change for TDA regardless of the ω parameter. As the experimental spectra in solution were measured with hexane as a solvent, the CPCM with hexane ($\varepsilon = 1.89$) was tested. The changes in energy are around 0.01 eV which means CPCM has negligible effect on the excitation energies.

Table 5.1: Vertical and adiabatic excitations in **1**. The letter 't' denotes the optimally tuned functional ($\omega = 0.18$). All values given in eV. The experimental absorption peak lies at 4.34 eV.

Vertical Excitations							
Root	**TD–DFT**	**TDA**	**tTD–DFT**	**tTDA**	**SCS-CC2**	**tTD–DFT CPCM (hexane)**	**tTDA CPCM (hexane)**
S_1	5.04	5.11	4.91	4.90	4.66	4.91	4.91
S_2	5.60	5.82	5.51	5.70	5.84	5.46	5.65
T_1	3.13	3.74	3.39	3.77	3.97	3.38	3.78
T_2	4.36	4.44	4.26	4.33	4.60	4.29	4.33
T_3	4.44	4.50	4.31	4.36	4.64	4.35	4.37
T_4	4.71	4.83	4.61	4.66	5.49	4.64	4.67
Adiabatic Excitations							
Root	**TD–DFT**	**DFT (SCF)**	**tTD–DFT**	**tTDA**	**SCS-CC2**	**DLPNO–CCSD(T)**	
S_1	4.97		4.81		4.46		
T_1		3.41		3.42	3.63	3.55	

5.3.2 Monomer 2

RT spectra of **2** show no phosphorescence after purification. Preliminary time gated measurements of **2** in a PMMA film (1 mol%) revealed a signal after 0.1 ms which resembles the prompt fluorescence signal (Figure 9.3). Different methods were also tested for **2** (see Table 5.2). For the vertical excitations the S_1 and the T_1 states are closer in energy than in 1. Again, implicit solvation in hexane has no effect. For the energy differences between TD–DFT and TDA the same trend as for **1** emerges. The vertical T_1 energy is underestimated by TD–DFT in comparison to TDA and

SCS-CC2. The optimally tuned functional ($\omega = 0.16$) lowers the excitation energies by up to 0.2 eV in comparison the the non–tuned functional.

Table 5.2: Vertical and adiabatic excitations in **2**. The letter 't' denotes the optimally tuned functional ($\omega = 0.16$). All values given in eV. The experimental absorption peak lies at 3.58 eV.

Vertical Excitations							
Root	**TD–DFT**	**TDA**	**tTD–DFT**	**tTDA**	**SCS-CC2**	**tTD–DFT CPCM (hexane)**	**tTDA CPCM (hexane)**
S_1	4.16	4.32	3.95	4.02	3.86	3.94	4.00
S_2	4.99	5.20	4.87	5.07	4.90	4.77	4.95
T_1	3.15	3.44	3.19	3.24	3.66	3.26	3.27
T_2	3.34	3.53	3.27	3.47	3.81	3.28	3.47
T_3	4.10	4.27	4.04	4.18	4.44	4.05	4.18
T_4	5.32	5.41	5.11	5.17	5.75	5.10	5.12
Adiabatic Excitations							
Root	**TD–DFT**	**DFT (SCF)**	**tTD–DFT**	**tTDA**	**SCS-CC2**	**DLPNO–CCSD(T)**	
S_1	4.04		3.81		3.67		
T_1		3.16		3.12	3.43	3.29	

Considering the SCS-CC2 value for the adiabatic excitation to the S_1 state, the deviation from the experimental absorption is 0.09 eV. This confirms the SCS-CC2 method is the appropriate choice for excited singlet state investigations. As **2** showed delayed fluorescence in preliminary measurements, we calculated the energy of the T_1 state to check whether a singlet fission mechanism could be at play. We find that the T_1 state is too close to the S_1 state for singlet fission to occur. In recent measurements, we find that **2** shows no delayed luminescence at room temperature. At 77 K there is a delayed fluorescence signal alongside the expected phosphorescence in time gated spectra. The remaining luminescence phenomenon at low temperatures is very likely caused by solid state surface effects or trace impurities, as the in the crystal there is no interaction between monomers and extensive investigations of the molecular excited state potential energy surfaces (PES) yield no reliable explanation of the observation (*vide infra*). As the initial delayed luminescence vanished after thorough purification, we think this is a strong argument that the measurement at 77 K is also contaminated with a vanishing amount of impurity whose effect is enhanced by the low temperature.

5.3.3 Comparison of 1 and 2

To explain possible differences between **1** and **2** we computed the PES of the excited states of the monomers. The relaxation of the geometry after the excitation to the S_1 state was modelled by linearly following the vector that connects the S_0 geometry to

the S_1 geometry. The excitation energies were calculated with the SCS-CC2 method (see Figure 5.2). **1** and **2** show a crossing of the S_1 state with the T_3 and T_2 state, respectively. At these points of the potential energy surface, intersystem crossing (ISC) could be facilitated by the degeneracy of the states. The most important difference in the two molecules is the energetic position of the T_1 state. We assume there could be reverse ISC in compound **2** as the T_1 state is relatively close to the S_1 state. If ISC happens in **1**, the excitation is trapped in the lower lying T_1 state after radiationless relaxation from the T_2 or T_3 state. As we do not observe phosphorescence in **1** at RT, the T_1 is deactivated by further radiationless relaxation, should it ever be populated in the first place.

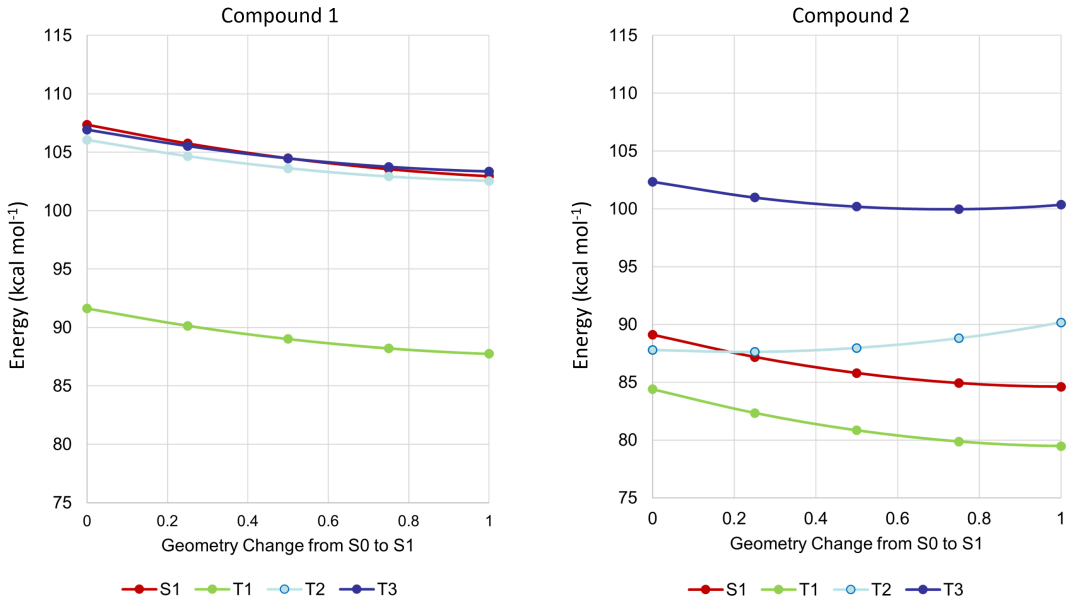

Figure 5.2: Relaxation of the S0 equilibrium geometry to the S1 equilibrium geometry in the first excited state and changes in the potential energy surfaces of compounds **1** and **2**. Values obtained by SCS-CC2 calculations.

To check the probability of ISC in both compounds spin orbit coupling (SOC) matrix elements were calculated on the ground state geometries of the monomers (see Table 5.3).

The SOC matrix elements of the relevant states in **2** are about ten times larger than the ones in **1**. This indicates that ISC in **2** is more efficient than in **1** and could explain why **1** does not show a delayed fluorescence signal while **2** does at 77 K. However, as the T_1 state in **2** lies below the S_1 state, we would expect TADF (thermally activated delayed fluorescence) behavior, i.e. enhanced luminescence intensity with higher temperatures. Temperature dependent measurements showed

Table 5.3: SOC matrix elements of **1** and **2** in the ground state geometry at the tuned ωB97X-D3/def2-TZVP level of theory.

Compound 1		$\langle T\|H_{SO}\|S\rangle$ (Re, Im) cm^{-1}			
T	S	Z	X	Y	amount
1	**1**	(0.00 , –0.02)	(0.00 , –0.06)	(–0.00 , 0.05)	0.081
2	**1**	(0.00 , 0.00)	(0.00 , –0.00)	(–0.00 , –0.01)	0.010
3	**1**	(0.00 , 0.00)	(0.00 , –0.01)	(–0.00 , –0.01)	0.014
Compound 2		$\langle T\|H_{SO}\|S\rangle$ (Re, Im) cm^{-1}			
T	S	Z	X	Y	amount
1	**1**	(0.00 , 0.00)	(0.00 , –0.00)	(–0.00 , –0.00)	0.000
2	**1**	(0.00 , 0.02)	(0.00 , 0.06)	(–0.00 , 0.14)	0.154
3	**1**	(0.00 , –0.03)	(0.00 , –0.00)	(–0.00 , –0.09)	0.095

that luminescence intensity decreases with higher temperatures, which contradicts the typical TADF mechanism.

As we are investigating a process that happens in the first excited singlet state, we calculated relaxed PES scans along prominent coordinates such as the rotation of the Bpin group in both **1** and **2** and the distance of the amino proton in **2** and the oxygen which is part of the neighboring Bpin group (see Figure 5.3).

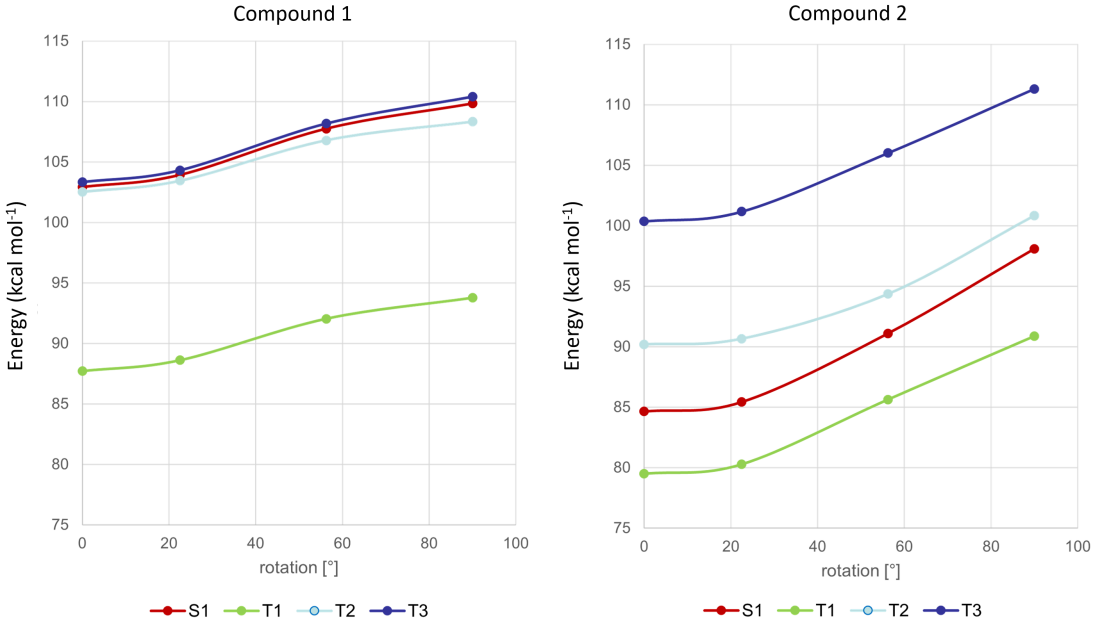

Figure 5.3: Relaxed scans that show the rotation of the Bpin group in the S_1 state for compounds **1** and 2. Values obtained by SCS-CC2 calculations.

Again, we see a different distribution of the excited states on the energy scale. In **1** the T_1 is considerably lower than either the S_1, T_2 or T_3 state. In **2** the T_1 and S_1 state remain in closer energetic proximity. Along the scan coordinate all states

remain parallel and we do not observe any degeneracies. The rotation in **2** is considerably hindered in comparison to **1** which can be rationalized by the two hydrogen bonds at the NH_2 group that hold the Bpin groups in an in-plane conformation. In **1** the Bpin groups can rotate more freely as the NH_2 group is missing.

As the NH_2 group is the distinctive feature of compound **2**, we tried to model a proton transfer from the amino group to the adjacent Bpin oxygen, which could be facilitated by CT from the N substituents to the Bpin residues in the S_1 state. By analysis of the $S_0 \rightarrow S_1$ transition (HOMO→LUMO), we learn two things about the electron-hole pair in the S_1 state:
Firstly, the hole is delocalized mainly over the benzene(NH_2)(CN) fragment (as this is where the HOMO is delocalized). The arene core contributes about 60% to the HOMO/exciton hole, whereas the N–substituents contribute about 36%.
Secondly, the electron is delocalized over the benzene$(Bpin)_2$ fragment. The arene core contributes about 75%, the two Bpin groups take up 25% of the electron.

This means the net charge flow is going from both N-substituents (loss of about 36% of an electron) to the Bpin groups (gain of about 25% of an electron) and the arene core (+11%). If we look at just the amino group, the electron loss on NH_2 is about 26%. This minor CT effect in the S_1 state is only slightly noticeable in a widening of the N-H bond. As you can see in Figure 5.4, the minimum of the S_1 state is shifted by 0.1 Å towards a shorter H ... O(Bpin) distance. Nevertheless, the proton is not transferred to the Bpin group, as we do not find a second minimum in the scan.

5.3.4 Dimers of 1 and 2

To model the situation in the solid state, i.e. the crystal, the dimer approach[120] was applied. An appropriate dimer was cut out of the crystal lattice and the monomer positions were replaced by the previously optimized monomer geometries. The goal was to improve the crude crystal structure which describes the hydrogen positions poorly.

The calculated singlet excitations using the standard TD-DFT method show no Davydov splitting and we only observe pure Frenkel states, i.e. localized excitations (see Table 5.4). Even when forcing the dimer in the CT geometry, meaning replacing one structure by the corresponding cation geometry and the other by the anion geometry, we see no CT character for the first five singlet states. We rationalize this

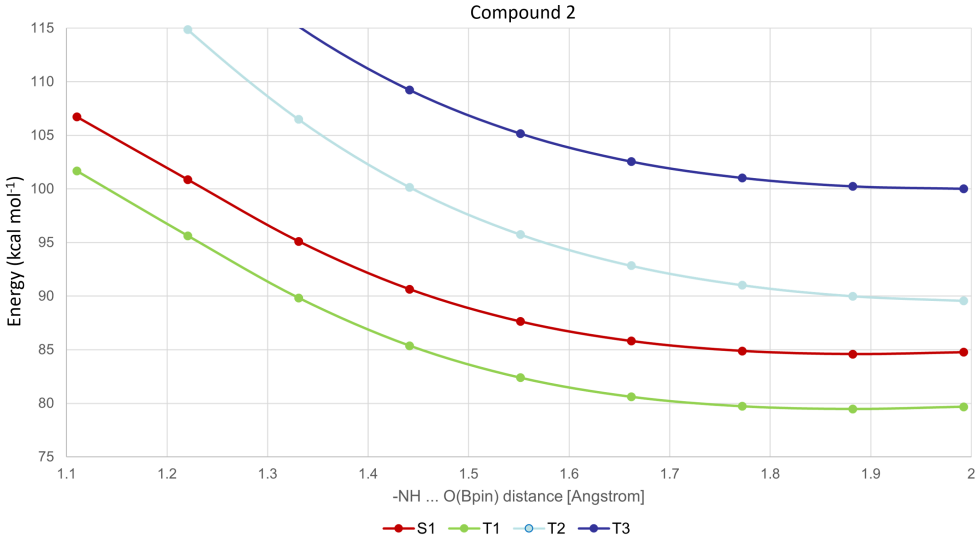

Figure 5.4: Relaxed scan of the -NH ... O(Bpin) distance in compound **2** in the S_1 state. Values obtained by SCS-CC2 calculations.

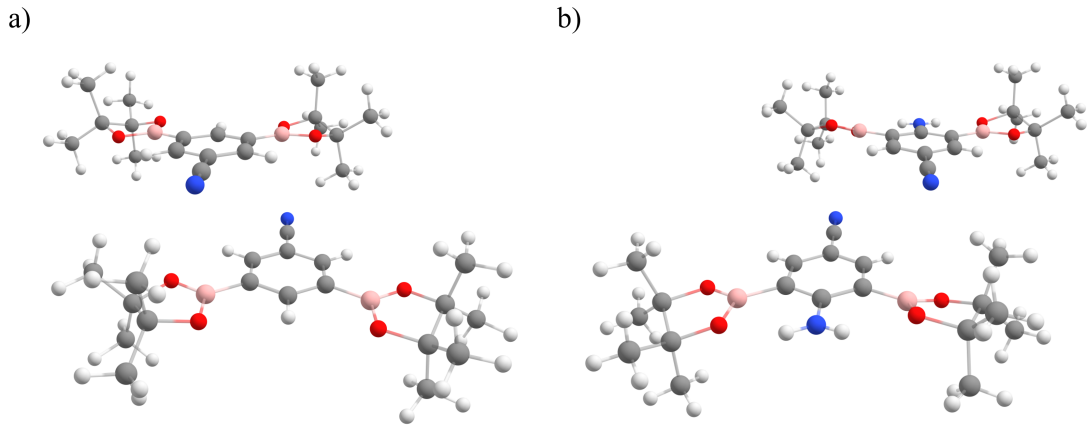

Figure 5.5: The dimer structures of **1** (a) and **2** (b) that were found by investigation of the respective crystal lattice.

result by the distance between the monomers (about 3.3 Å) and the displacement of the central benzene rings. As there is no direct contact of the π systems, there is also no interaction (CT) between the corresponding monomers. Also notice that the first excited states of **1** are dark, as the transition dipole moment is zero. Similarly to compound **1**, we observe no interaction between monomers of **2**, even in a forced CT geometry. The π systems are not properly stacked on top of each other. Notice that the oscillator strength (f) is generally larger than for **1**.

Table 5.4: Vertical excitations of homo dimers of **1** and **2**. Excitations were calculated both for the ground state as well as the simulated charge transfer (CT) geometry. All energy values given in eV.

		Compound 1			Compound 2		
Homo-Dimer Geometry	Root	dE(eV)	f	CT	dE(eV)	f	CT
Both monomers in the ground state	S_1	5.03	0.000	0.01	4.19	0.013	0.00
	S_2	5.03	0.000	0.01	4.20	0.321	0.00
	S_3	5.57	0.001	0.02	4.98	0.000	0.01
	S_4	5.58	0.012	0.01	5.00	0.430	0.00
	S_5	6.13	0.001	0.02	6.11	1.729	0.01
One monomer in anion and one in cation geometry (CT geometry)	S_1	4.84	0.006	0.01	3.89	0.165	0.00
	S_2	4.94	0.002	0.01	4.08	0.186	0.00
	S_3	5.25	0.099	0.02	4.83	0.272	0.01
	S_4	5.34	0.145	0.01	4.97	0.073	0.00
	S_5	6.03	0.318	0.03	5.71	0.897	0.02

5.3.5 Investigation of the 2/1 Mixture

Experiments show that delayed fluorescence can be achieved by doping **2** into a matrix of **1** (Figure 9.4). To investigate this effect, the dimer approach was chosen. We took the previously built dimer of **1** and replaced one of the monomers by an optimized monomer of **2**, and thus, modeled a hetero dimer **2**/**1**.
We permutated the monomer geometries and calculated different combinations of the corresponding dimer. For instance, the first column in Figure 5.6 describes both monomers in S_0 geometry, whereas in the last column describes both monomers in the S_1 geometry.

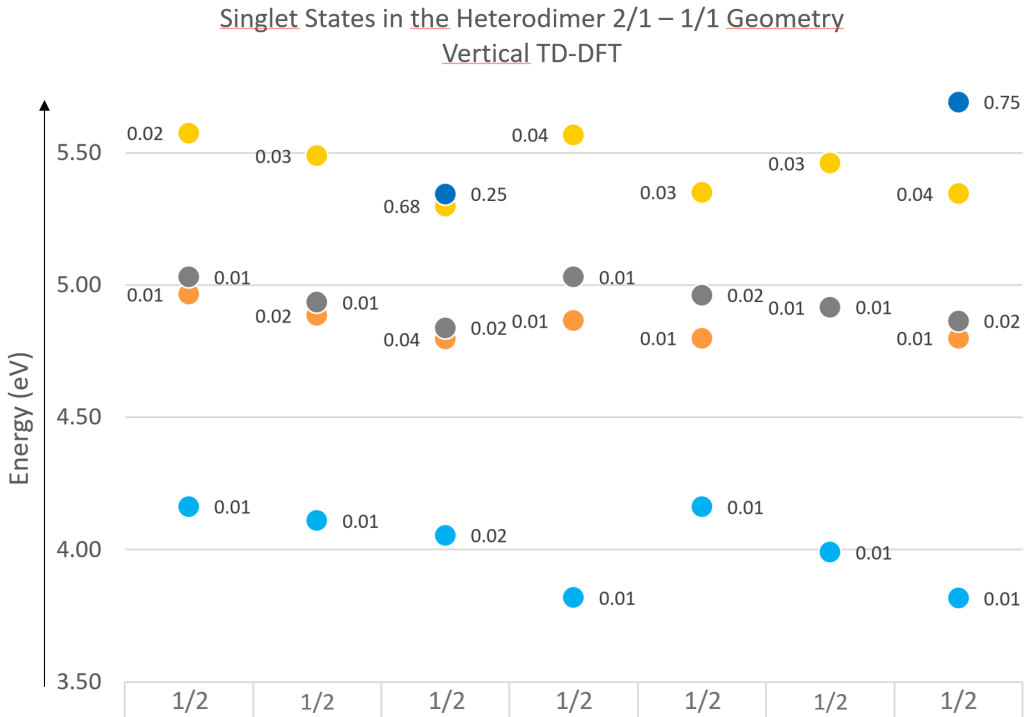

	1/2 S0/S0	1/2 0.5–/0.5+	1/2 –/+	1/2 S0/S1	1/2 S1/S0	1/2 S0.5/S0.5	1/2 S1/S1
S1	4.16	4.11	4.05	3.82	4.16	3.99	3.82
S2	4.96	4.88	4.80	4.87	4.80	4.91	4.80
S3	5.03	4.93	4.84	5.03	4.96	4.92	4.86
S4	5.57	5.49	5.30	5.57	5.35	5.46	5.34
S5	6.01	5.73	5.34	5.85	5.82	5.86	5.69

Figure 5.6: Vertical singlet excitations in the hetero dimer 2/1. The monomers were placed in a 1/1 geometry as it can be found in a pure crystal of **1**. On the x axis you can see some possible permutations of the corresponding geometries. S_0/S_0 denotes both monomers in the S_0 geometry. 0.5–/0.5+ denotes that **1** is of mixed geometry between S_0 and the anionic structure, for **2** that is the mix between S_0 and the cation geometry. The values next to the dots are the corresponding CT character of the excitation. Method: Not tuned ωB97X-D4/def2-TZVP.

We learn from Figure 5.6 that if we put **2** in the crystal lattice of **1**, we do not see any CT states except if we force the system into a CT geometry. In the CT geometry, we defined **2** as the electron richer donor and **1** as the electron deficient acceptor, hence **2** was optimized as a cation and **1** as an anion. Furthermore, the first singlet state is more stable by 0.34 eV if the dimer assumes the S_0/S_1 geometry instead of the S_1/S_0 geometry. In other words, when monomer **2** is allowed to relax in the S_1 state and **1** is frozen at the groundstate geometry (S_0/S_1), more energy is gained in comparison to the equivalent relaxation of monomer **1** (S_1/S_0). Hence, we expect the exciton to localize on **2**.

Because there is no apparent interaction between the monomers, which is not unexpected as in the pure compounds there is no monomer–monomer interaction either, we tried a different approach. Instead of placing **2** (as the impurity) in a crystal lattice spot of **1**, we froze the optimized monomer geometries and optimized the distance between the monomers. We argue that a crystal defect will not resemble the same geometry as the bulk of the crystal lattice, therefore it should be possible for the impurity **2** to be displaced from the original lattice spot and come into closer contact with the matrix, i.e. a monomer of **1** (Figure 5.7).

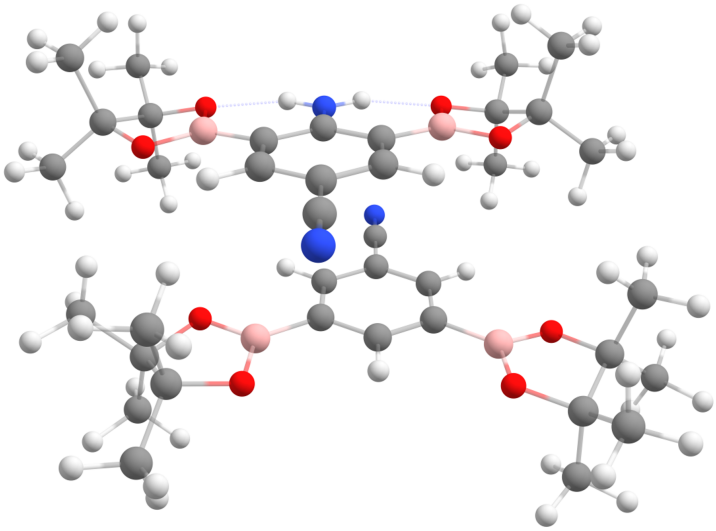

Figure 5.7: Heterodimer with optimized relative distance between **1** (bottom) and **2** (top).

If we revisit the excited states of such a displaced impurity position, we see that CT states start to appear and the monomers of the hetero dimer are interacting, see Figure 5.8.

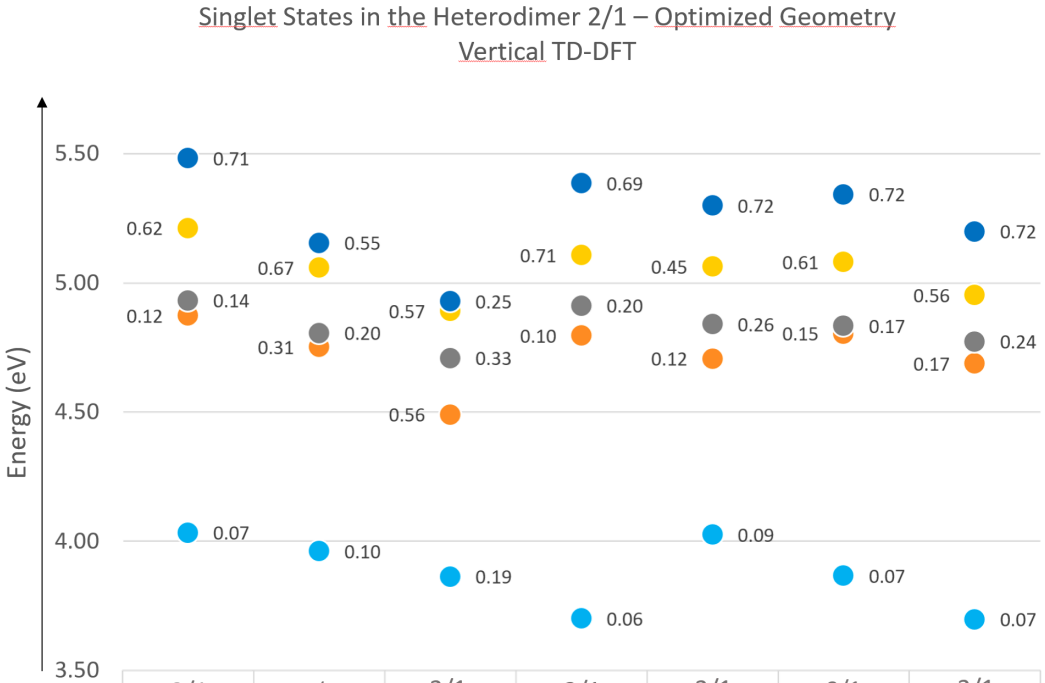

	2/1 S0/S0	2/1 0.5+/0.5–	2/1 +/–	2/1 S1/S0	2/1 S0/S1	2/1 S0.5/S0.5	2/1 S1/S1
S1	4.03	3.96	3.86	3.70	4.03	3.87	3.70
S2	4.87	4.75	4.49	4.80	4.71	4.80	4.69
S3	4.93	4.81	4.71	4.91	4.84	4.83	4.77
S4	5.21	5.06	4.89	5.11	5.06	5.08	4.95
S5	5.48	5.15	4.93	5.39	5.30	5.34	5.20

Figure 5.8: Vertical singlet excitations in the hetero dimer 2/1. The relative position of the monomers was optimized, to model a crystal defect. On the x axis you can see some possible permutations of the corresponding geometries. S_0/S_0 denotes both monomers in the S_0 geometry. 0.5–/0.5+ denotes that **1** is of mixed geometry between S_0 and the anionic structure, for **2** that is the mix between S_0 and the cation geometry. The values next to the dots are the corresponding CT character of the excitation. Method: Not tuned ωB97X-D4/def2-TZVP.

As the presented values were calculated using the standard ωB97X-D4 functional without optimal tuning, we expect the CT state energies to be overestimated. Hence, we repeated the calculation with optimally tuned DFT ($\omega = 0.14$) and suggest the mechanism presented in Figure 5.9.

If a doped **2**/**1** system is excited, both **1** and **2** emit prompt fluorescence, but as the concentration of **2** is low, we only observe prompt fluorescence of **1**. Because the S_1 state of **1** is essentially a dark state with a close to zero transition dipole moment, we assume that excitons are hopping around the matrix **1** with a considerable lifetime. The matrix exciton is either deactivated by a radiationless process or

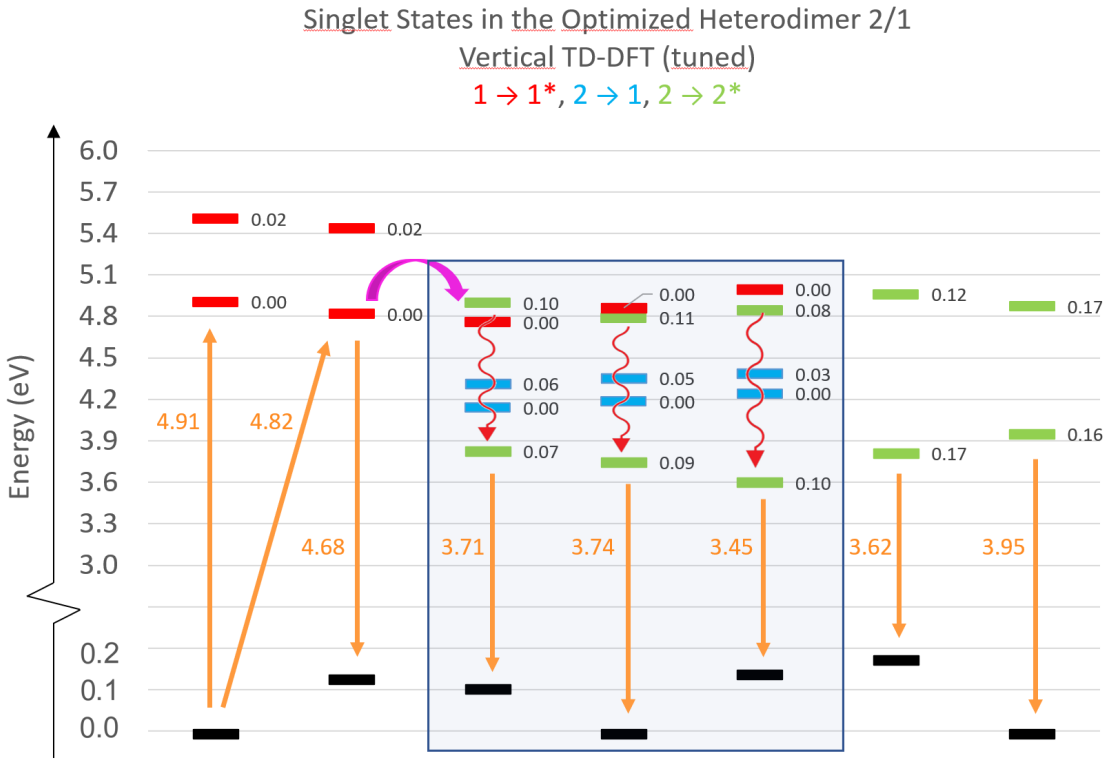

	1 S0	1 S1	2/1 S0/S1	2/1 S0/S0	2/1 S1/S0	2 S1	2 S0
S1	4.91	4.82	3.82	3.74	3.60	3.81	3.95
S2	5.51	5.44	4.14	4.19	4.24	4.96	4.87
S3			4.31	4.35	4.39		
S4			4.76	4.79	4.85		
S5			4.90	4.86	5.00		
S0	0.00	0.14	0.11	0.00	0.15	0.19	0.00

Figure 5.9: Vertical singlet excitations in the hetero dimer 2/1. The relative position of the monomers was optimized to model a crystal defect. Method: Optimally tuned ωB97X-D4/def2-TZVP. Note that the values next to the states are the transition dipole moments of the excitation. The color of the excitation corresponds to the localization of the exciton. Red excitations are localized on 1, green excitations are localized on **2** and blue excitations resemble CT states.

it encounters an impurity, i.e. a hetero dimer **2**/**1**. Here a new radiationless deactivation pathway opens via CT states on the impurity **2** (see Figure 5.9, blue lines). As a consequence, the S_1 state of **2** is populated with a certain time delay. Because the transition dipole moment for the S_1 state of **2** is considerably larger than the corresponding value in **1**, the exciton is deactivated by fluorescence emission which we observe experimentally during time gated measurements.

Figure 5.10 depicts the natural transition orbitals (NTO) that were obtained by

analyzing the vertical excitations of the heterodimer in its groundstate geometry with the TheoDORE program package.
Considering the highest calculated excitation (S_5), the exciton exhibits a mixed character which is composed of two distinct occupied NTOs. Both NTOs are of π symmetry and are located on the host **1**. The excitation corresponds to the S_1 state of **1**, as can be seen in Figure 5.9. All excitations below S_5 feature the exciton hole on the guest **2**, the corresponding NTO is comparable to the HOMO of **2**. The S_4 state is mainly localized on **2** and is therefore the equivalent to the S_2 state of the monomer. States S_3 and S_3 resemble CT states, in which the charge is transferred from the electron rich donor **2** to the electron deficient acceptor **1**. The lowest excited state S_1 is localized on the guest **2**, which is in accordance with the experimental observation of the characteristic emisson of **2** in time–gated measurements.

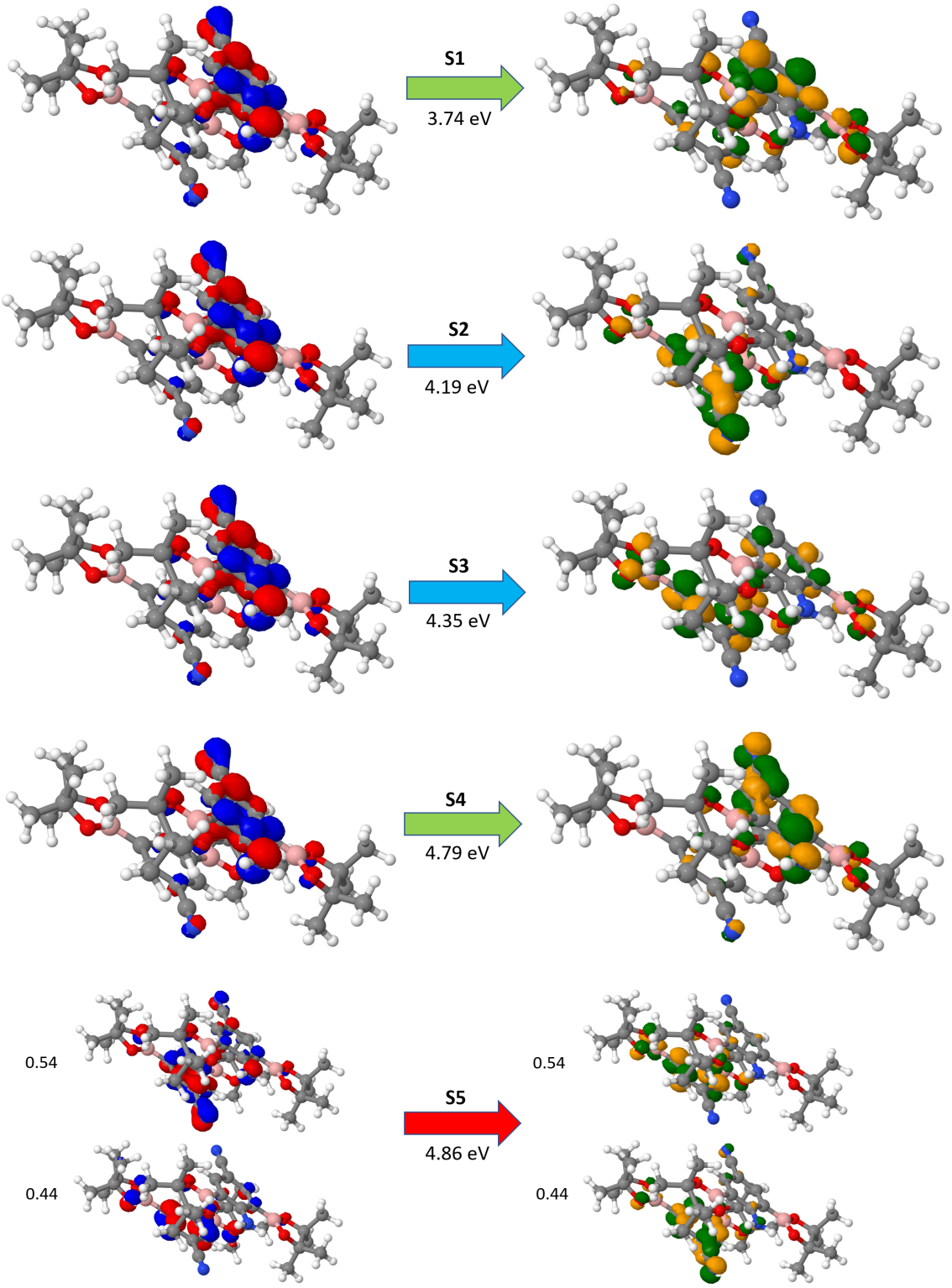

Figure 5.10: Natural transition orbitals in the hetero dimer **2**/**1**. Exciton-hole orbitals are depicted on the left and exciton-electron orbitals are depicted on the right. The color of the excitation corresponds to the localization of the exciton. Red excitations are localized on **1**, green excitations are localized on **2** and blue excitations resemble CT states.

5.3.6 Compound 3

As a benchmark, basis set effects were investigated on compound **3** (see Table 5.5). Going from a double zeta basis to larger minimally augmented (def2 family) or augmented (cc family) basis sets slightly reduces the excitation energy, but the deviation is within a 0.1 eV margin for the important first three excited states.

Table 5.5: Monomer calculations of **3** at the ground state geometry with ωB97XD or SCS-CC2 and different basis sets.

ωB97XD	def2-SVP		def2-TZVP		ma-def2-SVP		ma-def2-TZVP		ma-def2-QZVP	
Root	eV	f	eV	f	eV	f	eV	f	eV	f
S_1	5.04	1.132	4.95	1.108	4.98	1.087	4.94	1.087	4.94	1.087
S_2	5.17	0.010	5.10	0.010	5.12	0.012	5.09	0.011	5.08	0.011
S_3	5.18	0.002	5.11	0.002	5.13	0.003	5.10	0.002	5.09	0.002
S_4	6.07	0.000	5.95	0.000	5.99	0.000	5.93	0.000	5.93	0.000
S_5	6.48	0.054	6.31	0.048	6.32	0.049	6.25	0.043	6.24	0.047

SCS-CC2	cc-pVDZ		cc-pVTZ		aug-cc-pVDZ	
Root	eV	f	eV	f	eV	f
S_1	4.82	0.001	4.74	0.001	4.74	0.001
S_2	4.83	0.006	4.75	0.006	4.75	0.007
S_3	5.19	1.330	5.08	1.272	5.05	1.234
S_4	6.29	0.000	6.14	0.000	5.83	0.004
S_5	6.61	0.053	6.41	0.046	6.10	0.000

The effect of implicit solvation was investigated by single point calculations on the gas phase structure (Table 5.6). The influence of the non–equilibrium solvent shell is negligible. If the solvent shell is in equilibrium with the S_1 state, the vertical excitation is 0.14 eV lower in energy in comparison to the vacuum calculation. Excited states S_2–S_4 remain unaffected.

Table 5.6: Monomer calculations of compound **3** with wB97XD/def2-SVP and implicit solvation (linear response CPCM, Me-THF: $\varepsilon = 6.97$, refraction index 1.407). The middle column shows excitations with the ground state solvation shell, the right column shows the solvation shell in equilibrium with the first excited state.

TD-DFT	S_0 geom **vacuum**		S_0 geom **GS solvation**		S_0 geom **equilibrium**	
Root	eV	f	eV	f	eV	f
S_1	5.04	1.132	4.97	1.269	4.90	1.390
S_2	5.17	0.010	5.17	0.018	5.16	0.032
S_3	5.18	0.002	5.18	0.004	5.17	0.006
S_4	6.07	0.000	6.04	0.000	6.00	0.000
S_5	6.48	0.054	6.38	0.079	6.27	0.110

When we look at the adiabatic transition, the energy is lowered by 0.2 eV in comparison to the gas phase calculations (Table 5.7). Including the solvent model, the transition moves very close to the experimental emission (onset at ca. 300 nm).

The vertical emission from S_1 is at 3.74 eV (332 nm) with solvent, which is in the middle of the vibrational progression observed in the spectrum (Figure 9.5). We observe again that S_2 and S_3 are unaffected by the solvent shell.

Table 5.7: Monomer calculations of compound **3** with ωB97XD/def2-SVP and implicit solvation (linear response CPCM, Me-THF: $\varepsilon = 6.97$, refraction index 1.407). Comparison of adiabatic excitation to the S_1 equilibrium geometry in gas phase and with implicit solvation. The S_1 geometry is 0.42 eV above the equilibrium geometry on the S_0 PES with solvation.

TD-DFT	S_1 geometry **vacuum**	S_1 geometry **equilibrium solvation**
Root	eV	eV
S_1	4.39 (282 nm)	4.16 (298 nm)
S_2	5.16	5.13
S_3	5.35	5.30
S_4	6.23	6.04
S_5	6.34	6.21

Interestingly, TD-DFT predicts the HOMO→LUMO transition to be the lowest excited singlet state (S_1 state), whereas SCS-CC2 finds two states of mixed character below the HOMO→LUMO transition (see Table 5.8). The HOMO→LUMO transition results in a state of B_1 symmetry. As the relevant π MOs of **3** resemble that of unsubstituted biphenyl, we compare our results to the literature on simple biphenyl. Fukada *et al.*[121] found that the HOMO→LUMO transition has intramolecular charge transfer character.

Table 5.8: Vertical transitions in **3** with the SCS-CC2 method. The bright S_3 state is corresponding to the HOMO → LUMO transition.

Singlet states on S_0 geometry	Main contribution	SCS-CC2 natural orbitals	
S_1	ca. 50 %	107 → 110	HOMO-2 → LUMO
S_2	ca. 50 %	108 → 110	HOMO-1 → LUMO
S_3	ca. 90 %	109 → 110	HOMO → LUMO

They attributed the poor description of the state in comparison to the other states by TD-DFT to nondynamical correlation effects. In contrast to the literature, we find that the bright HOMO→LUMO transition is predicted uniformly by ωB97XD/def2-SVP and the more sophisticated SCS-CC2/cc-pVTZ to lie at about 5 eV (see Table 5.5). Instead, two other states are overestimated by DFT in comparison to SCS-CC2. In a paper by B. Roos[122] the lowest excited singlet state of the simple biphenyl compound is also assigned another symmetry than B_1. This

is supported by our SCS-CC2 calculations, as the B_1 state appears to be the third excited singlet state S_3 (see Table 5.9).

Table 5.9: Monomer calculations of **3** with wB97XD/def2-SVP and SCS-CC2/cc-pVTZ. CT character is defined between the connecting carbon atoms in the biphenyl moiety [C1, C1'] and the rest of the molecule. We can confirm that the bright transition has a somewhat higher CT character than the rest of the transitions. On the S_0 PES, the S_1 geometry is 0.44 eV and the T_1 geometry 0.76 eV higher in energy than the S_1 equilibrium geometry.

Root	eV	f	CT	eV	f	CT	eV	f	CT
TD-DFT	S_0 geometry			S_1 geometry			T_1 geometry		
S_1	5.04	1.132	0.368	4.39	1.208	0.362	4.70	1.524	0.350
S_2	5.17	0.010	0.269	5.16	0.000	0.253	5.45	0.000	0.245
S_3	5.18	0.002	0.270	5.35	0.024	0.256	5.66	0.026	0.249
S_4	6.07	0.000	0.270	6.23	0.000	0.259	6.59	0.000	0.345
S_5	6.48	0.054	0.276	6.34	0.000	0.301	6.79	0.000	0.251
T_1	3.61	0.000	0.333	2.99	0.000	0.357	3.01	0.000	0.352
T_2	4.16	0.000	0.250	4.43	0.000	0.348	4.66	0.000	0.367
T_3	4.54	0.000	0.268	4.56	0.000	0.266	4.79	0.000	0.261
T_4	4.55	0.000	0.269	4.69	0.000	0.266	4.92	0.000	0.261
T_5	4.73	0.000	0.072	5.13	0.000	0.257	5.38	0.000	0.248
SCS-CC2	S_0 geometry			S_1 geometry			T_1 geometry		
S_1	4.74	0.001	0.269	4.43	1.394	0.339	4.47	1.417	0.336
S_2	4.75	0.006	0.269	4.58	0.000	0.271	4.76	0.000	0.268
S_3	5.08	1.272	0.333	4.87	0.016	0.273	5.06	0.017	0.270
S_4	6.14	0.000	0.268	6.01	0.000	0.281	6.11	0.000	0.343
S_5	6.41	0.046	0.281	6.09	0.000	0.341	6.17	0.000	0.276
T_1	3.73	0.000	0.315	3.06	0.000	0.340	3.06	0.000	0.338
T_2	4.29	0.000	0.261	4.49	0.000	0.315	4.68	0.000	0.328
T_3	4.67	0.000	0.262	4.59	0.000	0.275	4.78	0.000	0.273
T_4	4.68	0.000	0.263	4.79	0.000	0.275	4.99	0.000	0.274
T_5	4.81	0.000	0.186	5.28	0.000	0.158	5.64	0.000	0.150

As the delayed fluorescence effect exists only in the solid state (Figure 9.6), we investigated the geometry of **3** in the crystal. **3** exhibits a twisted and bend geometry which is caused by packing effects and can not be reproduced by a standard monomer gas phase calculation. Hence, we considered the surrounding solid-state environment explicitly in the dimer optimization. This was achieved by an ONIOM calculation at the wB97X-D3/def2-SVP:XTB level of theory. Figure 5.11 shows the dimer as the active region of the calculation, all other coordinates were frozen.

Table 5.10 shows that for **3** DFT and SCS-CC2 are in good agreement, in contrast to **1** and **2** for which DFT is overestimating the excitation energies. The changes in geometry that are caused by the crystal packing appear to be small, except for the

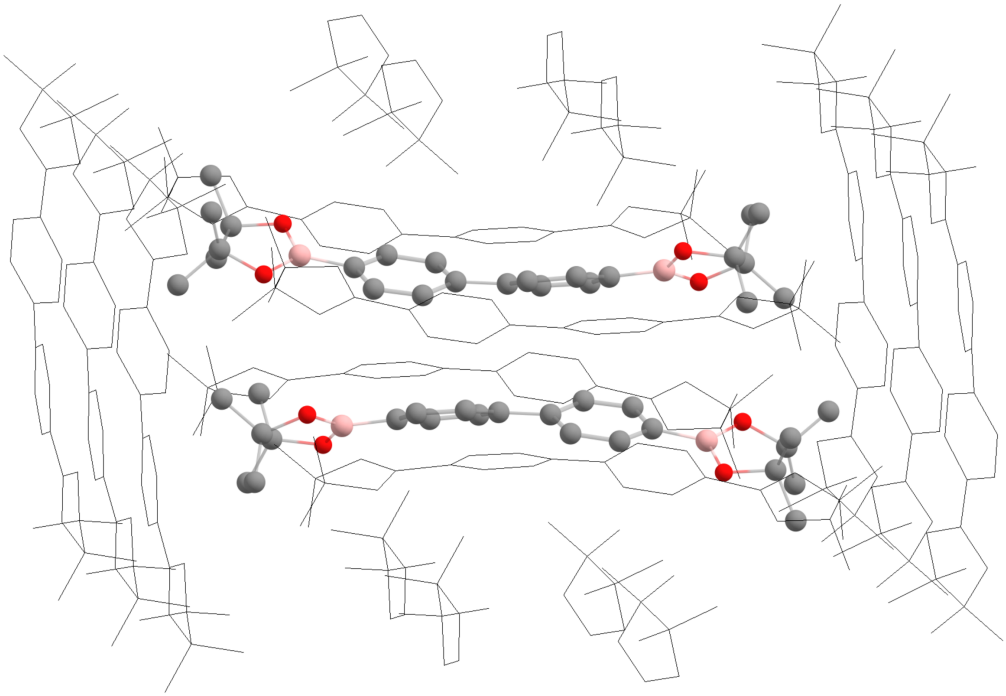

Figure 5.11: Dimer of compound **3** inside of the crystal lattice. The outer molecules that are depicted by black lines were frozen during the optimization to model the solid-state environment. Hydrogens omitted for clarity.

vertical T_1 energy. There is a difference of 0.3 eV between the optimized dimer and the optimized monomer.

Table 5.10: Vertical and adiabatic emission of **3** from the S1 and T1 states. DFT (=ωB97XD/def2-SVP) shows good agreement with SCS-CC2.

Emission eV(nm)	Dimer DFT	Monomer DFT	Monomer SCS-CC2
adiabatic S_1	4.38 (283)	4.39 (282)	4.43 (280)
vertical S_1	3.91 (317)	3.95 (314)	4.06 (305)
adiabatic T_1	3.04 (408)	3.02 (411)	3.06 (406)
vertical T_1	2.54 (489)	2.26 (549)	2.42 (513)

Because the dimer is too large to use the SCS-CC2 method, we resort to TD–DFT calculations. The dimer calculation for the ground state suggests that compound **3** forms an H–aggregate in the crystal (see Table 5.11). The S_1 transition is dipole forbidden, whereas the S_2 transition is bright (f = 1.879). The S_1 exciton on the ground state geometry is fully delocalized over the dimer and no CT character is observed. When the geometry is relaxed for the S_1 state, the exciton localizes on one monomer and the lowest excited singlet state becomes bright. Important to keep in mind for the comparison of the monomer and dimer calculations is the conformation

of the molecule in gas phase vs in the solid. In the gas phase the monomer is linear whereas in the solid the long axis of the molecule is bent, which means the two phenyl rings are twisted and slightly bent towards each other. Thus, there are no dark states (f = 0.000) in the relaxed S_1 conformation of the dimer (Table 5.11), whereas we observe them in the more symmetric gas phase monomer (Table 5.9). The energies seem to be unaffected by the different conformations. Because the S_1 transition in the H–aggregate is dipole forbidden, a delayed luminescence could be explained by the necessary slow geometry relaxation by which the S_1 state becomes bright.

Table 5.11: Dimer calculations with wB97XD/def2-SVP, CT character is defined between two monomers. Geometries obtained from crystal cluster calculations. Twisted and bent conformation of the solid state is retained. On the S_0 PES, the S_1 geometry is 0.47 eV and the T_1 geometry 0.50 eV higher in energy than the S_0 equilibrium geometry.

DFT	S_0 geometry			S_1 geometry			T_1 geometry		
Root	eV	f	CT	eV	f	CT	eV	f	CT
S_1	4.82	0.000	0.037	4.38	0.730	0.038	4.39	0.831	0.025
S_2	4.99	1.879	0.015	5.16	0.021	0.029	5.20	0.003	0.022
S_3	5.09	0.015	0.024	5.22	1.006	0.105	5.32	0.308	0.097
S_4	5.10	0.000	0.025	5.35	0.225	0.020	5.40	0.831	0.045
S_5	5.13	0.000	0.014	5.51	0.022	0.032	5.58	0.036	0.034
S_6	5.15	0.063	0.010	5.56	0.012	0.054	5.62	0.009	0.069
S_7	5.99	0.034	0.216	5.86	0.050	0.868	5.94	0.046	0.858
S_8	5.99	0.000	0.095	5.99	0.011	0.765	6.06	0.023	0.781
S_9	6.19	0.059	0.692	6.17	0.010	0.123	6.22	0.007	0.102
S_{10}	6.23	0.000	0.846	6.28	0.011	0.181	6.30	0.011	0.169
T_1	3.53	0.000	0.011	3.05	0.000	0.012	3.04	0.000	0.011
T_2	3.54	0.000	0.009	3.90	0.000	0.017	4.00	0.000	0.014
T_3	4.13	0.000	0.012	4.41	0.000	0.019	4.41	0.000	0.016
T_4	4.15	0.000	0.009	4.58	0.000	0.022	4.62	0.000	0.017
T_5	4.46	0.000	0.016	4.61	0.000	0.015	4.65	0.000	0.015
T_6	4.47	0.000	0.014	4.71	0.000	0.021	4.74	0.000	0.019
T_7	4.52	0.000	0.012	4.89	0.000	0.024	4.95	0.000	0.021
T_8	4.52	0.000	0.013	4.95	0.000	0.022	5.01	0.000	0.017
T_9	4.69	0.000	0.015	5.11	0.000	0.018	5.16	0.000	0.016
T_{10}	4.70	0.000	0.012	5.15	0.000	0.022	5.19	0.000	0.020

If we decompose the dimer into monomers and keep the bent and twisted dimer geometry, we get the monomer values summarized in Table 5.12. The monomer ground state in the dimer geometry is destabilized by less than 0.1 eV in comparison to the free monomer. This means, the bending of the molecule in the crystal has a minor effect on the energy in comparison to the linear gas phase structure. The

vertical excitation on the separated monomers is identical as the dimer is symmetric in the ground state. After relaxation of the S_1 state, monomer A stays in the S_0 geometry (energy change 0.01 eV) whereas monomer B adopts the S_1 geometry which is higher in energy (e.g. DFT: 0.47 eV). Consequently, the excitation localizes on monomer B and we get similar excitation energies as for the free monomer (compare Table 5.10). The difference of the two monomers in the S_1 geometry is larger for the DFT calculation (0.41 eV DFT, 0.15 eV SCS-CC2, last column Table 5.12). For DFT the S_1 state is consisting of the bright HOMO–LUMO transition on both the S_0 and S_1 geometries. Therefore, we see the full effect of the S_1 relaxation. The HOMO–LUMO transition is also stabilized in the SCS-CC2 calculation, but the S_1 excited state in the S_0 geometry has a different excitation character, see previous results (Table 5.9). The HOMO–LUMO transition at the ground state geometry lies at 5.00 eV (S_3, SCS-CC2) for both monomer A and B and is also lowered by 0.5 eV to 4.5 eV in the S_1 geometry, similarly to the DFT calculation. The S_1 state on monomer B (4.65 eV) is not the HOMO–LUMO transition, but a mixed character state.

Table 5.12: Monomer calculations of compound **3** with wB97XD/def2-SVP and SCS-CC2/cc-pVTZ in gas phase. First column: Ground state energy of the monomer optimized in gas phase. Rest: Monomers A and B in the respective dimer geometries.

DFT / [eV]	vacuum opt (free M)	crystal opt	vertical S_1 in S_0 geom	S_0 in dimer with S_1 geom	S_1 in dimer with S_1 geom
Monomer A	-0.07	0.00	4.95	0.01	4.87
Monomer B	-0.07	0.00	4.95	0.47	4.46
SCS-CC2 / [eV]	vacuum opt (free M)	crystal opt	vertical S_1 in S_0 geom	S_0 in dimer with S_1 geom	S_1 in dimer with S_1 geom
Monomer A	-0.06	0.00	4.69	0.01	4.65
Monomer B	-0.06	0.00	4.69	0.39	4.50

Considering these results, we expect the emission spectrum of **3** in the solid state to resemble closely the one which is measured in solution as the exciton is localized on a single monomer and there is no cooperative effect in the dimer.

Another possible explanation to the delayed luminescence might be the 'hot exciton' mechanism. SCS-CC2 calculations on the monomer predict that for the S_1 geometry the T_2 state is close to the S_1 state and the T_1 state is about 1.5 eV lower than both S_1 and T_2 (see Table 5.9). In the literature a 'hot exciton' mechanism[123] is proposed for compounds with an electronic structure like this. There is also experimental proof of this mechanism.[124] The theory is that a large T_1–T_2 energy gap makes the internal conversion from T_2 to T_1 so slow that reverse intersystem

crossing to the singlet manifold becomes competitive. This mechanism is different from TADF where Kasha's rule is obeyed and a small S_1–T_1 gap is at play.

5.4 Conclusions

In summary, the potential energy surfaces of the excited states in compounds **1** and **2** were thoroughly investigated and no reason for the initially experimentally observed luminescence phenomena was found. This result was proven correct by subsequent meticulous purification of both compounds by our coworkers in the Marder group. Because **2** was found as an impurity in **1**, the doped **2**/**1** system was investigated as well. The observed delayed luminescence of the doped host **1** is attributed to delayed fluorescence from the guest molecule **2**. The mechanism can be summarized as follows: Because the transition dipole moment of the singlet states in the host **1** is much smaller than in the guest **2**, excitons in the host have considerable life time. The portion of excitons which is not destroyed by fluorescence emission or vibrational relaxation eventually encounters a defect in the crystal in the form of an impurity **2**. At the site of the impurity, which was modeled by the dimer approach, an additional relaxation pathway opens for the exciton. Via two CT states that connect the host **1** and the guest **2**, the first singlet excited state of **2** is populated. Subsequent fluorescence emission from **2** can be detected after a prolonged time, which is attributed to the slow relaxation process at the impurity site. Because the fluorescence emission of **2** appears in the same region of the spectrum as the T_1 state of **1**, it can be easily mistaken as phosphorescence by **1**. For compound **3** the analysis of the excited state PES remains somewhat inconclusive. We observed significant differences in state ordering when TD–DFT and SCS-CC2 are compared. In any case, **3** seems to form H–aggregates in the solid state, which exhibit a dark first singlet excited state. After excitation, we expect the initially delocalized exciton to localize on one monomer, and as no cooperative effects were found, we predict that the solid state spectrum should closely resemble the monomer emission spectrum. An explanation for the weak delayed fluorescence emission of **3** is possibly the slow geometry relaxation of the S_1 state, which is considerably hindered in the solid state. This is evidenced by the significant influence of the crystal environment on the geometry of the compound. The electronic structure of **3** hypothetically also allows for the "hot exciton" mechanism which would explain delayed luminescence by repopulation of the S_1 state some time after the short fluorescence time window.

6 Investigation of RedOx Chemistry and Singlet–Triplet Gaps

6.1 Introduction

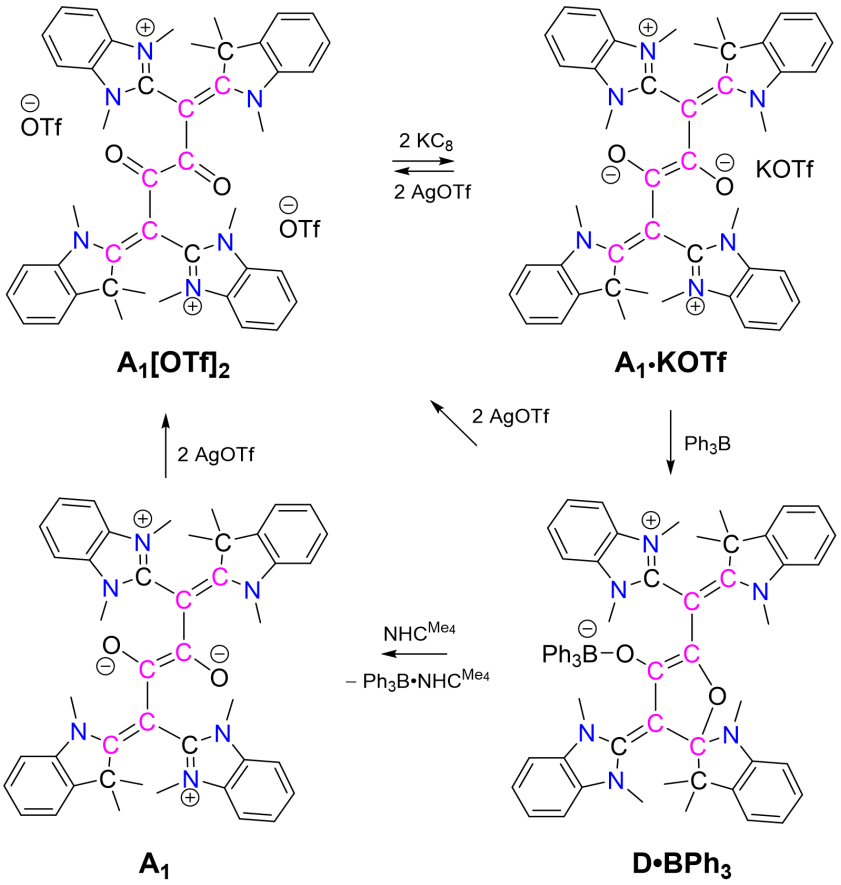

Figure 6.1: Reactivity of compound A.

This project was a cooperation with the group of Prof. Anukul Jana from Hyderabad (India) who performed all experimental investigations as well as measurements and provided us with their data. Compound $A_1[OTf]_2$ was synthesized from oxalyl chloride and an NHC/CAAC–carbodicarbene (N–heterocyclic carbene/ cyclic(alkyl)(amino)carbene). After reduction with potassium graphite the neutral A_1·KOTf was obtained. However, the molecule forms a complex with the ion pair KOTf which can not be separated by purification. In the reduced state, A_1 was observed to be EPR (Electron Paramagnetic Resonance) active and is therefore assumed to have biradicaloid character. Variable temperature EPR measurements yielded a singlet–triplet gap of only 0.93 kJ mol^{-1} (= 0.22 kcal mol^{-1}) by fitting the data to the

Bleaney–Bowers equation. When the complex A_1·KOTf is reacted with a Lewis acid such as BPh_3, compound D·BPh_3 is obtained. Importantly, D·BPh_3 exhibits a new C–O bond which connects one of the O atoms to a neighboring CAAC residue (see Figure 6.1). D·BPh_3 can be separated from the KOTf salt and the Lewis acid can be removed by addition of a strong Lewis base, i.e. carbene NHC^{Me_4} (1,3,4,5–tetra–methyl–imidazol–2–ylidene). The C–O bond formation was assumed to be reversible, although the nature of free compound A_1 is unknown. X–ray diffraction data could only be obtained for compound $A_1[KOTf]_2$ and compound D·BPh_3. D·BPh_3 can be oxidized by silver triflate (AgOTf) to reverse the C–O bond formation and yield compound $A_1[KOTf]_2$. Elucidating the unknown structure of $A_1$was the first goal of our theoretical study. As cyclic voltammetry experiments indicated that reduction and oxidation (RedOx) processes in this system are fully reversible, we attempted to model the RedOx chemistry by DFT calculations. Simultaneously, ST gaps were computed in an attempt to rationalize the experimentally found degeneracy of the lowest singlet and triplet states.

6.2 Computational Details

For our theoretical investigations the ORCA 5.0.4[71, 72] program package was employed. Optimizations were performed at the (u)ωB97X-D3/def2-SVP[77, 95] level of theory. Single point calculations were performed at the (u)ωB97X-D3/def2-TZVP[77, 95] level of theory.
The Conductor–like Polarizable Continuum Model (CPCM)[75] was used with THF ($\varepsilon = 7.43$) as solvent. All geometries were confirmed to be minima on the potential energy surface by vibrational frequency analysis, unless otherwise indicated.

6.3 Results and Discussion

6.3.1 Modeling of Reduction and Oxidation Processes

Figure 6.2 shows the potential energy surfaces of the di–cationic compound A_1^{2+} and its singly and doubly reduced derivatives. After one and two electron reduction, the compound relaxes to the A_1^{1+} and A_1^{0} geometries, respectively. A_1^{1+} retains the open A–type form because the formation of a O–NHC bond (B–type) is unfavorable (B_1^{1+} = +9 kcal mol^{-1}). On the contrary, the neutral A_1^{0} has a small barrier for the O–NHC bond formation ($TS1^0$ = 4 kcal mol^{-1}) and the product B_1^{0} is –13 kcal mol^{-1} lower in energy. When B_1^{0} is oxidized one time, the excess energy is sufficient to overcome the small barrier for the O–NHC bond breaking ($TS1^{1+}$)

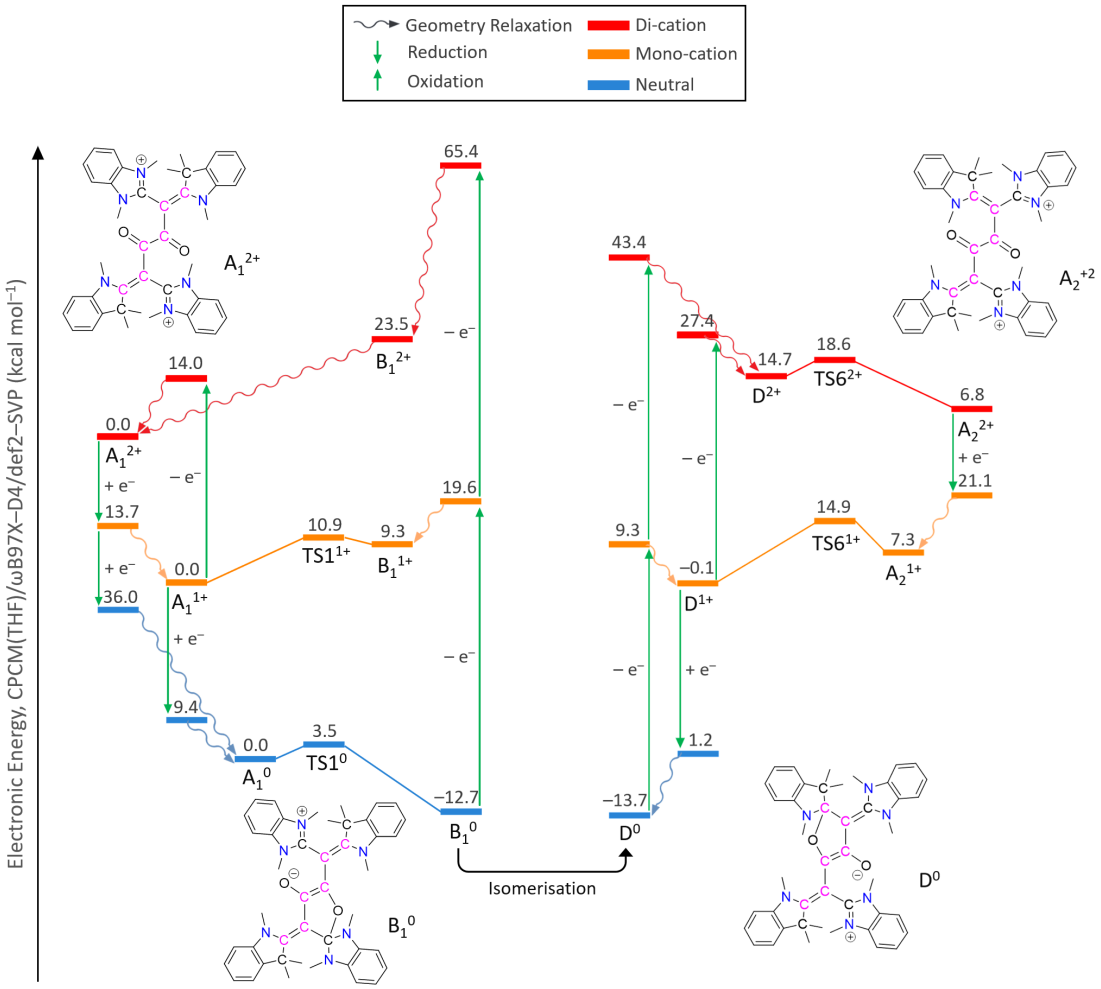

Figure 6.2: Potential energy surfaces of the di–cation (red), mono–cation (orange) and neutral system (blue). Electronic energies are referenced to the respective open form A_1^{2+}, A_1^{1+} and A_1^{0}. Instantaneous electron transfer is depicted by green arrows. Barrierless geometry relaxations are depicted by wave arrows. A–type systems show no O–carbene bond. B–type systems have only an O–NHC bond. C–type systems have both an O–NHC as well as an O–CAAC bond. D–type systems have only an O–CAAC bond.

and the system returns to an open A–type geometry. In any case, oxidation to the di–cation results in barrierless breaking of the O–NHC bond. The structure B_1^{2+} resembles the NHC spiro form (B–type), but it is not a PES minimum.

For the neutral B–type system there are several near degenerate conformations, that are accessible by rotations of the carbene residues ($TS2^0$, $TS3^0$, see Figure 6.3). Compound C^0 exhibits both an O–NHC bond as well as an O–CAAC bond. The later is responsible for a chiral center at the tetrahedral C atom. Hence, depending on the conformation before the O–CAAC bond formation, $TS4^0$ and $TS4^{*0}$ yield

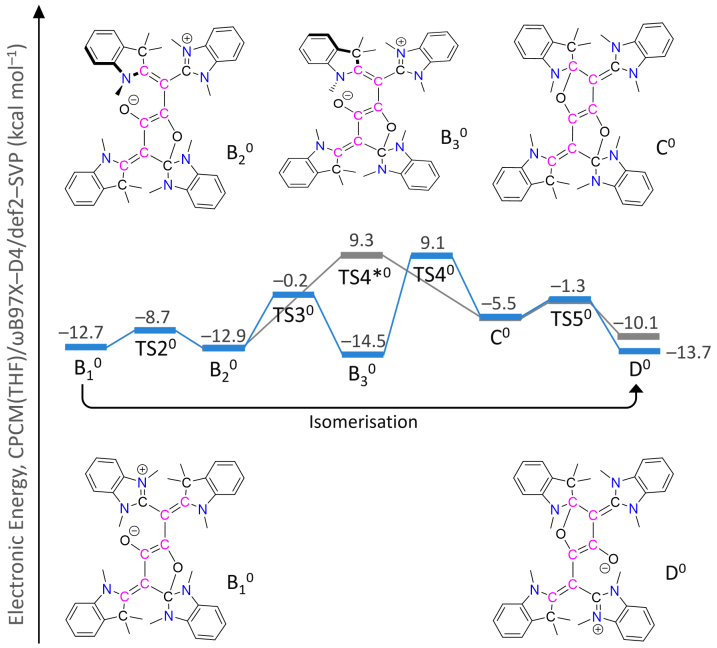

Figure 6.3: Isomerisation reaction from $B_1{}^0$ to D^0. B–type systems have only an O–NHC bond. C–type systems have both an O–NHC as well as an O–CAAC bond. D–type systems have only an O–CAAC bond. $TS4^{*0}$ denotes the transition state that leads to the enantiomer of C^0 and D^0 (grey line).

two distinct enantiomers of type C^0. The relative barriers for the formation of the C–type compound are about 24 and 22 kcal mol^{-1}, respectively. Because these are the highest barriers in the isomerization process, we expect the isomerization to occur slowly at room temperature. This explains why in the subsequent Lewis adduct experiments, the O–CAAC bond is found. It can already be present before the addition of the Lewis acid. As C^0 is an unfavorable intermediate in comparison to the B– and D–type systems, the O–NHC bond can be broken and a new isomer D^0 is formed. The two possible enantiomers for D^0 are about 4 kcal mol^{-1} apart. D^0 shows one O–CAAC bond and no O–NHC bond (D–type).

When D^0 is oxidized one time, D^{1+} retains the spiro form, as formation of the open A–type form is less stable by +7 kcal mol^{-1} for the mono–cation. After two electron oxidation, D^{2+} relaxes to a D–type spiro compound, but the excess energy is sufficient to break the O–CAAC bond and return to the open A–type system with a different conformation (compare $A_1{}^{2+}$ and $A_2{}^{2+}$).
If we assume an instantaneous electron transfer, both the reduction and the oxidation of compound $A_1{}^{2+}$ and its derivatives appear to be fully reversible regardless of the isomer. The excess energy is in any case sufficient to overcome whatever small

barriers are found for the isomerization from the open to the spiro form and vice versa.

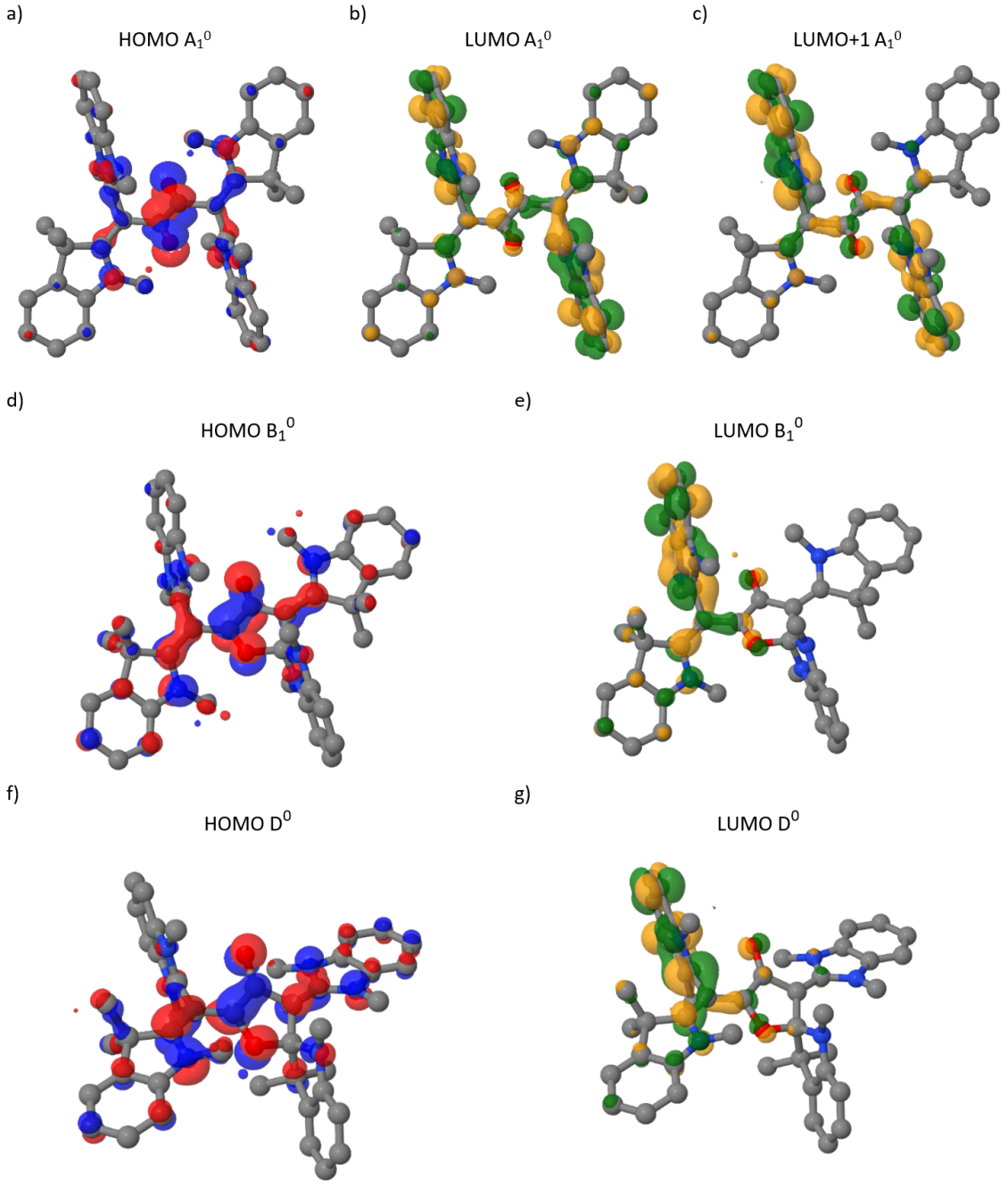

Figure 6.4: Restricted Kohn–Sham frontier molecular orbitals of isomers A_1^0, B_1^0, D^0 at the respective S_0 equilibrium geometry. Doubly occupied molecular orbitals are depicted in blue and red. Unoccupied orbitals are depicted in green and orange. Orbitals b) and c) are near degenerate. Isovalue = 0.03.

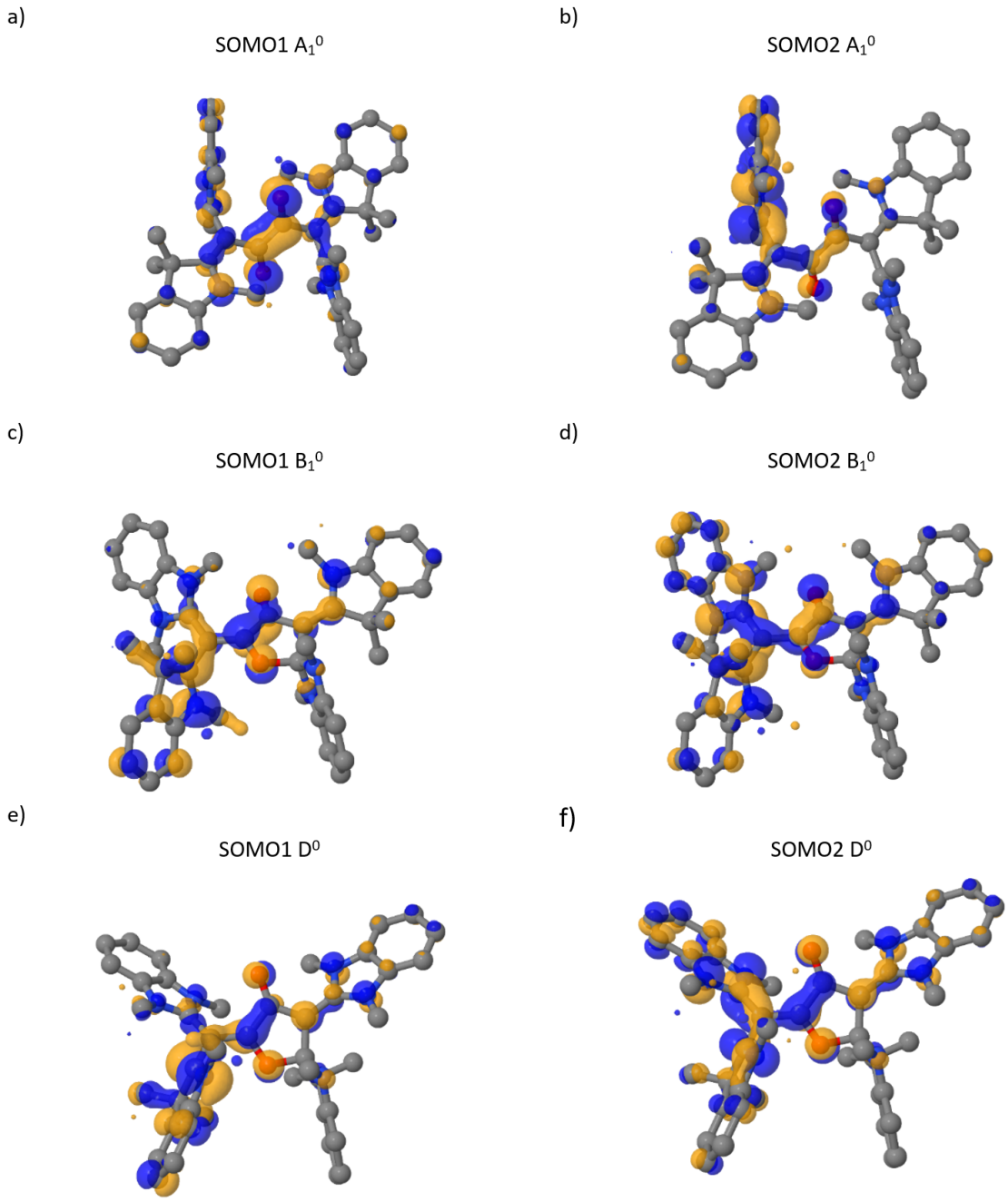

Figure 6.5: Unrestricted Kohn–Sham occupied alpha orbitals of isomers $A_1{}^0$, $B_1{}^0$, D^0 at the respective T_1 equilibrium geometry. The orbitals correspond to the frontier orbitals of the closed shell calculations in Figure 6.4. Singly occupied molecular orbitals are depicted in blue and orange. Isovalue = 0.03.

6.3.2 Prediction of Singlet–Triplet Gaps

Figure 6.4 depicts the frontier molecular orbitals of the isomers $A_1{}^0$, $B_1{}^0$, D^0 in their respective S_0 equilibrium geometries obtained by restricted Kohn–Sham calculations. Generally, the NHC residue on which the LUMO (lowest unoccupied molecular or-

bital) is localized is nearly orthogonal to the hexatriene motif. Figure 6.5 depicts the corresponding singly occupied frontier molecular orbitals resulting from unrestricted Kohn–Sham calculations on the respective T_1 equilibrium geometries. The optimized T_1 geometries differ from the corresponding S_0 equilibrium geometries. In the triplet geometry of the A–type isomer (Figure 6.5 a, b), the NHC residue where the SOMO2 (singly occupied molecular orbital) is mainly localized is bent towards the neighboring CO group. It maintains the 90° dihedral with respect to the hexatriene motif. For isomers $B_1{}^0$ and D^0, the NHC residue which is not part of the spiro center is rotated to a more in–plane conformation with respect to the hexatriene motif. This allows for more delocalization of SOMO2 towards the neighboring CAAC residue and the central OCCO motif (Figure 6.5 d, f). Also SOMO1 extents to the CAAC residue by a considerable amount when compared to the $A_1{}^0$ isomer (Figure 6.5 c, e).

Table 6.1 presents a benchmark calculation of the free energy of the A^0 to D^0 isomerization. The root mean square error of the def2-TZVP basis is only 0.4 kcal mol^{-1} in comparison to the augmented ma-def2-TZVP basis set. We conclude that a TZ valence basis set is large enough for single point DFT calculations and does not need augmentation.

Table 6.1: Benchmark of different basis sets with the CPCM(THF)/ωB97X-D4 method. All values are free energy values and include free energy corrections at the CPCM(THF)/ωB97X-D4/def2-SVP level. The values are given in kcal mol^{-1}. When referenced to ma-def2-TZVP values, the RMSD for def2-SVP, def2-TZVP and ma-def2-SVP is 4.7, 0.4 and 1.7 kcal mol^{-1}, respectively.

Basis set	$A_1{}^0$	$TS1^0$	$B_1{}^0$	$TS2^0$	$B_2{}^0$	$TS3^0$	$B_3{}^0$	$TS4^0$	C^0	$TS5^0$	D^0
def2-SVP	0.0	2.6	–14.0	–8.4	–12.2	0.1	–14.3	8.4	–6.2	–2.8	–14.3
def2-TZVP	0.0	1.3	–11.2	–5.2	–8.6	5.5	–10.4	13.6	1.7	3.5	–11.1
ma-def2-SVP	0.0	1.2	–12.5	–6.1	–9.6	3.3	–11.7	12.7	–0.1	1.5	–12.3
ma-def2-TZVP	0.0	1.5	–10.8	–5.1	–8.4	5.9	–10.2	14.2	2.4	3.7	–10.9

Because the cyclic voltammetry experiments were performed with the complex that includes KOTf, we investigated the influence of K+ cations on the $A_1{}^0$ to $B_1{}^0$ isomerization (see Figure 6.6).

Table 6.2 summarizes the adiabatic ST gaps of the isomerization intermediates from Figure 6.3 and the K^+ complexes from Figure 6.6. When the neutral system and the mono–cationic K^+ complex is considered, the formation of the spiro compound B_1 stabilizes the singlet ground state by –11.2 and –5.6 kcal mol^{-1}, respectively. Interestingly, the triplet state is almost unaffected by the cyclisation

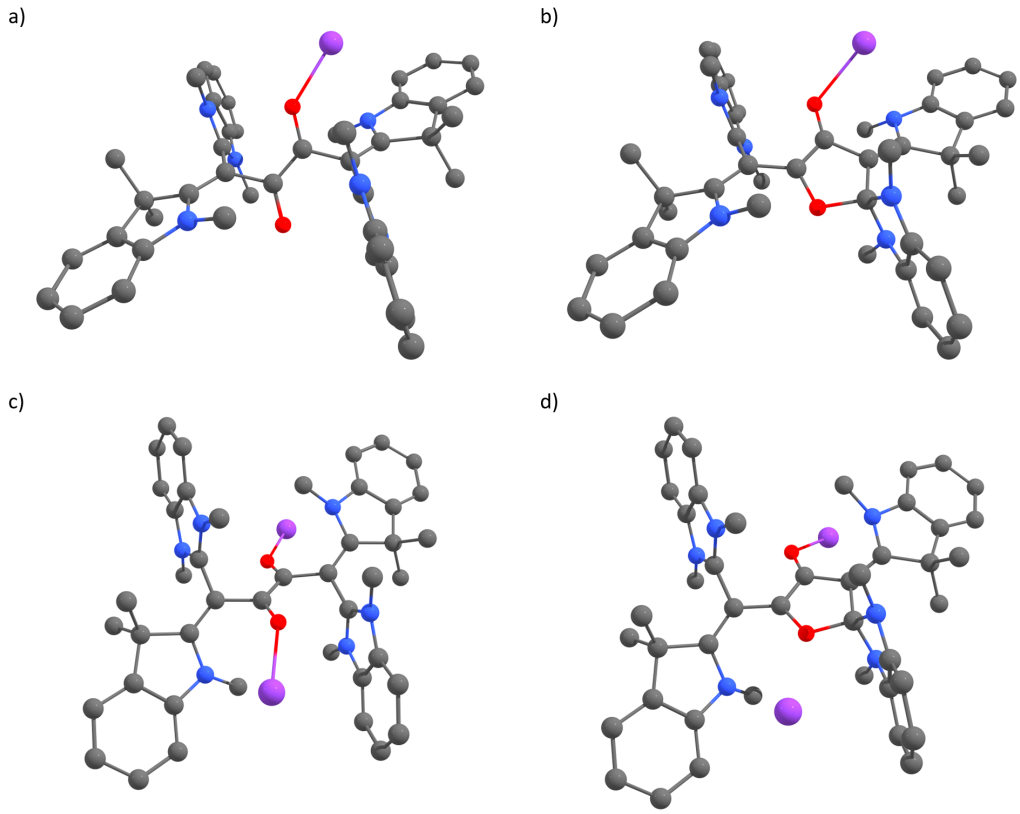

Figure 6.6: Placement of K^+ ions in the singlet ground state of the reduced compound. a) Open form with one K^+ ion, $[K_1A_1]^{1+}$. b) Spiro form with O–NHC bond and one K^+ ion, $[K_1B_1]^{1+}$. c) Open form with two K^+ ions, $[K_2A_1]^{2+}$. d) Spiro form with O–NHC bond and two K^+ ions, $[K_2B_1]^{2+}$. Hydrogens omitted for clarity.

reaction, leading to a larger ST gap than in the open form. While B and D type isomers are almost degenerate in their ground state free energy, the ST gap varies from 7.9 to 18.5 kcal mol^{-1} for the neutral system. The smallest ST gap for the spiro compounds is found with compound D, the CAAC spiro compound. For D, the triplet state is stabilized in comparison to the triplet state of A by –5 kcal mol^{-1}. The singlet is even more stabilized, which leads to an increased ST gap of 7.9 kcal mol^{-1} when compared to A (2.4 kcal mol^{-1}). Adding counterions to the neutral system destabilizes the spiro compound B with respect to A both for one and for two K+ ions. For $[K_1B_1]^{1+}$, the B isomer is still more stable than the open A form, but the energy gain from the cyclisation is only half of the gain in the corresponding neutral system. If two K^+ are added, the A and the B isomer become degenerate in the ground state, but the triplet state is destabilized considerably in comparison to the neutral system. This leads to relatively large ST gaps of about 10 kcal $mol^{-1}$for both the A and B isomer. The counterion dependent reaction energies of the A→B cyclisation in the S_0 state can be explained by the nature of the frontier molecular

Table 6.2: Adiabatic singlet–triplet gaps of different isomers at the CPCM(THF)/ωB97X-D4/def2-TZVP level of theory with additional free energy corrections at the CPCM(THF)/ωB97X-D4/def2-SVP level of theory. Values given in kcal mol^{-1}.

System	$A_1{}^0$	$B_1{}^0$	$B_2{}^0$	$B_3{}^0$	C^0	D^0	$[K_1A_1]^{1+}$	$[K_1B_1]^{1+}$	$[K_2A_1]^{2+}$	$[K_2B_1]^{2+}$
S0	0.0	–11.2	–8.6	–10.4	1.7	–11.1	0.0	–5.6	0.0	0.2
T1	2.4	1.8	6.9	8.1	25.1	–3.2	3.9	3.7	11.3	9.0
S-T gap	2.4	13.0	15.5	18.5	23.4	7.9	3.9	9.3	11.3	8.8

orbitals of the A isomer (compare Figure 6.4). For the A–type isomer, the HOMO is mainly localized on the O atoms in the center of the molecule (Figure 6.4a). The formally negatively charged O atom in A is stabilized if the charge separation from the formally positively charged NHC residues is diminished by formation of a C–O bond in B. When K^+ are introduced, the negative charge around the O atoms is stabilized and the energy gain of the C–O bond formation is reduced or even cancelled out completely (in the case of two K^+ ions). The frontier SOMOs in the triplet state are already delocalized away from the central O atoms. This corresponds to a formal charge transfer from the center of the molecule to the carbene residues in comparison to the singlet ground state. Consequently, the C–O bond formation has only a small influence on the T_1 energy.

As a test, we also calculated the association energies of a [KOTf] ion pair to the neutral compounds $A_1{}^0$ and $B_1{}^0$ (Table 6.3). We argue that the ion pair is a more reasonable choice for the association energy than the free K^+ ion, because the cation is already stabilized in a similar way as in the target complex. The free K^+ is in comparison poorly stabilized by the CPCM which results in a non–physical bias towards the target complex. This effect is partly compensated in the ion pair. The optimized geometries were checked for imaginary frequencies and some showed low–frequency imaginary modes in the range of 0 – 70 cm^{-1}. As the calculations were only preliminary, we refrained from optimizing the geometries further and used the near converged geometries for single point calculations. Hence, the data does not include thermochemistry contributions and is limited to the comparison of electronic energies. Association of one or two equivalents of KOTf is considerably exothermic, but the triplet state is again less stabilized than the singlet ground state. This leads to larger ST gaps. We also observe that $A_1{}^0$ and $B_1{}^0$ become closer in energy when the ion pairs are added. This is in line with the previous cation calculations (Table 6.2).

Table 6.3: Singlet–triplet gaps of different isomers and ion pair complexes at the CPCM(THF)/ωB97X-D4/def2-TZVP level of theory. All values are electronic energies and are given in kcal mol^{-1}.

System	$A_1{}^0$	$B_1{}^0$	$A_1{}^0$·KOTf	$B_1{}^0$·KOTf	$A_1{}^0$·$[KOTf]_2$	$B_1{}^0$·$[KOTf]_2$
S0	0.0	–9.9	–22.2	–28.4	–50.2	–51.3
T1	5.2	4.8	–9.7	–9.5	–31.2	–31.7
S–T gap	5.2	14.7	12.6	18.9	19.0	19.6

To check the validity of the ring formation prediction, the following calculation was performed: Figure 6.7 shows a hypothetical O–NHC bond formation in compound X. Our prediction aligns with the literature[125], indicating the absence of an O–NHC bond due to the significant ring tension in the four membered ring (+9 kcal mol^{-1}). On the contrary, $B_1{}^0$ does not have substantial ring tension and consequently, the spiro form is stabilized with respect to the zwitterionic open form $A_1{}^0$.

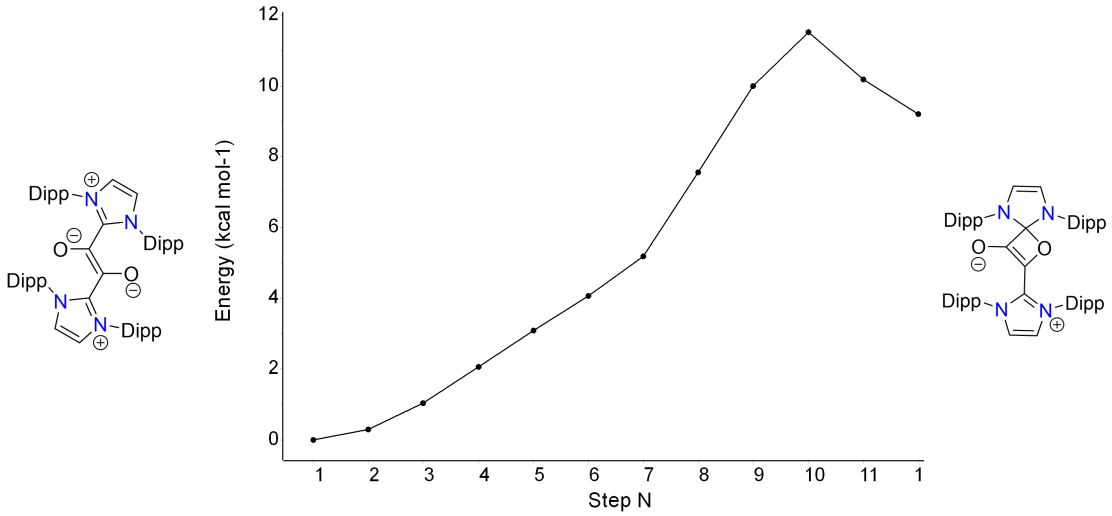

Figure 6.7: Nudge elastic band optimization of the minimal energy path between open form and spiro form of compound X. CPCM(THF)/ωB97X-D4/def2-SVP level of theory.

6.4 Conclusions

In summary, the PES of the system in its di–cationic, mono–cationic and neutral forms have been investigated. As a result, a variety of neutral isomers was discovered, which are kinetically and thermodynamically feasible. Importantly, the A–type isomer was found to be labile with respect to a C–O bond formation, which yields B–type isomers. The small ST gap of A_1 is in good agreement with the measured ST gap. But, as we predict that the B isomer is formed immediately after reduction, we can not rationalize the assumed biradicaloid character of the system by isomer A_1. All other isomers exhibit significantly larger ST gaps.

While we can not reproduce the small ST gap that is found in the experiment, the system exhibits extraordinary complexity due to the flexibility of its residues. Isomerization reactions and changes in conformation have a large impact on the calculated ST gap (Table 6.2). Addition of K^+ ions changes the PES of the system considerably which makes accurate predictions more difficult.
Therefore, the discrepancy in comparison to experimental data stems either from an insufficient theoretical model or the experimental data is faulty. Because the EPR method is very sensitive, trace impurities could cause an EPR signal. It is worth noting that the experimental ST gap was obtained from A_1·KOTf, as the measurement of pure A_1 failed due to the decomposition of the sample.

7 Summary

In the course of this work, a variety of systems and their potential energy surfaces both in the ground state and the electronically excited state were investigated. More specifically, the work focused mainly on a homogeneous catalysis process, which was mitigated by a main group element compound, as well as luminescence phenomena in organic crystals.

First, in a close collaboration with the Wagner group in Frankfurt, two distinct hydroboration mechanisms were discovered for a reduced 9,10–diboraanthracene (DBA) derivative in combination with pinacolborane as reagent. The behavior of DBA was found to depend on the substrate. For the bulky *N*–*t*Bu–benzylimine, the product of a B–H bond activation at the DBA moiety was observed. For all other unsaturated substrates, no activation of the borane reagent was found, but instead, the substrates underwent [4+2]–cycloaddition to the central DBA heterocycle, forming adducts that persisted throughout the hydroboration process. We focused our calculation on the first reaction as a special case, because the formation of a B–B bond sparked our interest. Although initial experimental indications were sparse, a plausible reaction mechanism was devised in a joint computational and experimental effort. A "hidden", undesired catalytic cycle based on BH_3, which is running independently of the DBA, was discovered, characterized by DFT and backed up by control experiments. During the investigation of the reaction, it became clear that an extensive environment model was crucial to the theoretical description of the reaction path. Equipped with this knowledge, the second reaction mechanism involving [4+2]–cycloaddition products as catalysts was proposed. Again, the importance of including the environment of the catalyst was confirmed, as the counterions of the catalyst were shown to stabilize the transition state of the rate determining step of the reaction.
The influence of the environment model on the reaction path prediction for the DBA–mediated hydroboration was shown to be significant. Therefore, the second project aimed at analyzing and understanding the effect of the first solvation shell on free energy calculations for homogeneous reactions. After checking the computational environment model against experimental data such as geometrical features in X–ray structures and coordination numbers, the dependency of the reaction path on the environment was confirmed by calculations of increasing complexity and system size. The most simple model involving anionic intermediates yielded significantly different results from the fully modeled environment and did not align with experi-

mental observations. The formation of the hydroboration product and regeneration of the doubly negatively charged catalyst was prohibited by an unphysical energetic trap at the singly charged intermediates. Inclusion of counterions somewhat mitigated this problem, but key intermediates were found to be considerably destabilized in comparison to the more extensive model which also included the first solvation shell. When both counterions and the first solvation shell are included, the correct product is predicted and key intermediates are stabilized. Additionally to the investigation of system size effects, a benchmark of electronic structure methods was performed. The ONIOM scheme proved especially useful to achieve basis set convergence in combination with correlated methods for the important negatively charged parts of the intermediates. The first solvation shell was described sufficiently by a cheaper DFT method.

The report of unusual room temperature phosphorescence (RTP) properties in simple arlyboronic esters by a Japanese group in the Journal of the American Chemical Society prompted an investigation of said compounds in the Marder group in Würzburg. After the author was involved in this project experimentally, some compounds indeed showed strange luminescence phenomena that warranted a computational investigation. The results of the computational efforts are presented within this work. Despite comprehensive simulations of the excited state potential energy surface, no satisfactory explanation was found for the apparent RTP. This gave rise to the suspicion that the long–lived luminescence effect was caused by trace impurities. Indeed, by continuous purification, an impurity could be isolated by our collaborators in the laboratory. Thorough investigation and comparison of both the host compound and the impurity as a guest were performed. They revealed that the delayed luminescence actually stemmed from a delayed fluorescence of the impurity and not the phosphorescence emission of the host. This was confirmed by doping experiments, i.e. controlled preparation of contaminated samples of the host. The delayed luminescence of the impurity could easily be mistaken for RTP of the host as the emission bands were found to be located in the same part of the spectrum. With this additional information, a exciton relaxation mechanism was suggested that aims at rationalizing the delayed fluorescence phenomenon. Essentially, we proposed that the impurity opens a new relaxation pathway for the excitons that form in the host after excitation. The relaxation proceeds through charge transfer states, whereby the electron rich impurity acts as a donor, while the electron deficient host acts as acceptor. Eventually, the exciton migrates to the impurity which emits a fluorescence signal. This relaxation process was assumed to give rise to the delay in the fluorescence of the impurity.

Lastly, in a collaboration with the Jana group from Hyderabad, India, the electro–chemical properties of a supposedly biradicaloid compound as well as its singlet–triplet (ST) gap were investigated. Our collaborators reported a fully reversible reduction and oxidation process as a result of cyclic voltammetry experiments. The reduction and oxidation are each divided in two single–electron transfers. Consequently, the potential energy surfaces of the di–cationic, mono–cationic and neutral forms were investigated, in an attempt at modeling the cyclic voltammetry experiments. The calculations revealed that reduction yields a spiro compound by the formation of a O–C bond to an adjacent carbene–like residue. According to the computations, this bond formation is fully reversible by oxidation of the compound. As the oxidation was shown to be a two step process, also the mono–cationic system was investigated, which lead to the same result. With respect to the electro–chemistry, all results align well with the experimental findings. The near–degeneracy of the singlet and the triplet state in the reduced compound, however, could not be confirmed computationally. While multiple isomers and conformers were found, each exhibiting a different (ST) gap, none matched with the experimental value, as the gap was always larger than 7 kcal mol^{-1}. Despite the mismatch, valuable insight on the structure of the compound was gained, considering that no structural data could be obtained experimentally.

In summary, this work presents the results of interdisciplinary collaborations between the author as computational chemist and colleagues who are involved in fundamental research on novel reactivity as well as investigations on photophysical effects. The herein presented results illustrate how important and fruitful the application of theory in an experimental context can be for a better (and accurate) understanding of chemical processes.

8 Zusammenfassung

Im Rahmen dieser Arbeit wurden eine Vielzahl von Systemen und ihre potentiellen Energieoberflächen sowohl im Grundzustand als auch im elektronisch angeregten Zustand untersucht. Konkret konzentrierten sich die Arbeiten vor allem auf einen homogenen Katalyseprozess, der durch eine Hauptgruppenelementverbindung abgeschwächt wurde, sowie auf Lumineszenzphänomene in organischen Kristallen.

Zunächst wurden in enger Zusammenarbeit mit der Wagner Gruppe in Frankfurt zwei unterschiedliche Hydroborierungsmechanismen für ein reduziertes 9,10–Diboraanthracen (DBA)–Derivat in Kombination mit Pinacolboran als Reagenz entdeckt. Es wurde festgestellt, dass das Verhalten von DBA vom Substrat abhängt. Für das sterisch anspruchsvolle *N*–*t*Bu–benzylimin wurde das Produkt einer B–H–Bindungsaktivierung an der DBA–Einheit beobachtet. Bei allen anderen ungesättigten Substraten wurde keine Aktivierung des Boran–Reagens festgestellt, stattdessen durchliefen die Substrate eine [4+2]–Cycloaddition an den zentralen DBA–Heterozyklus und bildeten Addukte, die während des gesamten Hydroborierungsprozesses bestehen blieben. Wir konzentrierten unsere Berechnungen auf die erste Reaktion als Sonderfall, da die Bildung einer B–B–Bindung unser Interesse weckte. Obwohl die ersten experimentellen Hinweise spärlich waren, wurde in einer gemeinsamen rechnerischen und experimentellen Anstrengung ein plausibler Reaktionsmechanismus entwickelt. Ein "versteckter", unerwünschter katalytischer Zyklus auf der Basis von BH_3, der unabhängig vom DBA abläuft, wurde entdeckt, durch DFT charakterisiert und durch Kontrollexperimente untermauert. Bei der Untersuchung der Reaktion wurde deutlich, dass ein umfangreiches Umgebungsmodell für die theoretische Beschreibung des Reaktionsverlaufs entscheidend ist. Mit diesem Wissen ausgestattet, wurde der zweite Reaktionsmechanismus vorgeschlagen, bei dem [4+2]–Cycloadditionsprodukte als Katalysatoren auftauchen. Auch hier bestätigte sich die Bedeutung der Einbeziehung der Umgebung des Katalysators, da sich zeigte, dass die Gegenionen des Katalysators den Übergangszustand des geschwindigkeitsbestimmenden Schritts der Reaktion stabilisieren.

Der Einfluss des Umgebungsmodells auf die Vorhersage der Reaktionspfade für die DBA–vermittelte Hydroborierung erwies sich als signifikant. Daher zielte das zweite Projekt darauf ab, die Auswirkungen der ersten Solvatationsschale auf die Berechnung der freien Energie für homogene Reaktionen zu analysieren und zu verstehen. Nach der Überprüfung des Modells der Umgebung anhand experimenteller Daten,

wie geometrischen Merkmalen in Röntgenstrukturen und Koordinationszahlen, wurde die Abhängigkeit des Reaktionspfads von der Umgebung durch Berechnungen mit zunehmender Komplexität und Systemgröße bestätigt. Das einfachste Modell, das anionische Zwischenprodukte einbezieht, ergab deutlich andere Ergebnisse als die vollständig modellierte Umgebung und stimmte nicht mit den experimentellen Beobachtungen überein. Die Bildung des Hydroborierungsprodukts und die Regeneration des doppelt negativ geladenen Katalysators wurden durch eine unphysikalische, energetische Falle an den einfach geladenen Zwischenprodukten verhindert. Die Einbeziehung von Gegenionen schwächte dieses Problem etwas ab, aber es zeigte sich, dass wichtige Zwischenstufen im Vergleich zu dem umfassenderen Modell, das auch die erste Solvatationsschale einschloss, erheblich destabilisiert waren. Wenn sowohl Gegenionen als auch die erste Solvatationsschale einbezogen werden, wird das korrekte Produkt vorhergesagt und die wichtigsten Zwischenprodukte werden stabilisiert. Zusätzlich zur Untersuchung von Effekten der Systemgröße wurde ein Benchmarking der elektronischen Strukturmethoden durchgeführt. Das ONIOM–Schema erwies sich als besonders nützlich, um Basissatzkonvergenz in Kombination mit korrelierten Methoden für die wichtigen, negativ geladenen Teile der Zwischenprodukte zu erreichen. Die erste Solvatationsschale wurde durch eine billigere DFT–Methode ausreichend beschrieben.

Der Bericht einer japanischen Gruppe im Journal of the American Chemical Society über ungewöhnliche Raumtemperatur–Phosphoreszenz (RTP) Eigenschaften in einfachen Arlyborsäureestern veranlasste die Marder Gruppe in Würzburg zu einer Untersuchung dieser Verbindungen. Nachdem der Autor an diesem Projekt experimentell beteiligt war, zeigten einige Verbindungen tatsächlich seltsame Lumineszenzphänomene, die eine theoretische Untersuchung rechtfertigten. Die Ergebnisse der theoretischen Untersuchungen werden in dieser Arbeit vorgestellt. Trotz umfassender Simulationen der Potentialhyperfläche des angeregten Zustands konnte keine zufriedenstellende Erklärung für die scheinbare RTP gefunden werden. Dies ließ den Verdacht aufkommen, dass der langlebige Lumineszenzeffekt durch Spurenverunreinigungen verursacht wurde. In der Tat konnte durch kontinuierliche Aufreinigung eine Verunreinigung durch unsere Mitarbeiter im Labor isoliert werden. Sowohl die Wirtsverbindung als auch die Verunreinigung als Gast wurden eingehend untersucht und verglichen. Die Untersuchungen ergaben, dass die verzögerte Lumineszenz tatsächlich auf eine verzögerte Fluoreszenz der Verunreinigung und nicht auf die Phosphoreszenzemission der Wirtsverbindung zurückzuführen ist. Dies wurde durch Dotierungsexperimente, d. h. die kontrollierte Herstellung von verunreinigten

Proben des Wirts, bestätigt. Die verzögerte Lumineszenz der Verunreinigung könnte leicht mit RTP des Wirts verwechselt werden, da die Emissionsbanden im selben Teil des Spektrums liegen. Mit diesen zusätzlichen Informationen wurde ein Exzitonen–Relaxationsmechanismus vorgeschlagen, der das Phänomen der verzögerten Fluoreszenz erklären soll. Im Wesentlichen schlugen wir vor, dass die Verunreinigung einen neuen Relaxationspfad für die Exzitonen eröffnet, die sich nach der Anregung im Wirt bilden. Die Relaxation verläuft über Ladungstransferzustände, wobei die elektronenreiche Verunreinigung als Donor und der elektronenarme Wirt als Akzeptor fungiert. Schließlich wandert das Exziton zu der Verunreinigung, die ein Fluoreszenzsignal aussendet. Es wurde angenommen, dass dieser Relaxationsprozess die Verzögerung der Fluoreszenz der Verunreinigung verursacht.

Schließlich wurden in Zusammenarbeit mit der Jana Gruppe aus Hyderabad, Indien, die elektrochemischen Eigenschaften einer vermeintlichen Biradicaloid–Verbindung sowie ihre Singulett–Triplett–Lücke (ST) untersucht. Unsere Mitarbeiter berichteten über einen vollständig reversiblen Reduktions– und Oxidationsprozess als Ergebnis von Cyclovoltammetrie–Experimenten. Die Reduktion und die Oxidation sind jeweils in zwei Einzelelektronentransfers aufgeteilt. Folglich wurden die Energiehyperflächen der di–kationischen, mono–kationischen und neutralen Formen untersucht, um zu versuchen, die Cyclovoltammetrie-Experimente zu modellieren. Die Berechnungen ergaben, dass die Reduktion zu einer Spiroverbindung führt, indem eine O–C–Bindung zu einem benachbarten carbenartigen Rest gebildet wird. Den Berechnungen zufolge ist diese Bindungsbildung durch Oxidation der Verbindung vollständig reversibel. Da sich die Oxidation als zweistufiger Prozess erwiesen hat, wurde auch das monokationische System untersucht, was zum gleichen Ergebnis führte. Was die Elektrochemie betrifft, so stimmen alle Ergebnisse gut mit den experimentellen Befunden überein. Die Beinahe–Entartung des Singulett– und des Triplett–Zustands in der reduzierten Verbindung konnte jedoch nicht theoretisch bestätigt werden. Es wurden zwar mehrere Isomere und Konformere gefunden, die jeweils eine andere ST–Lücke aufwiesen, aber keine stimmte mit dem experimentellen Wert überein, da die Lücke immer größer als 7 kcal mol^{-1}war. Trotz der Nichtübereinstimmung wurden wertvolle Einblicke in die Struktur der Verbindung gewonnen, da experimentell keine Strukturdaten bestimmt werden konnten.

Zusammenfassend stellt diese Arbeit die Ergebnisse der interdisziplinären Zusammenarbeit zwischen dem Autor als Computerchemiker und Kollegen vor, die an der Grundlagenforschung zu neuartiger Reaktivität sowie an Untersuchungen zu photo-

physikalischen Effekten beteiligt sind. Die hier vorgestellten Ergebnisse verdeutlichen, wie wichtig und fruchtbar die Anwendung der Theorie in einem experimentellen Kontext für ein besseres (und richtiges) Verständnis chemischer Prozesse sein kann.

9 Appendix

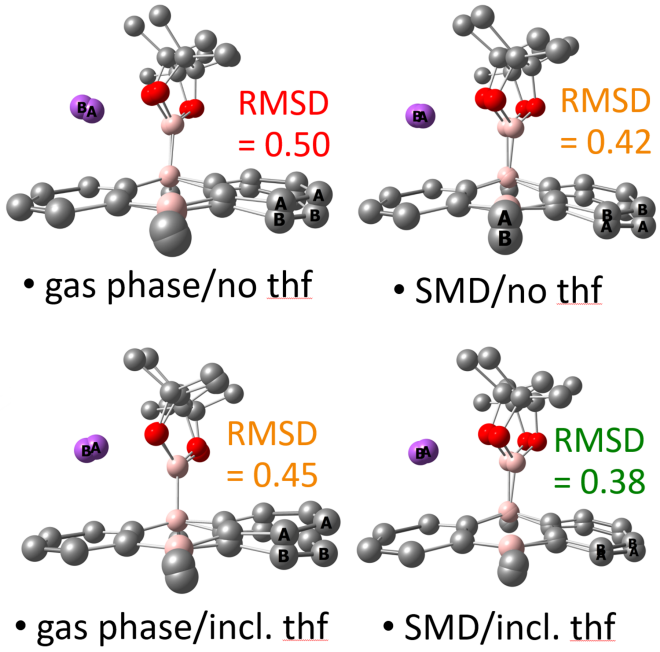

Figure 9.1: Influence of implicit and explicit solvation on the geometry. A: Optimized geometry. B: Crystal structure. Values are given in Å. Hydrogen atoms and explicit solvent removed for clarity.

Table 9.1: Comparison of different optimized coordination spheres and the crystal structure. * RMSD is referenced to the mean d(M-O_{THF}) of the crystal structure. All values are given in Å.

Li_2DBA	d(M-O_{THF})						mean d(M-O_{THF})	RMSD*	d(M-M)	absolute deviation d(M-M)
6 THF	2.077	2.127	2.127	2.077	2.099	2.099	2.101	0.123	4.413	0.591
4 THF	1.983	1.985	1.981	1.992			1.985	0.007	3.893	0.072
2 THF	1.899	1.899					1.899	0.080	3.511	-0.311
0 THF									3.468	-0.354
crystal	1.964	1.994	1.978	1.982			1.980	0.080	3.821	0.000
Na_2DBA	d(M-O_{THF})						mean d(M-O_{THF})	RMSD*	d(M-M)	absolute deviation d(M-M)
6 THF	2.336	2.346	2.329	2.328	2.342	2.338	2.336	0.093	4.811	0.274
4 THF	2.292	2.294	2.288	2.299			2.293	0.136	4.634	0.098
2 THF	2.256	2.256					2.256	0.173	4.548	0.012
0 THF									4.490	-0.046
crystal	2.367	2.506	2.404	2.429	2.372	2.499	2.429	0.068	4.536	0.000

Table 9.2: Comparison of the influence of system size on electronic energies and entropy corrections to Gibbs Free Energy. All values are given in kcal mol^{-1}.

Electronic Energies (ΔEE)

	full	no THF	anionic		full	no THF	anionic
A–1	25.0	25.2	24.4	B–1	28.1	39.3	70.2
A–2	0.0	0.0	0.0	B–2	3.0	14.0	45.8
A–3	11.1	31.5	0.3	B–3	0.0	0.0	0.0
A–4	-17.5	-1.4	-33.1	B–4	-14.9	-29.7	-16.6
A–5	-32.4	-31.1	-49.7	B–5	-13.4	3.2	17.9
A–6	-30.9	1.9	-15.2	B–6	-41.7	-41.7	-41.7
A–7	-56.2	-29.0	-29.0				

Entropy Correction (–TΔS)

	full	no THF	anionic		full	no THF	anionic
A–1	-17.1	-16.3	-15.1	B–1	-9.0	-11.8	-13.4
A–2	0.0	0.0	0.0	B–2	8.1	4.5	1.7
A–3	7.3	-5.3	-1.7	B–3	0.0	0.0	0.0
A–4	12.7	5.7	8.6	B–4	11.5	15.8	14.3
A–5	24.1	21.6	22.8	B–5	23.5	17.5	16.0
A–6	36.1	23.3	24.5	B–6	14.1	14.0	14.0
A–7	34.9	24.2	24.3				

Table 9.3: Comparison of Free Energies with different electronic structure methods for the electronic energy with the 6-311++G(d,p) basis set. Entropy corrections to Gibbs Free Energy are added from the ωB97XD/6-31+G(d,p) level of theory. All values are given in kcal mol^{-1}.

Basis Set	6-311++G(d,p)					
Solvation	IEFPCM, SMD variation					none
Method	ωB97XD	B3LYP-D3	M06-2X	PBE0-D3	SCS-MP2	ωB97XD
A–1	6.3	0.3	-2.9	1.7	-1.6	-2.6
A–2	0.0	0.0	0.0	0.0	0.0	0.0
A–3	19.0	16.5	18.5	18.0	21.6	18.6
A–4	-1.8	-3.2	-3.7	-3.4	3.5	4.4
A–5	-3.1	3.1	-4.4	-3.1	6.6	-1.9
A–6	12.1	19.1	11.0	11.7	20.9	8.6
A–7	-14.3	-6.6	-16.4	-16.2	-8.3	-16.2
RMSD	4.5	2.9	5.4	4.8	2.4	4.9
B–1	17.8	15.0	8.2	13.5	6.7	3.9
B–2	11.5	14.8	11.2	11.9	8.3	6.6
B–3	0.0	0.0	0.0	0.0	0.0	0.0
B–4	-1.3	6.2	-0.7	0.4	3.1	-6.3
B–5	13.9	22.3	14.7	15.2	17.4	4.2
B–6	-24.0	-18.2	-23.8	-24.6	-20.1	-27.2
RMSD	3.4	5.1	1.6	2.2	2.5	3.6

Table 9.4: Comparison of Free Energies with different basis sets for the electronic energy with the ωB97XD method. Entropy corrections to Gibbs Free Energy are added from the ωB97XD/6-31+G(d,p) level of theory. All values are given in kcal mol^{-1}.

Method	ωB97XD								
Solvation	IEFPCM, SMD variation								
Basis Set	6-311++**	cc-pVDZ	cc-pVTZ	aug-cc-pVDZ	def2-SVP	def2-TZV	def2-TZVP	def2-TZVPP	def2-QZVP
A–1	6.3	10.7	5.2	7.8	9.0	14.2	4.7	4.5	3.8
A–2	0.0	0.0	0.0	0.0	0.0	0.0	0.0	0.0	0.0
A–3	19.0	15.5	18.8	19.2	16.8	14.5	19.7	19.6	20.3
A–4	-1.8	-8.1	-4.1	-1.8	-8.2	-10.0	-2.2	-2.4	-1.5
A–5	-3.1	-8.3	-3.9	-4.8	-11.1	-13.5	-2.5	-2.7	-1.7
A–6	12.1	2.2	11.2	9.5	-1.0	-7.0	13.9	13.8	16.0
A–7	-14.3	-23.7	-16.2	-16.8	-28.0	-30.8	-13.7	-13.8	-11.9
RMSD	4.5	10.8	5.4	6.0	12.5	15.7	3.8	3.8	2.8
B–1	17.8	21.8	16.8	18.2	18.4	22.9	16.2	16.2	16.0
B–2	11.5	11.2	11.6	10.6	9.5	8.8	11.6	11.9	12.2
B–3	0.0	0.0	0.0	0.0	0.0	0.0	0.0	0.0	0.0
B–4	-1.3	-0.2	0.2	-3.1	-2.9	-3.5	-0.3	-0.2	-0.2
B–5	13.9	10.3	15.3	11.3	7.2	3.0	16.1	16.2	17.5
B–6	-24.0	-26.8	-23.7	-25.6	-29.3	-29.6	-23.2	-23.2	-22.6
RMSD	3.4	5.6	3.0	4.1	5.7	8.0	2.7	2.7	2.8

Table 9.5: Comparison of Free Energies with different basis sets for the electronic energy with the revDSD-PBEP86-D3BJ method. Entropy corrections to Gibbs Free Energy are added from the ωB97XD/6-31+G(d,p) level of theory. All values are given in kcal mol^{-1}.

Method	revDSD-PBEP86-D3BJ			
Solvation	CPCM, SMD variation			
Basis Set	cc-pVDZ	cc-pVTZ	aug-cc-pVDZ	aug-cc-pVTZ
A–1	5.4	-0.6	5.1	-7.9
A–2	0.0	0.0	0.0	0.0
A–3	15.4	18.5	19.8	12.3
A–4	-7.8	-3.4	-1.0	-8.3
A–5	-3.3	-0.2	-1.8	-6.2
A–6	7.8	15.2	10.1	11.4
A–7	-19.9	-13.3	-17.2	-11.0
RMSD	7.6	3.3	5.0	7.3
B–1	16.2	10.4	12.7	10.3
B–2	11.0	11.1	7.7	18.3
B–3	0.0	0.0	0.0	0.0
B–4	4.5	3.2	-0.9	2.1
B–5	15.6	18.6	11.1	19.8
B–6	-23.1	-21.1	-24.0	-20.9
RMSD	3.4	2.3	2.4	4.2

Table 9.6: Comparison of Free Energies with different solvation for the electronic energy with the ωB97X-D3 method. Entropy corrections to Gibbs Free Energy are added from the ωB97XD/6-31+G(d,p) level of theory. All values are given in kcal mol^{-1}.

Method	ωB97X-D3		
Solvation	CPCM, SMD variation	CPCM	none
Basis Set	ma-def2-TZVP		
A–1	6.3	4.8	-4.0
A–2	0.0	0.0	0.0
A–3	19.5	17.9	18.9
A–4	-2.1	-0.3	4.1
A–5	0.3	0.5	1.4
A–6	17.7	16.0	14.3
A–7	-11.7	-10.9	-13.1
RMSD	3.1	2.4	2.6
B–1	18.8	16.4	4.1
B–2	12.6	11.8	8.2
B–3	0.0	0.0	0.0
B–4	2.3	0.9	-2.7
B–5	19.8	16.3	10.2
B–6	-22.2	-22.3	-25.4
RMSD	4.3	2.8	2.8

Table 9.7: Comparison of Free Energies with different basis sets for the electronic energy with the DLPNO-CCSD(T) method. Entropy corrections to Gibbs Free Energy are added from the ωB97XD/6-31+G(d,p) level of theory. All values are given in kcal mol^{-1}.

Method	DLPNO-CCSD(T)		
Solvation	none		
Basis Set	cc-pVDZ	aug-cc-pVDZ	ma-def2-TZVP
A–1	5.3	5.8	0.3
A–2	0.0	0.0	0.0
A–3	17.3	21.0	22.1
A–4	-6.2	-0.1	1.4
A–5	0.1	-2.2	3.3
A–6	12.1	7.5	19.0
A–7	-17.1	-19.8	-11.1
RMSD	5.5	6.3	1.4
B–1	15.8	10.9	8.8
B–2	10.7	5.2	8.6
B–3	0.0	0.0	0.0
B–4	6.3	-2.1	1.9
B–5	18.2	7.6	17.6
B–6	-21.6	-24.9	-21.1
RMSD	3.9	3.9	1.7

Table 9.8: Comparison of Free Energies with different basis sets for the electronic energy with the ωB97XD:ωB97XD scheme. Entropy corrections to Gibbs Free Energy are added from the ωB97XD/6-31+G(d,p) level of theory. All values are given in kcal mol^{-1}.

ONIOM	ωB97XD:ωB97XD							
Solvation	IEFPCM, SMD variation							
High-layer	aug-cc-pVDZ		aug-cc-pVTZ			aug-cc-pVQZ		
Low-layer	cc-pVDZ	aug-cc-pVDZ	cc-pVDZ	cc-pVTZ	aug-cc-pVDZ	cc-pVDZ	cc-pVTZ	aug-cc-pVDZ
A–1	6.9	7.8	3.9	4.4	4.7	3.5	4.1	4.4
A–2	0.0	0.0	0.0	0.0	0.0	0.0	0.0	0.0
A–3	15.2	19.2	15.1	18.9	19.1	15.5	19.3	19.5
A–4	-5.6	-1.8	-5.2	-2.6	-1.4	-4.6	-2.1	-0.8
A–5	-5.3	-4.8	-2.3	-2.2	-1.9	-1.9	-1.8	-1.4
A–6	6.7	9.5	12.6	13.5	15.4	13.7	14.6	16.5
A–7	-19.1	-16.8	-14.3	-13.9	-12.1	-13.6	-13.2	-11.4
RMSD	7.7	6.0	5.0	3.9	3.1	4.5	3.4	2.6
B–1	18.9	18.2	17.7	16.1	17.0	17.3	15.7	16.6
B–2	12.1	10.6	14.0	11.8	12.4	13.9	11.7	12.3
B–3	0.0	0.0	0.0	0.0	0.0	0.0	0.0	0.0
B–4	0.3	-3.1	2.9	0.4	-0.5	2.7	0.3	-0.6
B–5	12.3	11.3	17.8	16.1	16.8	18.3	16.7	17.3
B–6	-25.6	-25.6	-23.1	-23.1	-23.1	-22.9	-22.9	-22.9
RMSD	4.2	4.1	4.0	2.7	3.1	3.9	2.6	3.0

Table 9.9: Comparison of Free Energies with different basis sets for the electronic energy with the DLPNO-CCSD(T):ωB97XD and the DLPNO-CCSD(T):DLPNO-CCSD(T) schemes. Entropy corrections to Gibbs Free Energy are added from the ωB97XD/6-31+G(d,p) level of theory. All values are given in kcal mol^{-1}.

ONIOM	DLPNO-CCSD(T):ωB97X-D3			DLPNO-CCSD(T):DLPNO-CCSD(T)			DLPNO-CCSD(T): ωB97X-D3
Solvation	none						CPCM
High-layer	ma-def2-SVP	ma-def2-TZVP	ma-def2-QZVP	def2-SVP	def2-TZVP	def2-QZVP	ma-def2-QZVP
Low-layer	ma-def2-TZVP			def2-TZVP			ma-def2-TZVP
A–1	0.5	-6.7	-8.1	-6.7	-11.5	-12.5	0.8
A–2	0.0	0.0	0.0	0	0	0.0	0.0
A–3	21.4	20.9	21.4	24.8	22.4	22.0	20.3
A–4	3.2	6.5	7.2	7	8.5	8.2	2.7
A–5	-2.8	3.2	3.2	1.1	4.7	3.5	1.9
A–6	3.7	15.0	16.7	13	17.8	17.9	17.8
A–7	-23.5	-12.5	-10.7	-17.1	-10.6	-10.3	-8.7
RMSD	8.1	1.1	0.0	3.2	1.6	1.8	0.0
B–1	3.3	-1.5	-2.1	-4.1	-6.9	-6.9	10.4
B–2	2.8	5.3	6.1	2.6	4.7	5.7	9.7
B–3	0.0	0.0	0.0	0	0	0.0	0.0
B–4	-6.0	-3.4	-4.0	-5.9	-3.8	-4.7	-0.9
B–5	0.5	8.5	9.5	6	9.3	9.7	15.1
B–6	-29.6	-24.4	-24.0	-26.7	-23.8	-24.2	-21.1
RMSD	5.1	0.6	0.0	2.6	2.0	2.0	0.0

Table 9.10: Comparison of wall times and geometrical RMSD for ONIOM scheme optimizations. "DFT" denotes the ωB97X-D3/def2-SVP level of theory.

	Walltime [h]							RMSD [Å]		
	DFT	DFT:B97-3c		B97-3c		total #atom	#QM atoms	B97-3c	anionic	neutral
A–1	10.66	5.17	49%	2.38	22%	84	32	0.754	1.350	1.475
A–2	20.62	12.01	58%	3.05	15%	106	54	0.121	0.377	0.467
A–3	3.96	4.59	116%	1.22	31%	63	24	0.529	0.825	0.815
A–4	1.77	3.25	184%	1.27	71%	45	6	0.485	0.956	0.968
A–5	5.05	4.06	80%	0.95	19%	59	33	0.435	0.518	0.563
A–6	7.14	6.50	91%	1.37	19%	77	51	0.084	0.931	0.908
B_2pin_3	2.94	2.94	100%	0.51	17%	62	62	0.211		
BH_3	0.14	0.33	232%	0.11	76%	17	4	0.039	0.918	0.918
HBpin	0.22	0.22	99%	0.11	49%	22	22	0.018		
Product	1.88	1.88	100%	0.47	25%	49	49	0.039		
Substrate	0.36	0.26	73%	0.15	42%	27	27	0.031		
THF	0.10	0.08	82%	0.08	82%	13	13	0.013		
Average			105%		39%	52	29	0.230	0.839	0.873

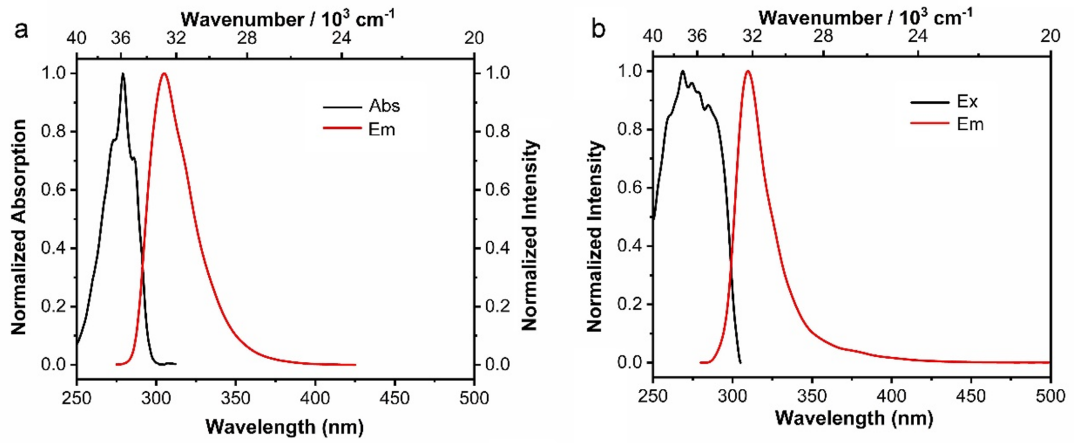

Figure 9.2: a) Normalized absorption and emission spectra of **1** in hexane; b) normalized excitation and emission spectra of **1** in the crystalline state (λ_{ex} = 265 nm).

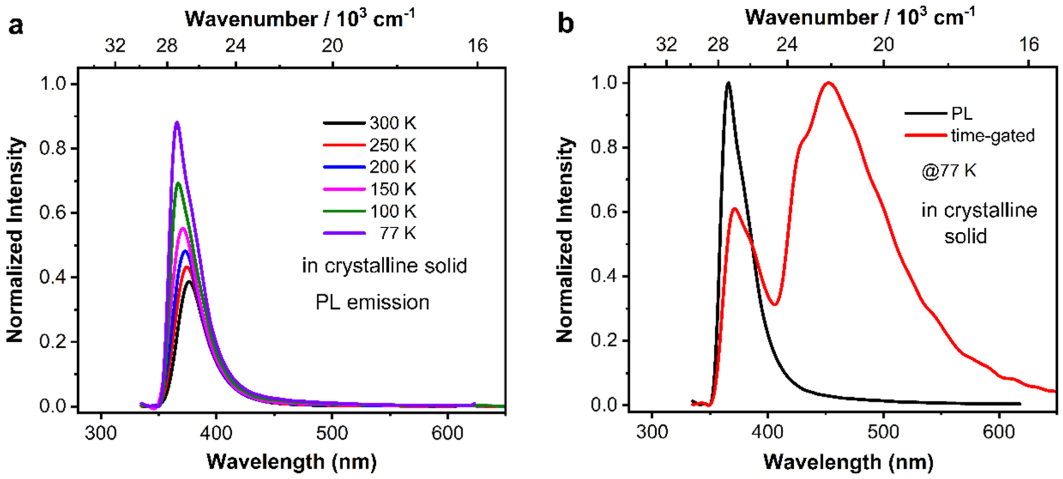

Figure 9.3: a) Photoluminescence spectra of **2** in the crystalline state at different temperatures (λ_{ex} = 300 nm); b) Normalized photoluminescence (black line) and time-gated (0.1 ms) emission (red line) spectra of **2** in the crystalline state at 77 K (λ_{ex} = 300 nm).

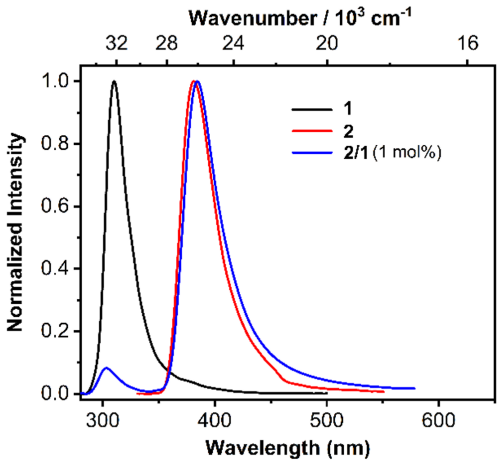

Figure 9.4: Normalized photoluminescence spectra of compounds **1**, **2** and **2/1** (1.0 mol%) in the crystalline state (λ_{ex} = 265 nm).

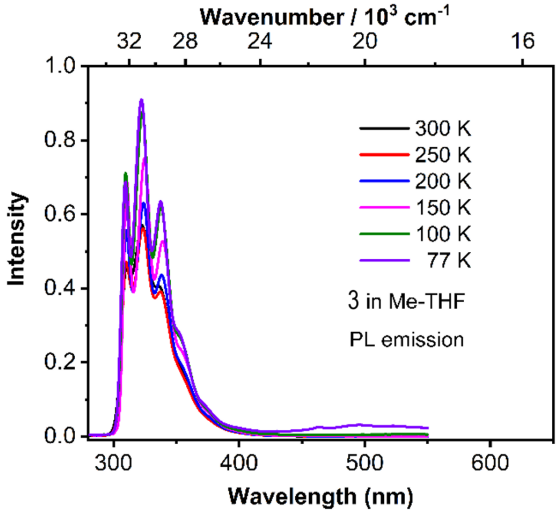

Figure 9.5: Photoluminescence spectra of **3** in 2–methyltetrahydrofuran at different temperatures (λ_{ex} = 265 nm).

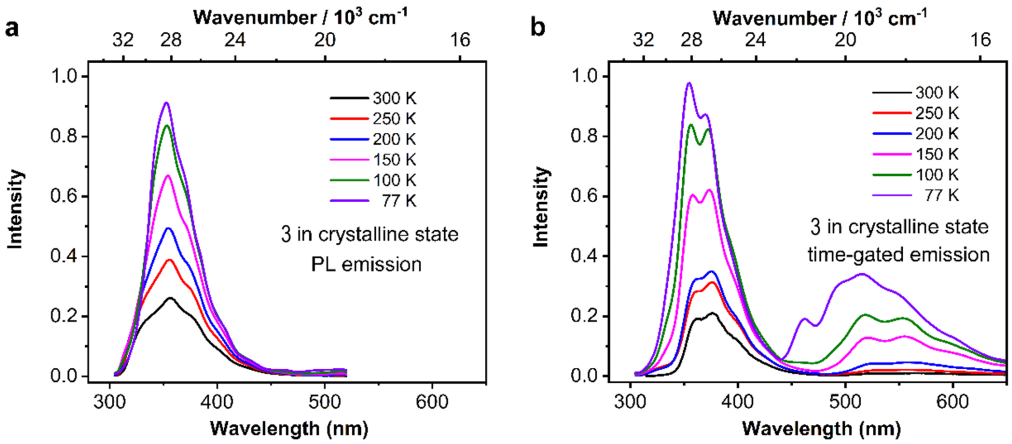

Figure 9.6: a) Photoluminescence spectra, b) Time-gated emission spectra of **3** in the crystalline state at different temperatures (λ_{ex} = 265 nm).

10 Acknowledgements

First of all, I would like to thank my supervisor Prof. Dr. Bernd Engels for the opportunity to embark on this journey in the realm of quantum chemistry. And what a journey it was! I was offered the chance to get in touch with the international scientific community at important conferences like the WATOC in 2022 and the ICQC in 2023. Our numerous discussions in pursuit of insight and understanding are greatly appreciated. My gratitude is also extended to my co–supervisor Prof. Dr. Volker Engel for his support. Many thanks deserves my mentor from overseas, Dr. Felipe Fantuzzi. Not only did he provide help and support in scientific questions, his unceasing enthusiasm for quantum chemistry and life in general was also a great source of inspiration.

Secondly, I would also like to thank all my collaborators in the wet lab. Prof. Dr. Matthias Wagner and Sven Prey from Frankfurt provided me with the opportunity to unravel elusive catalytic processes, an exemplary case of the importance of interdisciplinary work. In the same vein, I thank Prof. Dr. Todd Marder and Dr. Zhu Wu, for the chance to shed light on some strange luminescence phenomena. I thank Prof. Anukul Jana for our discussions in the last project of this thesis.

Of course, all past and present members of the angelic Engels and Engel groups whom I had the opportunity to meet are appreciated. Special mentions deserve, in no particular order: Dr. Dustin Kaiser, Dr. Sara Wirsing, Luca Craciunescu, Peter Schürger and Jessica Meyr. Special gratitude goes to Uschi Rüppel for her continuous support and the empathetic way she took care of us PhD students.

I would like to express my sincere gratitude for my office roommate Jessica. Through countless trials we prevailed as a team, be it as colleagues or just as friends. I wish I had your talent for keeping your life organized and well planned, at least in the short term. I am happy we adopted Peter into our team, he made an excellent addition to the Party Zone. There are few people I would have liked more as companions on this (at times literal) journey than you two. And Luca was also there.

Last, but not least, I am thankful for the good times that I spent together with all my other friends who shall not be named here individually, except for one. Emely, thank you for being the one and only #1. I also greatly appreciate the support by my (chosen) family.

11 References

[1] C. Herok, *Hydroboration Mechanisms of a Reduced 9,10–Diboraanthracene Catalyst*, Master's thesis, **2021**.

[2] M.-A. Légaré, C. Pranckevicius, H. Braunschweig, *Chemical reviews* **2019**, *119*, 8231–8261.

[3] S. E. Prey, M. Wagner, *Advanced Synthesis & Catalysis* **2021**, *363*, 1–21.

[4] A. Lorbach, M. Bolte, H.-W. Lerner, M. Wagner, *Organometallics* **2010**, *29*, 5762–5765.

[5] J. W. Taylor, A. McSkimming, C. F. Guzman, W. H. Harman, *Journal of the American Chemical Society* **2017**, *139*, 11032–11035.

[6] Y. Su, R. Kinjo, *Chemical Society Reviews* **2019**, *48*, 3613–3659.

[7] Di Wu, L. Kong, Y. Li, R. Ganguly, R. Kinjo, *Nature Communications* **2015**, *6*, 7340.

[8] Di Wu, R. Ganguly, Y. Li, S. N. Hoo, H. Hirao, R. Kinjo, *Chemical Science* **2015**, *6*, 7150–7155.

[9] B. Wang, Y. Li, R. Ganguly, H. Hirao, R. Kinjo, *Nature Communications* **2016**, *7*, 11871.

[10] Y. Su, Y. Li, R. Ganguly, R. Kinjo, *Angewandte Chemie International Edition* **2018**, *57*, 7846–7849.

[11] Y. Su, D. C. Huan Do, Y. Li, R. Kinjo, *Journal of the American Chemical Society* **2019**, *141*, 13729–13733.

[12] Di Wu, R. Wang, Y. Li, R. Ganguly, H. Hirao, R. Kinjo, *Chem* **2017**, *3*, 134–151.

[13] E. von Grotthuss, M. Diefenbach, M. Bolte, H.-W. Lerner, M. C. Holthausen, M. Wagner, *Angewandte Chemie (International ed. in English)* **2016**, *55*, 14067–14071.

[14] E. von Grotthuss, S. E. Prey, M. Bolte, H.-W. Lerner, M. Wagner, *Angewandte Chemie (International ed. in English)* **2018**, *57*, 16491–16495.

[15] E. von Grotthuss, S. E. Prey, M. Bolte, H.-W. Lerner, M. Wagner, *Journal of the American Chemical Society* **2019**, *141*, 6082–6091.

[16] S. Mukherjee, P. Thilagar, *Chemical Communications* **2015**, *51*, 10988–11003.

[17] G. Zhang, J. Chen, S. J. Payne, S. E. Kooi, J. N. Demas, C. L. Fraser, *Journal of the American Chemical Society* **2007**, *129*, 8942–8943.

[18] G. Zhang, S. E. Kooi, J. N. Demas, C. L. Fraser, *Advanced Materials* **2008**, *20*, 2099–2104.

[19] G. Zhang, G. M. Palmer, M. W. Dewhirst, C. L. Fraser, *Nature Materials* **2009**, *8*, 747–751.

[20] M. Koch, K. Perumal, O. Blacque, J. A. Garg, R. Saiganesh, S. Kabilan, K. K. Balasubramanian, K. Venkatesan, *Angewandte Chemie International Edition* **2014**, *53*, 6378–6382.

[21] M. B. Smith, J. Michl, *Chemical Reviews* **2010**, *110*, 6891–6936.

[22] J. C. Johnson, A. J. Nozik, J. Michl, *Accounts of Chemical Research* **2013**, *46*, 1290–1299.

[23] M. Li, X. Cai, Z. Qiao, K. Liu, W. Xie, L. Wang, N. Zheng, S.-J. Su, *Chemical Communications* **2019**, *55*, 7215–7218.

[24] Z. Chai, C. Wang, J. Wang, F. Liu, Y. Xie, Y.-Z. Zhang, J.-R. Li, Q. Li, Z. Li, *Chemical Science* **2017**, *8*, 8336–8344.

[25] M. A. El-Sayed, *Nature* **1963**, *197*, 481–482.

[26] Z. Wu, J. Nitsch, J. Schuster, A. Friedrich, K. Edkins, M. Loebnitz, F. Dinkelbach, V. Stepanenko, F. Würthner, C. M. Marian, L. Ji, T. B. Marder, *Angewandte Chemie International Edition* **2020**, *59*, 17137–17144.

[27] S. Kuno, T. Kanamori, Z. Yijing, H. Ohtani, H. Yuasa, *ChemPhotoChem* **2017**, *1*, 102–106.

[28] Y. Shoji, Y. Ikabata, Q. Wang, D. Nemoto, A. Sakamoto, N. Tanaka, J. Seino, H. Nakai, T. Fukushima, *Journal of the American Chemical Society* **2017**, *139*, 2728–2733.

[29] H. Yuasa, S. Kuno, *Bulletin of the Chemical Society of Japan* **2018**, *91*, 223–229.

[30] F. Jensen, *Introduction to computational chemistry*, 2nd ed., John Wiley & Sons, Chichester, England and Hoboken, NJ, **2007**.

[31] C. J. Cramer, *Essentials of Computational Chemistry: Theories and Models*, 2. ed., Wiley, s.l., **2013**.

[32] A. K. Wilson, J. Almlöf, *Theoretica chimica acta* **1997**, *95*, 49–62.

[33] M. Schütz, H.-J. Werner, *The Journal of Chemical Physics* **2001**, *114*, 661–681.

[34] C. Riplinger, F. Neese, *The Journal of Chemical Physics* **2013**, *138*, 034106.

[35] F. Neese, A. Hansen, D. G. Liakos, *The Journal of Chemical Physics* **2009**, *131*, 064103.

[36] S. F. Boys, *Reviews of Modern Physics* **1960**, *32*, 296–299.

[37] J. Pipek, P. G. Mezey, *The Journal of Chemical Physics* **1989**, *90*, 4916–4926.

[38] D. M. Schrader, S. Prager, *The Journal of Chemical Physics* **1962**, *37*, 1456–1460.

[39] E. J. Baerends, D. E. Ellis, P. Ros, *Chemical Physics* **1973**, *2*, 41–51.

[40] J. L. Whitten, *The Journal of Chemical Physics* **1973**, *58*, 4496–4501.

[41] B. I. Dunlap, J. W. D. Connolly, J. R. Sabin, *The Journal of Chemical Physics* **1979**, *71*, 4993–4999.

[42] B. I. Dunlap, *Physical Chemistry Chemical Physics* **2000**, *2*, 2113–2116.

[43] H.-J. Werner, F. R. Manby, P. J. Knowles, *The Journal of Chemical Physics* **2003**, *118*, 8149–8160.

[44] C. Møller, M. S. Plesset, *Physical Review* **1934**, *46*, 618–622.

[45] Y. Kurashige, J. Yang, G. K.-L. Chan, F. R. Manby, *The Journal of Chemical Physics* **2012**, *136*, 124106.

[46] R. Fink, V. Staemmler, *Theoretica chimica acta* **1993**, *87*, 129–145.

[47] J. Yang, G. K.-L. Chan, F. R. Manby, M. Schütz, H.-J. Werner, *The Journal of Chemical Physics* **2012**, *136*, 144105.

[48] W. Kohn, L. J. Sham, *Physical Review* **1965**, *140*, A1133–A1138.

[49] J. P. Perdew, A. Ruzsinszky, J. Tao, V. N. Staroverov, G. E. Scuseria, G. I. Csonka, *The Journal of Chemical Physics* **2005**, *123*, 62201.

[50] P. A. M. Dirac, *Mathematical Proceedings of the Cambridge Philosophical Society* **1930**, *26*, 376–385.

[51] T. Leininger, H. Stoll, H.-J. Werner, A. Savin, *Chemical Physics Letters* **1997**, *275*, 151–160.

[52] H. Iikura, T. Tsuneda, T. Yanai, K. Hirao, *The Journal of Chemical Physics* **2001**, *115*, 3540–3544.

[53] O. A. Vydrov, G. E. Scuseria, *The Journal of Chemical Physics* **2006**, *125*, 234109.

[54] T. Stein, L. Kronik, R. Baer, *Journal of the American Chemical Society* **2009**, *131*, 2818–2820.

[55] T. Stein, H. Eisenberg, L. Kronik, R. Baer, *Physical Review Letters* **2010**, *105*, 266802.

[56] L. Kronik, T. Stein, S. Refaely-Abramson, R. Baer, *Journal of Chemical Theory and Computation* **2012**, *8*, 1515–1531.

[57] J. P. Perdew, R. G. Parr, M. Levy, J. L. Balduz, *Physical Review Letters* **1982**, *49*, 1691–1694.

[58] C. Almbladh, U. von Barth, *Physical review. B Condensed matter* **1985**, *31*, 3231–3244.

[59] L. Craciunescu, S. Wirsing, S. Hammer, K. Broch, A. Dreuw, F. Fantuzzi, V. Sivanesan, P. Tegeder, B. Engels, *The journal of physical chemistry letters* **2022**, *13*, 3726–3731.

[60] L. Craciunescu, M. Asbach, S. Wirsing, S. Hammer, F. Unger, K. Broch, F. Schreiber, G. Witte, A. Dreuw, P. Tegeder, F. Fantuzzi, B. Engels, *Journal of Chemical Theory and Computation* **2023**, *19*, 9369–9387.

[61] L. W. Chung, W. M. C. Sameera, R. Ramozzi, A. J. Page, M. Hatanaka, G. P. Petrova, T. V. Harris, X. Li, Z. F. Ke, F. Y. Liu, H. B. Li, L. N. Ding, K. Morokuma, *Chemical Reviews* **2015**, *115*, Sp. Iss. SI Cl6fw Times Cited:591 Cited References Count:1172, 5678–5796.

[62] A. Warshel, M. Levitt, *Journal of Molecular Biology* **1976**, *103*, 227–249.

[63] D. Bakowies, W. Thiel, *The Journal of Physical Chemistry* **1996**, *100*, 10580–10594.

[64] M. Svensson, S. Humbel, R. D. J. Froese, T. Matsubara, S. Sieber, K. Morokuma, *The Journal of Physical Chemistry* **1996**, *100*, 19357–19363.

[65] Y. Zhang, T.-S. Lee, W. Yang, *The Journal of Chemical Physics* **1999**, *110*, 46–54.

[66] G. G. Ferenczy, J.-.-L. Rivail, P. R. Surján, G. Náray–Szabó, *Journal of Computational Chemistry* **1992**, *13*, 830–837.

[67] G. Henkelman, B. P. Uberuaga, H. Jónsson, *The Journal of Chemical Physics* **2000**, *113*, 9901–9904.

[68] S. Smidstrup, A. Pedersen, K. Stokbro, H. Jónsson, *The Journal of Chemical Physics* **2014**, *140*, 214106.

[69] S. E. Prey, C. Herok, F. Fantuzzi, M. Bolte, H.-W. Lerner, B. Engels, M. Wagner, *Chemical Science* **2023**, *14*, 849–860.

[70] M. J. Frisch, G. W. Trucks, H. B. Schlegel, G. E. Scuseria, M. A. Robb, J. R. Cheeseman, G. Scalmani, V. Barone, G. A. Petersson, H. Nakatsuji, X. Li, M. Caricato, A. V. Marenich, J. Bloino, B. G. Janesko, R. Gomperts, B. Mennucci, H. P. Hratchian, J. V. Ortiz, A. F. Izmaylov, J. L. Sonnenberg, D. Williams-Young, F. Ding, F. Lipparini, F. Egidi, J. Goings, B. Peng, A. Petrone, T. Henderson, D. Ranasinghe, V. G. Zakrzewski, J. Gao, N. Rega, G. Zheng, W. Liang, M. Hada, M. Ehara, K. Toyota, R. Fukuda, J. Hasegawa, M. Ishida, T. Nakajima, Y. Honda, O. Kitao, H. Nakai, T. Vreven, K. Throssell, Montgomery, Jr., J. A., J. E. Peralta, F. Ogliaro, M. J. Bearpark, J. J. Heyd, E. N. Brothers, K. N. Kudin, V. N. Staroverov, T. A. Keith, R. Kobayashi, J. Normand, K. Raghavachari, A. P. Rendell, J. C. Burant, S. S. Iyengar, J. Tomasi, M. Cossi, J. M. Millam, M. Klene, C. Adamo, R. Cammi, J. W. Ochterski, R. L. Martin, K. Morokuma, O. Farkas, J. B. Foresman, D. J. Fox, Gaussian˜16 Revision A.03, **2016**.

[71] F. Neese, *WIREs Computational Molecular Science* **2012**, *2*, 73–78.

[72] F. Neese, *WIREs Computational Molecular Science* **2022**, *12*, DOI 10.1002/wcms.1606.

[73] A. V. Marenich, C. J. Cramer, D. G. Truhlar, *The Journal of Physical Chemistry. B* **2009**, *113*, 6378–6396.

[74] S. Miertuš, E. Scrocco, J. Tomasi, *Chemical Physics* **1981**, *55*, 117–129.

[75] V. Barone, M. Cossi, *The Journal of Physical Chemistry A* **1998**, *102*, 1995–2001.

[76] J.-D. Chai, M. Head-Gordon, *Physical Chemistry Chemical Physics : PCCP* **2008**, *10*, 6615–6620.

[77] Y.-S. Lin, G.-D. Li, S.-P. Mao, J.-D. Chai, *Journal of Chemical Theory and Computation* **2013**, *9*, 263–272.

[78] A. Ben-Naim, *The Journal of Physical Chemistry* **1978**, *82*, 792–803.

[79] A. D. Becke, *The Journal of Chemical Physics* **1993**, *98*, 5648–5652.

[80] C. Lee, W. Yang, R. Parr, *Physical Review. B Condensed Matter* **1988**, *37*, 785–789.

[81] S. Grimme, J. Antony, S. Ehrlich, H. Krieg, *The Journal of Chemical Physics* **2010**, *132*, 154104.

[82] G. Santra, N. Sylvetsky, J. M. L. Martin, *The Journal of Physical Chemistry. A* **2019**, *123*, 5129–5143.

[83] Y. Zhao, D. G. Truhlar, *Theoretical Chemistry Accounts* **2008**, *120*, 215–241.

[84] Y. Guo, C. Riplinger, U. Becker, D. G. Liakos, Y. Minenkov, L. Cavallo, F. Neese, *The Journal of Chemical Physics* **2018**, *148*, 011101.

[85] C. Adamo, V. Barone, *The Journal of Chemical Physics* **1999**, *110*, 6158–6170.

[86] J. G. Brandenburg, C. Bannwarth, A. Hansen, S. Grimme, *The Journal of Chemical Physics* **2018**, *148*, 064104.

[87] M. J. Frisch, M. Head-Gordon, J. A. Pople, *Chemical Physics Letters* **1990**, *166*, 275–280.

[88] S. Grimme, *The Journal of Chemical Physics* **2003**, *118*, 9095–9102.

[89] R. Ditchfield, W. J. Hehre, J. A. Pople, *The Journal of Chemical Physics* **1971**, *54*, 724–728.

[90] A. D. McLean, G. S. Chandler, *The Journal of Chemical Physics* **1980**, *72*, 5639–5648.

[91] T. Clark, J. Chandrasekhar, G. W. Spitznagel, P. V. R. Schleyer, *Journal of Computational Chemistry* **1983**, *4*, 294–301.

[92] M. J. Frisch, J. A. Pople, J. S. Binkley, *The Journal of Chemical Physics* **1984**, *80*, 3265–3269.

[93] T. H. Dunning, *The Journal of Chemical Physics* **1989**, *90*, 1007–1023.

[94] B. P. Prascher, D. E. Woon, K. A. Peterson, T. H. Dunning, A. K. Wilson, *Theoretical Chemistry Accounts* **2011**, *128*, 69–82.

[95] F. Weigend, R. Ahlrichs, *Physical Chemistry Chemical Physics : PCCP* **2005**, *7*, 3297–3305.

[96] R. A. Kendall, T. H. Dunning, R. J. Harrison, *The Journal of Chemical Physics* **1992**, *96*, 6796–6806.

[97] J. Zheng, X. Xu, D. G. Truhlar, *Theoretical Chemistry Accounts* **2011**, *128*, 295–305.

[98] F. Weigend, *Physical Chemistry Chemical Physics : PCCP* **2006**, *8*, 1057–1065.

[99] F. Weigend, A. Köhn, C. Hättig, *The Journal of Chemical Physics* **2002**, *116*, 3175–3183.

[100] C. Hättig, *Physical Chemistry Chemical Physics* **2005**, *7*, 59–66.

[101] A. Hellweg, C. Hättig, S. Höfener, W. Klopper, *Theoretical Chemistry Accounts* **2007**, *117*, 587–597.

[102] G. L. Stoychev, A. A. Auer, F. Neese, *Journal of Chemical Theory and Computation* **2017**, *13*, 554–562.

[103] B. Helmich-Paris, B. de Souza, F. Neese, R. Izsák, *The Journal of Chemical Physics* **2021**, *155*, 104109.

[104] A. Tongraar, B. Michael Rode, *Chemical Physics Letters* **2004**, *385*, 378–383.

[105] J. Zhang, H. Zhang, T. Wu, Q. Wang, D. van der Spoel, *Journal of Chemical Theory and Computation* **2017**, *13*, 1034–1043.

[106] R. E. Skyner, J. L. McDonagh, C. R. Groom, T. van Mourik, J. B. O. Mitchell, *Physical Chemistry Chemical Physics* **2015**, *17*, 6174–6191.

[107] V. S. Bryantsev, M. S. Diallo, W. A. Goddard, *The Journal of Physical Chemistry. B* **2008**, *112*, 9709–9719.

[108] T. Vreven, K. Morokuma, O. Farkas, H. B. Schlegel, M. J. Frisch, *Journal of Computational Chemistry* **2003**, *24*, 760–769.

[109] J. C. Sancho-García, C. Adamo, *Physical Chemistry Chemical Physics* **2013**, *15*, 14581–14594.

[110] TURBOMOLE V7.6 2021, a development of University of Karlsruhe and Forschungszentrum Karlsruhe GmbH, 1989-2007, TURBOMOLE GmbH, since 2007; available from
`https://www.turbomole.org`.

[111] S. G. Balasubramani, G. P. Chen, S. Coriani, M. Diedenhofen, M. S. Frank, Y. J. Franzke, F. Furche, R. Grotjahn, M. E. Harding, C. Hättig, A. Hellweg, B. Helmich-Paris, C. Holzer, U. Huniar, M. Kaupp, A. Marefat Khah, S. Karbalaei Khani, T. Müller, F. Mack, B. D. Nguyen, S. M. Parker, E. Perlt, D. Rappoport, K. Reiter, S. Roy, M. Rückert, G. Schmitz, M. Sierka, E. Tapavicza, D. P. Tew, C. van Wüllen, V. K. Voora, F. Weigend, A. Wodynski, J. M. Yu, *The Journal of Chemical Physics* **2020**, *152*, 184107.

[112] M. Häser, R. Ahlrichs, *Journal of Computational Chemistry* **1989**, *10*, 104–111.

[113] C. Hättig, F. Weigend, *The Journal of Chemical Physics* **2000**, *113*, 5154–5161.

[114] C. Hättig, K. Hald, *Physical Chemistry Chemical Physics* **2002**, *4*, 2111–2118.

[115] C. Hättig, A. Köhn, *The Journal of Chemical Physics* **2002**, *117*, 6939–6951.

[116] C. Hättig, A. Hellweg, A. Köhn, *Physical Chemistry Chemical Physics* **2006**, *8*, 1159–1169.

[117] A. Hellweg, S. A. Grün, C. Hättig, *Physical Chemistry Chemical Physics* **2008**, *10*, 4119–4127.

[118] C. Brückner, B. Engels, *Chemical Physics* **2017**, *482*, 319–338.

[119] F. Plasser, *The Journal of Chemical Physics* **2020**, *152*, 084108.

[120] B. Engels, V. Engel, *Physical Chemistry Chemical Physics* **2017**, *19*, 12604–12619.

[121] R. Fukuda, M. Ehara, *Physical Chemistry Chemical Physics* **2013**, *15*, 17426–17434.

[122] M. Rubio, M. Merchán, E. Ortí, B. O. Roos, *Chemical Physics Letters* **1995**, *234*, 373–381.

[123] Y. Pan, W. Li, S. Zhang, L. Yao, C. Gu, H. Xu, B. Yang, Y. Ma, *Advanced Optical Materials* **2014**, *2*, 503.

[124] Y. Xu, P. Xu, D. Hu, Y. Ma, *Chemical Society Reviews* **2021**, *50*, 1030–1069.

[125] Y. Kim, J. E. Byeon, G. Y. Jeong, S. S. Kim, H. Song, E. Lee, *Journal of the American Chemical Society* **2021**, *143*, 8527–8532.

Julius-Maximilians-
UNIVERSITÄT
WÜRZBURG

Fakultät für
CHEMIE UND
PHARMAZIE

Erklärung zur Autorenschaft

Multifaceted behavior of a doubly reduced arylborane in B–H-bond activation and hydroboration catalysis, Sven E. Prey, Christoph Herok, Felipe Fantuzzi, Michael Bolte, Hans-Wolfram Lerner, Bernd Engels, Matthias Wagner, Chemical Science, 2023, 14, 849-860.

Detaillierte Darstellung der Anteile an der Veröffentlichung (in %)
Angabe Autoren/innen (ggf. Haupt- / Ko- / korrespondierende/r Autor/in) mit Vorname Nachname

Autor/in 1 (Sven E. Prey), Autor/in 2 (Christoph Herok), Autor/in 3 (Felipe Fantuzzi), Autor/in 4 (Michael Bolte), Autor/in 5 (Hans-Wolfram Lerner), Autor/in 6 (Bernd Engels), Autor/in 7 (Matthias Wagner)

Autor	A1	A2	A3	A4	A5	A6	A7					∑ in Prozent
Chemical synthesis and experiments	95	0	0	5	0	0	0					100%
Quantum chemical calculations	0	100	0	0	0	0	0					100%
Interpretation of experiments	80	0	0	0	0	0	20					100%
Interpretation of calculations	0	80	10	0	0	10	0					100%
Manuscript	35	40	0	0	5	10	10					100%
Corrections of manuscript	20	25	0	0	5	25	25					100%
												0%
												0%
												0%
												0%
												0%
												0%
												0%
Summe	38	41	2	1	2	8	8					100%

12 Author Contributions